
Turbulence Modelling for Smoothed Particle Hydrodynamics

Report submitted in complete fulfillment of the requirements of the degree of
Master of Technology

by

K T Prajwal Prathiksh

Roll No. : 180010027

Supervisor:

Prof. Prabhu Ramachandran



Department of Aerospace Engineering
Indian Institute of Technology Bombay

June 2022 - June 2023

Declaration of Authorship

I, K T Prajwal Prathiksh, hereby declare that this written submission on "*Turbulence Modelling for Smoothed Particle Hydrodynamics*", represents my ideas in my own words and where others' ideas or words have been included, I have adequately cited and referenced the original sources. I also declare that I have adhered to all principles of academic honesty and integrity and have not misrepresented or fabricated or falsified any idea/data/fact/source in my submission. I understand that any violation of the above will be cause for disciplinary action by the *Indian Institute of Technology Bombay*, and can also evoke penal action from the sources which have thus not been properly cited or from whom proper permission has not been taken when needed.

Date:
June 28, 2023

Student Name: K T Prajwal Prathiksh
Roll No.: 180010027

INDIAN INSTITUTE OF TECHNOLOGY BOMBAY

Abstract

Prof. Prabhu Ramachandran

Master of Technology

Turbulence Modelling for Smoothed Particle Hydrodynamics

by K T Prajwal Prathiksh

Turbulence modelling is a challenging problem, particularly for a Lagrangian method such as Smoothed Particle Hydrodynamics (SPH) which lacks the years of theoretical and practical research that conventional CFD solvers based on FEM/FVM enjoy. However, work based on translating existing Eulerian-based turbulence methods to SPH and Lagrangian-specific models has started making inroads in the general understanding of the topic in an SPH setting. Ultimately, a rigorous and robust model can be devised, which is suitable for a wide variety of 2D and 3D problems.

This project aims to survey and review the state-of-the-art turbulence models that SPH offers and help subsequently provide a comparative analysis detailing the advantages and limitations of these models. It also intends to extend the best-equipped models to robust and accurate SPH schemes and incorporate some of the latest developments in the field of SPH to refine further the machinery required to model turbulence.

Keywords: Fluid Mechanics, Turbulence Modelling, Smoothed Particle Hydrodynamics, Reynolds Averaging, Large Eddy Simulation, Lagrangian Averaging, Coherent Structures

Acknowledgements

I would like to express my deepest gratitude and appreciation for Prof. Prabhu Ramachandran, my supervisor, for his invaluable guidance and support throughout the process of completing my academic thesis. His expertise, commitment, and insightful feedback have been instrumental in shaping this work and have significantly contributed to my growth as a researcher. His encouragement and patience, particularly during challenging times, have been a source of inspiration and motivation. It proved, indeed, to be a privilege to work under his supervision.

I would also like to sincerely appreciate the academic environment and resources provided by *Indian Institute of Technology Bombay*. The stimulating scholarly community, state-of-the-art facilities, and access to extensive research materials have played an indispensable role in shaping my research journey.

I would like to thank the *Department of Aerospace Engineering* for providing me with the opportunity to pursue my graduate studies. The input and feedback provided by the faculty members have been invaluable in helping me develop my research skills. I must also acknowledge the facilities and resources provided by the *Department of Aerospace Engineering*, particularly the *Aerospace Computational Engine - ACE HPC* cluster, which has been crucial to the completion of this work.

I would also like to thank the members of the lab group headed by Prof. Prabhu Ramachandran for their support and guidance. Amal S Sebastian, Abhinav Muta, Asmelash Haftu, Pawan Negi, and Navaneet (*in no particular order*) helped provide an environment conducive to learning and growth. I must acknowledge their generous sharing of knowledge and encouragement. Their contributions have enriched my research experience and have made this journey more enjoyable.

Lastly, I extend my heartfelt gratitude to my family and friends for their unwavering support, understanding, and patience throughout this academic pursuit. Their unconditional love and encouragement have been my source of strength and motivation.

Contents

Declaration of Authorship	I
Abstract	II
Acknowledgements	III
Contents	IV
List of Figures	VI
List of Symbols	XI
List of Tables	XIV
1 Introduction	1
1.1 Smoothed Particle Hydrodynamics	2
1.2 Project Motivation & Objectives	2
1.3 Report Structure	3
2 Turbulence Modelling	4
2.1 Viscosity-based Models	4
2.1.1 Eddy Viscosity Model	4
2.1.2 Generalized Langevin Model	5
2.1.3 mSPH	6
2.2 Large Eddy Simulation-based Models	9
2.2.1 Implicit Pressure Poisson-based Models	9
2.2.2 Explicit Pressure Equation of State-based Models	14
2.2.2.1 Standard Smagorinsky Model	14
2.2.2.2 Modified Smagorinsky Model	15
2.3 Lagrangian LES-based Models	22
2.3.1 Extension to EDAC-SPH Scheme	26
2.4 RANS-based k-epsilon Models	27
2.5 LANS-based Models	31
2.6 Miscellaneous Models	33
3 Evaluation of Turbulence Models	35
3.1 Benchmark Problems	35
3.1.1 Taylor-Green Vortex Problem	35
3.1.2 Thin Double-Shear Layer	36
3.1.3 3D Isotropic Turbulence	36
3.1.4 2D Confined and Driven Turbulence	36
3.1.5 Free Surface Flows	36
3.2 Post-Simulation Analysis	37

3.2.1	Energy Spectral Density	37
3.2.2	Lagrangian Coherent Structures	38
4	Results	40
4.1	Turbulence-specific Post-processing	40
4.1.1	Energy Spectral Density	41
4.1.2	Finite-time Lyapunov Exponent (FTLE) Field	48
4.2	Turbulence Modelling	51
4.2.1	Implementation of Models	51
4.2.2	L-IPST-C Scheme	52
4.2.3	SPH-LES Scheme	53
4.2.4	delta-LES-SPH Scheme	58
4.2.5	k-epsilon SPH Scheme	62
4.2.6	SPH-epsilon Scheme	70
4.3	Long-time Simulations - Taylor-Green Vortex Problem	79
4.4	Externally Forced Variant - Taylor-Green Vortex Problem	87
5	Conclusion & Future Work	96
A	Lagrangian LES Filtering of EDAC	100
	Bibliography	102

List of Figures

1.1	A scanned copy of a part of the first page of the 1887 paper by William Thomson, where the word ' <i>turbulence</i> ', as a noun, is first introduced. Reproduced from Schmitt 2017	2
2.1	Turbulent Poiseuille flow in a pipe ($Re = 6.4 \times 10^4$) modelled using the eddy viscosity model. Computed mean velocity profiles after ($t = 1s$) (solid circles), against theory (solid line). Reproduced from Violeau, Piccon, and Chabard 2002	5
2.2	Turbulent Poiseuille flow in a pipe ($Re = 6.4 \times 10^4$) modelled using the generalised Langevin model. Computed mean velocity profiles after ($t = 1s$) (solid circles), against theory (solid line). Reproduced from Violeau, Piccon, and Chabard 2002	7
2.3	Velocity vector plot at $t = 2$ (left) and $t = 30$ (right). $Re = \infty$. Reproduced from Adami, X. Y. Hu, and N. A. Adams 2012	8
2.4	Comparison of energy spectra $t = 10$. + and \times denote standard SPH results with quintic spline and MLS interpolation; \circ and \square denote mSPH results with quintic spline and MLS interpolation. Reproduced from Adami, X. Y. Hu, and N. A. Adams 2012	8
2.5	Dissipation rate at $Re = 400$ using DNS (solid line), Smagorinsky model (dashed line), standard SPH (+) and mSPH (\circ). Reproduced from Adami, X. Y. Hu, and N. A. Adams 2012	9
2.6	Dissipation rate at $Re = 3000$ using DNS (solid line), Smagorinsky model (dashed line) and mSPH (\circ). Reproduced from Adami, X. Y. Hu, and N. A. Adams 2012	9
2.7	Time sequences of computational and experimental wave profiles near curtain wall (overtopping). Reproduced from Hitoshi Gotoh, Songdong Shao, and Memita 2004	12
2.8	Experimental and computational wave profiles by SPH and MPS model. Reproduced from Songdong Shao and Hitoshi Gotoh 2005	13
2.9	Cylinder distribution and instantaneous velocity overlapped by velocity vectors. Velocity in m/s , at $t = 20s$. The flow direction is from left to right. Reproduced from Canelas et al. 2016	16
2.10	Vorticity field. Vorticity in Hz, at $t = 20s$. Reproduced from Canelas et al. 2016	17
2.11	FTLE field with negative integration time ($T = -0.4s$) (unstable manifolds - attracting LCS) at $t = 20s$. Reproduced from Canelas et al. 2016	17
2.12	Comparison of quantitative metrics for different particle counts N . (a) & (b) Temporal evolution of the density-weighted averaged kinetic energy. (c) & (d) Temporal evolution of the averaged dissipation rate. Reproduced from Okrashevski et al. 2022	19

2.13 Backward FTLE at the plane $z = \pi$ for $N = 2563$ and $t = 14s$ in the range [11; 14]s. (a) Without explicit SFS model. (b) With the SMAG model. (c) With SIGMA model. (d) With the SMAG-MCG model. Reproduced from Okrashevski et al. 2022	20
2.14 Comparison of quantitative metrics for different $N = 256^3$ runs. (a) & (b) Temporal evolution of the density-weighted averaged kinetic energy. (c) & (d) Temporal evolution of the averaged dissipation rate. Reproduced from Okrashevski et al. 2022	21
2.15 2D freely decaying turbulence ($tU/L = 2$, $Re = 1.25 \times 10^5$). Left: Energy spectrum using DNS-SPH. Right: Energy spectrum using LES-SPH. Reproduced from Di Mascio et al. 2017	24
2.16 3D homogeneous turbulence decay. Comparison between DNS-SPH and LES-SPH simulations ($tU/L = 5$). Left: Particle resolution = 64^3 . Right: particle resolution = 128^3 . Reproduced from Di Mascio et al. 2017	25
2.17 Left: Energy spectrum at ($tU/L = 3$, $Re = 1 \times 10^6$) as predicted by the δ -LES-SPH model and a finite volume scheme. Symbols k_f and k_R indicate the wave numbers of the external forcing and the kernel radius, respectively, while k_λ and k_D are the wave numbers associated with the Taylor and Kolmogorov scales. Right: k field at the same instant. Reproduced from Antuono et al. 2021	25
2.18 Left: Time histories of k as predicted by finite volume scheme and the δ -LES-SPH model. Right: Energy spectra. Symbols k_f and k_R denote the wave numbers of the external forcing and the kernel radius, respectively. Reproduced from Antuono et al. 2021	26
2.19 Comparisons of computed water surface elevations by SPH (solid lines) with experimental (\circ) and numerical (dotted lines) data of T. Li, Troch, and De Rouck 2004. Reproduced from Songdong Shao 2006	28
2.20 Comparisons between experimental data (left) and numerical results (right) for turbulence intensity (m/s) at $t = 0.6s$ (top panels) and the corresponding vertical cross-sections (lower panels). In the lower panels, solid lines and \circ represent the numerical and experimental results, respectively. Reproduced from Wang and P. L. Liu 2020	30
2.21 Comparisons of numerical and experimental turbulent kinetic energy in x -direction and y -direction. Reproduced from Wang and P. L. Liu 2020	30
3.1 Viscous flow past a circular cylinder at $Re = 105$. Top: Attracting FTLE contour plot from SPH simulation. Bottom: Photo from experiments conducted by Taneda 1977 with electrolytic precipitation in water technique for vortex street visualisation. Reproduced from Sun, Colagrossi, et al. 2016	39
4.1 Speedup of the 1D energy spectrum computation for various dimensions of the velocity field.	42
4.2 The vector fields $\mathbf{E}(\mathbf{k})$ for 1D and 2D case, with decay rate $\gamma = 0$, and $N = 1$. Note: The plots are shown by shifting the energy spectrum such that the centre of the plot along each axis corresponds to the zero wavenumber for that axis.	43
4.3 The scalar fields $E(k)$ for 1D, 2D, and 3D case, with decay rate $\gamma = 0$, and $N = 1$	44

4.4	The vector fields $\mathbf{E}(\mathbf{k})$ for 1D and 2D case, with decay rate $\gamma = 1$, and $N = n_x/2$. Note: The plots are shown by shifting the energy spectrum such that the centre of the plot along each axis corresponds to the zero wavenumber for that axis.	45
4.5	The scalar fields $E(k)$ for 1D, 2D, and 3D case, with decay rate $\gamma = 1$, and $N = n_x/2$	45
4.6	The scalar fields $E(k)$ for 1D, 2D, and 3D case, for various perturbation amplitudes.	46
4.7	The scalar fields $E(k)$ for 1D, 2D, and 3D case, for various interpolation schemes.	47
4.8	The scalar fields $E(k)$ for 1D, 2D, and 3D case, for various interpolation kernels.	48
4.9	The scalar fields $E(k)$ for 1D, 2D, and 3D case, for various particle resolutions.	49
4.10	Parabolic displacement field	50
4.11	Spiral displacement field	50
4.12	Convergence of the L-IPST-C scheme for various time-integrators.	53
4.13	Run-time (in s) of the L-IPST-C scheme for various time-integrators.	54
4.14	Convergence of the SPH-LES scheme for various f_{pst} values.	54
4.15	Velocity magnitude field for the SPH-LES scheme for various f_{pst} values ($N = 50^2, t_f = 0.1, Re = 10000, c_s = 20$).	55
4.16	Evolution of the energy spectrum for the SPH-LES scheme for various f_{pst} values ($N = 100^2, t_f = 0.1, Re = 10000, c_s = 20$). The initial energy spectrum is plotted in dark blue, and the final energy spectrum is plotted in yellow.	56
4.17	Convergence of the SPH-LES scheme for various speed of sound values.	56
4.18	Velocity magnitude field for the SPH-LES scheme for various speed of sound values ($N = 50^2, t_f = 0.1, Re = 10000, f_{pst} = 10$).	57
4.19	Evolution of the energy spectrum for the SPH-LES scheme for various speed of sound values ($N = 100^2, t_f = 0.1, Re = 10000, f_{pst} = 10$).	57
4.20	Convergence of the δ -LES-SPH (ρ) scheme for various equations of state.	59
4.21	Convergence of the δ -LES-SPH (ρ_c) scheme for various equations of state.	59
4.22	Convergence of the δ -LES-SPH (ρ_c) scheme for various f_{pst} values.	60
4.23	Velocity magnitude field for the δ -LES-SPH (ρ_c) scheme for various f_{pst} values ($N = 50^2, t_f = 0.1, Re = 10000, c_s = 20$).	60
4.24	Evolution of the energy spectrum for the δ -LES-SPH (ρ_c) scheme for various f_{pst} values ($N = 100^2, t_f = 0.1, Re = 10000, c_s = 20$). The initial energy spectrum is plotted in dark blue, and the final energy spectrum is plotted in yellow.	61
4.25	Convergence of the δ -LES-SPH (ρ_c) scheme for various time-integrators.	62
4.26	Run-time (in s) of the δ -LES-SPH (ρ_c) scheme for various time-integrators.	63
4.27	Velocity magnitude field for the δ -LES-SPH (ρ_c) scheme for various time-integrators ($N = 50^2, t_f = 0.1, Re = 10000, c_s = 20, f_{pst} = 10$).	63
4.28	Evolution of the energy spectrum for the δ -LES-SPH (ρ_c) scheme for various time-integrators ($N = 100^2, t_f = 0.1, Re = 10000, c_s = 20, f_{pst} = 10$).	64
4.29	Convergence of the spatial operators in the k transport equation for various test-cases.	66

4.30	Convergence of the spatial operators in the ϵ transport equation for various test-cases.	66
4.31	RHS of the k transport equation for various test-cases ($N = 150^2, t_f = 1\Delta t, Re = 10000, c_s = 60$).	67
4.32	RHS of the ϵ transport equation for various test-cases ($N = 150^2, t_f = 1\Delta t, Re = 10000, c_s = 60$).	68
4.33	Convergence of the $k - \epsilon$ SPH scheme for various equations of state.	69
4.34	Velocity magnitude field for the $k - \epsilon$ SPH scheme for various equations of state ($N = 50^2, t_f = 0.1, Re = 10000, c_s = 20, f_{pst} = 10$).	69
4.35	Evolution of the energy spectrum for the $k - \epsilon$ SPH scheme for various equations of state ($N = 100^2, t_f = 0.1, Re = 10000, c_s = 20, f_{pst} = 10$).	70
4.36	Convergence of the $k - \epsilon$ SPH scheme for various f_{pst} values.	70
4.37	Velocity magnitude field for the $k - \epsilon$ SPH scheme for various f_{pst} values ($N = 50^2, t_f = 0.1, Re = 10000, c_s = 20$).	71
4.38	Evolution of the energy spectrum for the $k - \epsilon$ SPH scheme for various f_{pst} values ($N = 100^2, t_f = 0.1, Re = 10000, c_s = 20$).	71
4.39	Convergence of the SPH- ϵ scheme without and with gradient correction.	72
4.40	Velocity magnitude field for the SPH- ϵ scheme without and with gradient correction ($N = 50^2, t_f = 0.1, Re = 10000, c_s = 20, f_{pst} = 100$).	73
4.41	Evolution of the energy spectrum for the SPH- ϵ scheme without and with gradient correction ($N = 100^2, t_f = 0.1, Re = 10000, c_s = 20, f_{pst} = 100$).	73
4.42	Convergence of the SPH- ϵ scheme for various values of ϵ ($N = 50^2, t_f = 0.1, Re = 10000, c_s = 20, f_{pst} = 100$).	74
4.43	Velocity magnitude field for the SPH- ϵ scheme for various values of ϵ ($N = 50^2, t_f = 0.1, Re = 10000, c_s = 20, f_{pst} = 100$).	75
4.44	Evolution of the energy spectrum for the SPH- ϵ scheme for various values of ϵ ($N = 100^2, t_f = 0.1, Re = 10000, c_s = 20, f_{pst} = 100$).	75
4.45	Convergence of the SPH- ϵ scheme for various equations of state.	76
4.46	Velocity magnitude field for the SPH- ϵ scheme for various equations of state ($N = 50^2, t_f = 0.1, Re = 10000, c_s = 20, f_{pst} = 100$).	76
4.47	Evolution of the energy spectrum for the SPH- ϵ scheme for various equations of state ($N = 100^2, t_f = 0.1, Re = 10000, c_s = 20, f_{pst} = 100$).	77
4.48	Convergence of the SPH- ϵ scheme for various f_{pst} values.	77
4.49	Velocity magnitude field for the SPH- ϵ scheme for various f_{pst} values ($N = 50^2, t_f = 0.1, Re = 10000, c_s = 20$).	78
4.50	Evolution of the energy spectrum for the SPH- ϵ scheme for various f_{pst} values ($N = 100^2, t_f = 0.1, Re = 10000, c_s = 20$).	78
4.51	Evolution of the angular and linear momentum for various schemes ($N = [100^2, 200^2], Re = [10^4, 10^5], c_s = 20$).	80
4.52	Evolution of the kinetic energy and velocity decay for various schemes ($N = [100^2, 200^2], Re = [10^4, 10^5], c_s = 20$).	81
4.53	Evolution of the L_1 error for various schemes ($N = [100^2, 200^2], Re = [10^4, 10^5], c_s = 20$).	82
4.54	Velocity magnitude field (<i>arrows represent the velocity vector</i>) for various schemes ($N = 200^2, t_f = 2, Re = 10^5, c_s = 20$).	82
4.55	Vorticity magnitude field (<i>arrows represent the velocity vector</i>) for various schemes ($N = 200^2, t_f = 2, Re = 10^5, c_s = 20$).	83
4.56	Evolution of the L_1 error (pressure) for various schemes ($N = [100^2, 200^2], Re = [10^4, 10^5], c_s = 20$).	84
4.57	Pressure field for various schemes ($t_f = 2, Re = 10^5, c_s = 20$).	85

4.58 Density field for various schemes ($t_f = 2, Re = 10^5, c_s = 20$).	86
4.59 Evolution of the energy spectrum for various schemes ($N = 200^2, t_f = 2, Re = 10^5, c_s = 20$).	87
4.60 Evolution of the kinetic energy for the externally-forced TGV problem ($N = [100^2, 200^2], Re = [10^4, 10^5, 10^6], c_s = 20$). Compared with data obtained from Antuono et al. 2021.	89
4.61 Evolution of the energy spectrum for the externally-forced TGV problem ($N = 200^2, t_f = 3, Re = 10^6, c_s = 20$). Compared with data obtained from Antuono et al. 2021.	91
4.62 Comparison between expected velocity magnitude field (Antuono et al. 2021), and the computed velocity magnitude field for the externally-forced TGV problem ($N = 200^2, t_f = 1.92, Re = 10^6, c_s = 20$).	92
4.63 Comparison between expected ω_z field (Antuono et al. 2021), and the computed ω_z field for the externally-forced TGV problem ($N = 200^2, t_f = 1.92, Re = 10^6, c_s = 20$).	93
4.64 Comparison between expected pressure field (Antuono et al. 2021), and the computed pressure field for the externally-forced TGV problem ($N = 200^2, t_f = 1.92, Re = 10^6, c_s = 20$).	94
4.65 Evolution of the angular and linear momentum for the externally-forced TGV problem ($N = [100^2, 200^2], Re = [10^4, 10^5, 10^6], c_s = 20$).	95

List of Symbols

Symbol	Description
\mathbf{a}	Vector Field
$\underline{\mathbf{A}}$	Second-rank Tensor Field
$\underline{\mathbf{I}}$	Identity Tensor
$\hat{\mathbf{e}}_i$	i^{th} Basis
\otimes	Tensor Product
$\frac{D(\cdot)}{Dt}$	Lagrangian Derivative
$\langle \underline{\mathbf{A}}, \underline{\mathbf{B}} \rangle$	Frobenius Inner Product of $\underline{\mathbf{A}}$ and $\underline{\mathbf{B}}$
$\ \mathbf{A}\ _F$	Frobenius Norm of \mathbf{A} ($= \sqrt{\langle \mathbf{A}, \mathbf{A} \rangle}$)
∇^2	Laplacian Operator
$\Delta(\cdot)$	Component-wise Laplacian Operator
$(1 - \alpha^2 \Delta)$	Helmholtz Operator
i	Reference Particle
j	Neighbouring Particle
$(\dots)_i$	Property of i^{th} SPH particle
$(\dots)_j$	Property of j^{th} SPH particle
$(\dots)_{ij}$	$(\dots)_i - (\dots)_j$
n_{dim}	Number of spatial dimensions for a given problem
t	Time
\mathbf{r}	Position = (x, y, z)
\mathbf{v}	Velocity = (v_x, v_y, v_z)
m	Mass
P	Pressure

Table 1 continued from previous page

Symbol	Description
ρ	Density
$(\dots)_0$	Initial Condition ($t = 0$) of Specified Property
Δt	Time Step
Δx	Inter Particle Spacing
$\delta(x)$	Dirac Delta Function
W_h	SPH Interpolating Kernel
h	Kernel Smoothing Length
$W_{h,ij}$	$W(\mathbf{r}_{ij} , h)$
$\nabla_i W_{h,ij}$	$\nabla_i W(\mathbf{r}_{ij}, h) = \frac{\mathbf{r}_{ij}}{ \mathbf{r}_{ij} } \frac{\partial W_{h,ij}}{\partial r_i}$
\mathcal{V}_i	Volume of i^{th} SPH particle
φ_i	Particle Density of i^{th} SPH particle
\mathbf{F}	External Body Force
ν	Kinematic Viscosity
η	Dynamic Viscosity ($= \nu\rho$)
ξ	Machine Epsilon
M_o	Reference Mass
P_o	Reference Pressure
ρ_o	Reference Density
c_s	Speed of Sound
γ	Exponent - Equation of State
$\boldsymbol{\omega}$	Vorticity ($= \nabla \times \mathbf{v}$)
ν_t	Turbulent Eddy Viscosity
\underline{S}	Strain-Rate Tensor ($= [1/2][\nabla \mathbf{v} + \nabla \mathbf{v}^T]$)
\underline{R}	Rate of Rotation Tensor ($= [1/2][\nabla \mathbf{v} - \nabla \mathbf{v}^T]$)
ϵ	Turbulent Dissipation Rate
k	Turbulent Kinetic Energy

Table 1 continued from previous page

Symbol	Description
$\underline{\tau}$	Stress Tensor
C_s	Smagorinsky Constant
u_{max}	Maximum Particle Velocity
ε	Smoothing Parameter (XSPH)
k	Wave Number

List of Tables

4.1	Implementation of representative turbulence models.	51
4.2	Optimised SPH schemes for each category of turbulence model.	79

1 Introduction

Turbulence is the most important unsolved problem of classical physics.

Richard Feynman

Turbulent flows have long been a phenomenon that is surprisingly easy to detect and observe in the natural world but unmistakably challenging to understand and model in sufficient detail, unlike other problems in classical physics. The fundamental aspects of turbulent flow consisting of eddies of various length scales had long been observed, as reflected in the 16th century diagrams by Leonardo Da Vinci consisting of water flow in streams and channels. It took the work of Osborne Reynolds on his averaging of the Navier-Stokes (NS) equations and William Thomson's (Lord Kelvin) work on flow along an inclined plane (see Fig. 1.1) for *turbulence* to enter the parlance of the larger scientific community. This allowed turbulence to be recognised as a new subfield of fluid mechanics.

However, further strides in the field have remained arduous despite the Navier-Stokes equations being written down in the early 19th century. There is consensus that this remarkable failure of some of the greatest scientific minds in providing an intricate understanding of turbulence points to an inadequacy of the mathematical tools we have at our disposal. Even the current machinery cannot deal with the strong non-linearity of the equations coupled with the characteristic tendency of flows to degenerate into some form of instability.

Turbulence is caused by excessive kinetic energy in parts of a fluid flow that can overcome the damping effect of the fluid's viscosity. Its onset can be predicted by the dimensionless Reynolds number, which is the ratio of kinetic energy to viscous damping in a fluid flow.

The criteria for defining a flow as turbulent are varied and ambiguous since there is no explicit definition for it. However, the most often used criteria for qualifying a flow as turbulent is given below (Sagaut 2002):

- random character of the spatial and temporal fluctuations of the velocities, which reflect the existence of finite characteristic scales of statistical correlation;
- velocity field is three-dimensional and rotational;
- various modes are strongly coupled, which is reflected in the non-linearity of the NS equations;
- large mixing capacity due to the agitation induced by the various scales;
- chaotic character of the solution, which exhibits a powerful dependency on the initial condition and boundary conditions.

[272]

XXXIV. Stability of Motion (continued from the May, June, and August Numbers).—Broad River flowing down an Inclined Plane Bed. By Sir WILLIAM THOMSON, F.R.S.*

41. CONSIDER now the second of the two cases referred to in § 27—that is to say, the case of water on an inclined plane bottom, under a fixed parallel plane cover (ice, for example), both planes infinite in all directions and gravity everywhere uniform. We shall include, as a sub-case, the icy cover moving with the water in contact with it, which is particularly interesting, because, as it annuls tangential force at the upper surface, it is, for the steady motion, the same case as that of a broad open river flowing uniformly over a perfectly smooth inclined plane bed. It is not the same, except when the motion is steadily laminar, the difference being that the surface is kept rigorously plane, but not free from tangential force, by a rigid cover, while the open surface is kept almost but not quite rigorously plane by gravity, and rigorously free from tangential force. But, provided the bottom is smooth, the smallness of the dimples and little round hollows which we see on the surface, produced by turbulence (when the motion is turbulent), seems to prove that the motion must be very nearly the same as it would be if the upper surface were kept rigorously plane, and free from tangential force.

Figure 1.1: A scanned copy of a part of the first page of the 1887 paper by William Thomson, where the word ‘turbulence’, as a noun, is first introduced. Reproduced from Schmitt 2017

1.1 Smoothed Particle Hydrodynamics

Smoothed particle hydrodynamics (SPH) is a technique for problem-solving in *Computational Continuum Dynamics* (CCD). This technique approximates numerical solutions of the equations of fluid dynamics by replacing the fluid with a set of particles. The equations of motion and properties of these particles are determined from the continuum equations of fluid dynamics. They are subsequently discretised based on the particles’ interpolant data. The interpolant can be constructed using analytical functions, and spatial derivatives of the interpolated quantities can then be found using ordinary calculus. There is no need to use a grid, and the description of free surfaces, however complicated, is trivial.

Therefore, this *Lagrangian* based particle formulation uses no background spatial mesh. Since there is no mesh to distort, the method can handle large deformations in a pure Lagrangian frame. Thus, material interfaces can be modelled naturally, and complex constitutive behaviour can be implemented relatively quickly. This allows SPH to have diverse and fascinating applications in various domains that extend beyond the astrophysical and cosmological problems it was initially designed to tackle.

1.2 Project Motivation & Objectives

Despite the success of SPH in simulating transient flows, a robust or rigorous model of turbulence does not seem to exist. Some of the models in use cannot be generalised to a wide variety of turbulence-based problems or scaled to 3D-flows. This

limits SPH's applicability in turbulent flows where conventional FEM/FVM-based CFD solvers have the upper hand, owing to their sophisticated models.

This project aims to survey and review the current state of the art regarding turbulence modelling in SPH and subsequently provide a framework to help establish the advantages and limitations of such models, using a comparative analysis between the major class of models. After that, it is intended to extend the most well-equipped models to robust and accurate SPH schemes (which might not have been the case in the author/s original work) for bounded flows specifically. Such an exercise is expected to either improve the original model or expose any underlying limitations in its assumptions or discretisation.

1.3 Report Structure

The report is structured to present the turbulence models developed for SPH in [Chapter 2](#). Here, the models have been categorised by the fundamental ideas on which they were based. In [Chapter 3](#), research on analysing turbulence through standard benchmarks problems and methods of quantifying turbulence data is presented. Subsequently, the implementation of the models, and their results are presented in [Chapter 4](#). Finally, the project conclusion and future work are presented in [Chapter 5](#).

2 Turbulence Modelling

2.1 Viscosity-based Models

Violeau, Piccon, and Chabard 2002 were amongst the early pioneers who tried to incorporate a turbulence model in SPH. They came up with two techniques to tackle the problem of turbulence in a Lagrangian framework, which so far had been neglected till then in research, namely, the eddy viscosity model and a generalised Langevin model. For each of their techniques, they considered the following equation of state:

$$P_i = B \left[\left(\frac{\rho_i}{\rho_o} \right)^\gamma - 1 \right] , \quad B = \frac{\rho_o c_s^2}{\gamma}, \quad (2.1)$$

where, (P, ρ) denotes pressure and density respectively. $(\dots)_i$ denotes the property of the i^{th} SPH particle, $(\dots)_o$ denotes the reference quantities, and (c_s) denotes the speed of sound. The continuity equation is given below:

$$\frac{D\rho_i}{Dt} = \sum_j m_j \mathbf{v}_{ij} \cdot \nabla_i W_{h,ij}, \quad (2.2)$$

where $\left[\frac{D(\cdot)}{Dt} \right]$ denotes the Lagrangian derivative, and (m, \mathbf{v}) represent the mass and velocity respectively. Here we adopt the nomenclature of $(\dots)_{ij}$ to denote the difference of a specified property between the i^{th} and j^{th} SPH particle $[(\dots)_i - (\dots)_j]$, and $(\nabla_i W_{h,ij})$ denotes $[\nabla_i W(\mathbf{r}_{ij}, h) = \frac{\mathbf{r}_{ij}}{|\mathbf{r}_{ij}|} \frac{\partial W_{h,ij}}{\partial r_i}]$, where (h) is the kernel smoothing length. The momentum equation, based on the work of J. J. Monaghan 1992, is given below:

$$\frac{D\mathbf{v}_i}{Dt} = - \sum_j m_j \left(\frac{P_i}{\rho_i^2} + \frac{P_j}{\rho_j^2} + \Pi_{ij} \right) \nabla_i W_{h,ij} + \mathbf{F}_i, \quad (2.3)$$

where (\mathbf{F}) is the external body force, and the viscous term (Π) is defined as:

$$\Pi_{ij} = - \frac{16\nu}{\rho_i + \rho_j} \frac{\mathbf{v}_{ij} \cdot \mathbf{r}_{ij}}{|\mathbf{r}_{ij}|^2 + \xi^2}, \quad (2.4)$$

here (ν) is the kinematic viscosity, and (ξ) is the machine epsilon.

2.1.1 Eddy Viscosity Model

The eddy viscosity model was devised as a first-order closure model, which consisted of a relationship between the Reynolds stress tensor and the mean velocity gradients. Therefore, the momentum equation is similar to the equation in Eq. 2.3, except that the kinematic viscosity is replaced by the eddy viscosity (ν_t), and the velocities are Reynolds-averaged. In the SPH formalism, the diffusion term occurring is therefore defined as given in Eq. 2.5, with the eddy viscosity defined according to

Eq. 2.6, which are given below:

$$\tilde{\Pi}_{ij} = -8 \frac{\nu_{t,i} + \nu_{t,j}}{\rho_i + \rho_j} \frac{\langle \mathbf{v} \rangle_{ij} \cdot \mathbf{r}_{ij}}{|\mathbf{r}_{ij}|^2 + \zeta^2}, \quad (2.5)$$

$$\nu_t = L_m^2 \|\underline{S}\|_F = L_m^2 \sqrt{\langle \underline{S}, \underline{S} \rangle}, \quad (2.6)$$

where $\langle \mathbf{v} \rangle$ is Reynolds-averaged velocity, L_m refers to the mixing length scales, and (\underline{S}) is the strain-rate tensor ($= [1/2][\nabla \mathbf{v} + \nabla \mathbf{v}^T]$), where we adopt the nomenclature of (\underline{A}) to represent a second-rank tensor field. Also, here $(\langle \underline{A}, \underline{B} \rangle)$ denotes the Frobenius inner product of \underline{A} and \underline{B} , and $(\|\underline{A}\|_F)$ denotes the Frobenius norm of \underline{A} ($= \sqrt{\langle \underline{A}, \underline{A} \rangle}$). The SPH formulation for the mean velocity gradients is given below:

$$\nabla \langle \mathbf{v} \rangle_i = -\frac{1}{\rho_i} \sum_j m_j \langle \mathbf{v} \rangle_{ij} \otimes \nabla_i W_{h,ij}, \quad (2.7)$$

where (\otimes) denotes the tensor product.

On simulating Poiseuille flow for a high Reynolds number case, the authors could show that the velocity profile showed only a slight discrepancy with theory, with the expected log-law profile near the walls Fig. 2.1. This indicated that the model is appropriate for turbulent mixing problems or for cases involving spatially-varying viscosity while restricted to shear flows.

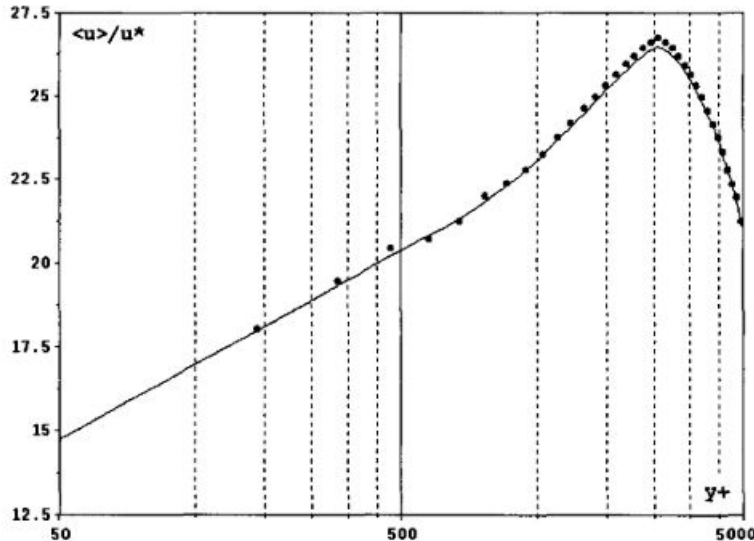


Figure 2.1: Turbulent Poiseuille flow in a pipe ($Re = 6.4 \times 10^4$) modelled using the eddy viscosity model. Computed mean velocity profiles after ($t = 1s$) (solid circles), against theory (solid line). Reproduced from Violeau, Piccon, and Chabard 2002

2.1.2 Generalized Langevin Model

Violeau, Piccon, and Chabard 2002 also considered a stochastic approach, where the main idea is built on the concept of prescribing particle velocities as a random process, with properties fulfilling the theoretical turbulence hypotheses (S. Pope 1994).

Hence, came about the Generalised Langevin model (GLM), where the particle acceleration is defined as:

$$d\mathbf{v} = -\frac{1}{\rho} \nabla \langle P \rangle + \underline{\mathbf{G}}(\mathbf{v} - \langle \mathbf{v} \rangle) dt + \sqrt{C_0 \epsilon dt} \vec{\xi}, \quad (2.8)$$

where $\vec{\xi}$ is a random vector statistically non-correlated with velocities. The closure for this model was defined by specifying $\underline{\mathbf{G}}$ as:

$$\underline{\mathbf{G}} = \frac{1}{2} C_1 \frac{\epsilon}{k} \mathbf{I} + C_2 \nabla \langle \mathbf{v} \rangle, \quad (2.9)$$

where (k) is the turbulent kinetic energy, (ϵ) the dissipation rate, and (C_i) being constants - ($C_1 = 1.8, C_2 = 0.6$). (\mathbf{I}), here, denotes the identity tensor. By modelling turbulence as GLM in SPH, the momentum equation derived was given by:

$$\frac{D \mathbf{v}_i}{Dt} = - \sum_j m_j \left(\frac{\langle P \rangle_i}{\rho_i^2} + \frac{\langle P \rangle_j}{\rho_j^2} \right) \nabla_i W_{h,ij} - \frac{1}{2} C_1 \frac{\epsilon_i}{k_i} \mathbf{v}'_i + C_2 \nabla \langle \mathbf{v} \rangle_i \cdot \mathbf{v}'_i + \sqrt{\frac{C_0 \epsilon_i}{\Delta t}} \vec{\xi}_i, \quad (2.10)$$

$$\langle \mathbf{v} \rangle = \sum_j \frac{m_j}{\rho_j} \mathbf{v}_j W_h(\mathbf{r}_j), \quad (2.11)$$

where the fluctuations are defined as $\mathbf{v}' = \mathbf{v} - \langle \mathbf{v} \rangle$, and the local values of turbulent kinetic energy and dissipation rate are:

$$\epsilon_i = 2\nu_{t,i} + \|\underline{\mathbf{S}}_i\|_F^2, \quad (2.12)$$

$$k_i = \frac{\epsilon_i \nu_{t,i}}{C_\mu} \quad , \quad C_\mu = 0.009. \quad (2.13)$$

It is to be noted that the authors did not estimate the dissipation rate through the proper velocity gradients since the fluctuations of random velocities do not reproduce the small eddies. The same test case as mentioned in Sec. 2.1.1 was considered for the performance of GLM. The authors observed large fluctuations. They attributed the discrepancy to the mean operator being redefined as given by Eq. 2.11 instead of being a Reynolds average. In fact, by redefining the mean operator in such a fashion, they appeared to have constructed a rudimentary LES filter. As observed in Fig. 2.2, the fluctuations have an order of magnitude of $k^{1/2}$. However, as claimed by the authors, unlike the eddy viscosity model, the GLM method can be used for different flows instead of being restricted to only shear flows.

2.1.3 mSPH

Adami, X. Y. Hu, and N. A. Adams 2012 devised a model built on their observation of SPH simulations, wherein the absence of viscosity in typical SPH formulations produced purely noisy particle motion. At finite viscosities, the method would over-predict dissipation. Hence to counter this, they essentially “modified” (hence the name: Modified SPH [mSPH]) the momentum equation and the equation of state to advect the particles in order to homogenise the particle distribution, in turn stabilising the numerical scheme. They were also able to reduce the artificial dissipation in transitional flows.

The authors considered summation density (Eq. 2.15), which is a function of the volume of the respective SPH particle as given by Eq. 2.14, as opposed to evolving

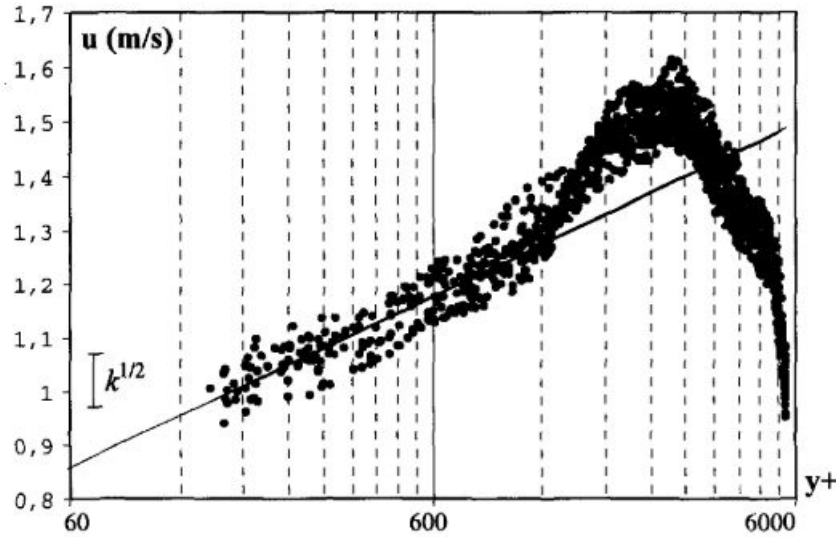


Figure 2.2: Turbulent Poiseuille flow in a pipe ($Re = 6.4 \times 10^4$) modelled using the generalised Langevin model. Computed mean velocity profiles after ($t = 1s$) (solid circles), against theory (solid line).
Reproduced from Violeau, Piccon, and Chabard 2002

density through the continuity equation (Xiang Yu Hu and Nikolaus A Adams 2006). The modified equation of state as given by Eq. 2.16, is equivalent to the classical SPH equation-of-state with $\gamma = 1$.

$$\mathcal{V}_i = \frac{1}{\sum_j W_{h,ij}}, \quad (2.14)$$

$$\rho_i = \frac{m_i}{\mathcal{V}_i} = m_i \sum_j W_{h,ij}, \quad (2.15)$$

$$P_i = c_s^2 (\rho_i - \rho_o), \quad (2.16)$$

where (\mathcal{V}) represents the volume of a particle.

The momentum equation, which provides the acceleration of the particle, is a function of just the gradient and viscous shear forces as given by Eq. 2.17. The corresponding SPH formulation was derived as given by Eq. 2.18, which built on the earlier work of X. Hu and Nikolaus A Adams 2007.

$$\frac{D\mathbf{v}}{Dt} = -\frac{1}{\rho} \nabla P + \nu \Delta(\mathbf{v}) + \mathbf{F}, \quad (2.17)$$

$$\frac{D\mathbf{v}_i}{Dt} = -\frac{1}{m_i} \sum_j (\mathcal{V}_i^2 + \mathcal{V}_j^2) \frac{P_i \rho_j + P_j \rho_i}{\rho_i + \rho_j} \nabla_i W_{h,ij} - \frac{\eta}{m_i} \sum_j (\mathcal{V}_i^2 + \mathcal{V}_j^2) \frac{\mathbf{v}_{ij}}{|\mathbf{r}_{ij}|} \nabla_i W_{h,ij} + \mathbf{F}_i, \quad (2.18)$$

where $[\Delta()]$ denotes the component-wise Laplacian operator, and (η) is the dynamic viscosity.

This scheme takes advantage of the regularisation of the particle motion stemming from the additional background pressure ($P_o = \rho_o c_s^2$). The additional force exerted by the background pressure counteracts non-homogeneous particle distributions, therein reducing numerical dissipation.

The authors estimated the energy spectra of the flow simulations in order to analyse the results of their test cases, using first and second-order moving-least-squares (MLS) method (Gossler 2001) and its subsequent Fourier transform (Frigo and Johnson 2005). Their first test case, the 2D variant of the Taylor-Green Vortex (TGV) problem, involved 8×8 counter-rotating vortices, requiring 64^2 particles. They considered the viscosity to be zero. As seen in the time evolution of the

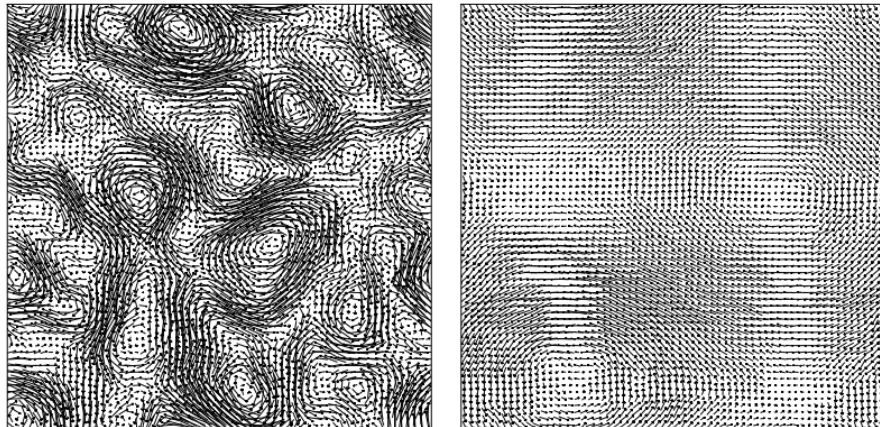


Figure 2.3: Velocity vector plot at $t = 2$ (left) and $t = 30$ (right).
 $Re = \infty$. Reproduced from Adami, X. Y. Hu, and N. A. Adams 2012

The time evolution of the velocity field is given in Fig. 2.3, where it can be observed that the 2D turbulence is characterised by merging and pairing of small vortices. The energy spectra given in Fig. 2.4 show that at low wave numbers, both interpolation schemes give the same results, but at high wave numbers, the results differ. The energy spectrum of the standard SPH has a linear slope of magnitude $m = 1$ in a log-log scale equivalent to a purely noisy velocity field. Theoretically, however, 2D turbulence has an energy cascade with a slope of $m = -3$ in the inertial range, which is reasonably predicted using mSPH.

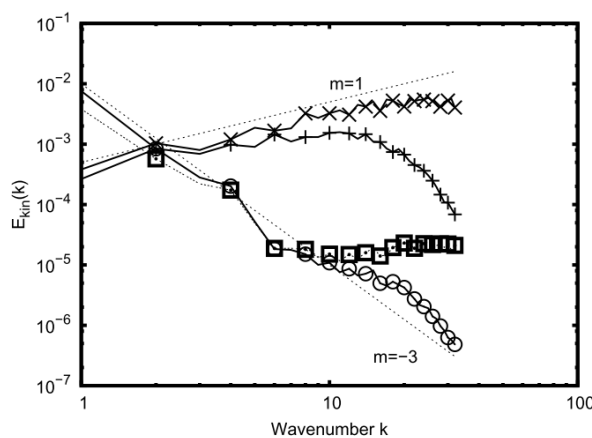


Figure 2.4: Comparison of energy spectra $t = 10$. + and \times denote standard SPH results with quintic spline and MLS interpolation; \circ and \square denote mSPH results with quintic spline and MLS interpolation. Reproduced from Adami, X. Y. Hu, and N. A. Adams 2012

The second test case employed by the authors was that of the 3D TGV problem requiring 64^3 particles for a wide range of Reynolds numbers. The dissipation rate of the flow simulations are shown in Fig. 2.5 and Fig. 2.6. It can be observed that the standard SPH is unable to simulate transitional flows due to excessive dissipation. In contrast, mSPH can reproduce the dissipation rate reasonably well. This implies that the corrected particle transport velocity is an analogous eddy-viscosity model on scales below the numerical resolution.

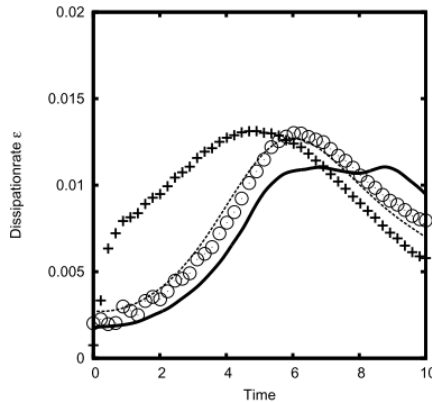


Figure 2.5: Dissipation rate at $Re = 400$ using DNS (solid line), Smagorinsky model (dashed line), standard SPH (+) and mSPH (○).

Reproduced from Adami, X. Y. Hu, and N. A. Adams 2012

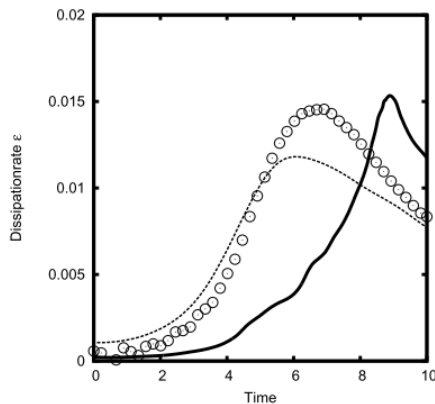


Figure 2.6: Dissipation rate at $Re = 3000$ using DNS (solid line), Smagorinsky model (dashed line) and mSPH (○). Reproduced from

Adam, X. Y. Hu, and N. A. Adams 2012

2.2 Large Eddy Simulation-based Models

2.2.1 Implicit Pressure Poisson-based Models

Hitoshi Gotoh, Songdong Shao, and Memita 2004 were amongst the first to integrate Large Eddy Simulation techniques with the SPH method. They derived this LES-SPH model, based on incompressible flow, to tackle the problem of reflection and transmission characteristics of regular waves by a partially immersed curtain-type breakwater. In order to compare the dissipation efficiencies, they considered the non-overtopping and overtopping cases of the problem.

The governing equations of the system were described as given by the continuity equation in Eq. 2.19 and the momentum equation in Eq. 2.17.

$$\frac{1}{\rho} \frac{D\rho}{Dt} + \nabla \cdot \mathbf{v} = 0. \quad (2.19)$$

The LES mass and momentum conservation equations for the flow were derived by filtering the respective equations using a spatial filter $\overline{(...)}$ to obtain their filtered counterparts as given by Eq. 2.20 and Eq. 2.21 respectively.

$$\frac{1}{\rho} \frac{D\rho}{Dt} + \nabla \cdot \bar{\mathbf{v}} = 0, \quad (2.20)$$

$$\frac{D\bar{\mathbf{v}}}{Dt} = -\frac{1}{\rho} \nabla \bar{P} + \nu \Delta(\bar{\mathbf{v}}) + \frac{1}{\rho} \nabla \cdot \underline{\tau} + \mathbf{F}, \quad (2.21)$$

$$\frac{1}{\rho} \underline{\tau} = \bar{\mathbf{v}} \otimes \bar{\mathbf{v}} - \overline{\mathbf{v} \otimes \mathbf{v}}. \quad (2.22)$$

The stress tensor ($\underline{\tau}$) defined in Eq. 2.22 is closed using Boussinesq's Hypothesis as defined below:

$$\frac{1}{\rho} \underline{\tau} = 2\nu_t \underline{S} - \frac{2}{3} k \underline{I}. \quad (2.23)$$

The turbulent eddy viscosity is estimated using a modified Smagorinsky model as given in Eq. 2.24. This allows wall effects to be incorporated into the model, which was required by the authors to tackle the problem they were working on.

$$\nu_t = \min(C_s \Delta x, \kappa d_{wall})^2 \sqrt{2 \langle \underline{S}, \underline{S} \rangle}, \quad (2.24)$$

$$C_s = 0.1, \quad \kappa = 0.4, \quad (2.25)$$

where (C_s) is the Smagorinsky constant, (κ) is the von Karman constant, d_{wall} is the normal distance of the particle to the closest wall, and (Δx) is the inter-particle spacing.

The first term in Eq. 2.24 dominates the flow far away from the solid wall, thereby recovering the standard Smagorinsky model. However, the second term dominates for flow close to the wall; hence, the eddy viscosity is a function of the particle distance to the wall. This overcomes the disadvantage of the standard Smagorinsky being over-dissipative inside the laminar layer.

In order to solve the system of equations and evolve them in time, the authors employed the Predictive-Corrective time integrator, similar to the two-step projection method of Chorin 1968. The prediction stage is outlined by Eq. 2.26 - Eq. 2.28, where (δt) denotes the time step.

$$\Delta \mathbf{v}_* = \left(\nu \Delta(\bar{\mathbf{v}}) + \frac{1}{\rho} \nabla \cdot \underline{\tau} + \mathbf{F} \right) \Delta t, \quad (2.26)$$

$$\mathbf{v}_* = \mathbf{v}_t + \Delta \mathbf{v}_*, \quad (2.27)$$

$$\mathbf{r}_* = \mathbf{r}_t + \mathbf{v}_* \Delta t. \quad (2.28)$$

The correction stage is outlined by Eq. 2.29 - Eq. 2.32. (\bar{P}) which is required to update the (\mathbf{v}_{t+1}) term is calculated implicitly from Eq. 2.30, which is based on the filtered continuity equation given by Eq. 2.20 and assuming incompressibility $\frac{D\rho}{Dt} = 0$.

$$\Delta\mathbf{v}_{**} = -\frac{1}{\rho}\nabla\bar{P}_{t+1}\Delta t, \quad (2.29)$$

$$\nabla \cdot \left(\frac{1}{\rho_*} \nabla \bar{P}_{t+1} \right) = \frac{\rho_o - \rho_*}{\rho_o \Delta t^2}, \quad (2.30)$$

$$\mathbf{v}_{t+1} = \mathbf{v}_* + \Delta\mathbf{v}_{**}, \quad (2.31)$$

$$\mathbf{r}_{t+1} = \mathbf{r}_t + (\mathbf{v}_t + \mathbf{v}_{t+1}) \frac{\Delta t}{2}. \quad (2.32)$$

In order to solve the system of equations given by Eq. 2.26 - Eq. 2.32 in an SPH setting, the authors presented the following SPH formulation for the flow property. The fluid density is given using a simple summation density given below:

$$\rho_i = \sum_j m_j W_{h,ij}. \quad (2.33)$$

The pressure gradient term is defined in a symmetric form, as given below:

$$\left(\frac{1}{\rho} \nabla \bar{P} \right)_i = \sum_j m_j \left(\frac{\bar{P}_i}{\rho_i^2} + \frac{\bar{P}_j}{\rho_j^2} \right) \nabla_i W_{h,ij}. \quad (2.34)$$

The divergence of \mathbf{v} is also defined symmetrically as given as:

$$\nabla \cdot \bar{\mathbf{v}}_i = \rho_i \sum_j m_j \left(\frac{\bar{\mathbf{v}}_i}{\rho_i^2} + \frac{\bar{\mathbf{v}}_j}{\rho_j^2} \right) \cdot \nabla_i W_{h,ij}. \quad (2.35)$$

The pressure Laplacian, defined in Eq. 2.36, is formulated as a hybrid of a standard SPH first derivative with a finite difference approximation for the first derivative to aid particle pressure stability (Cummins and Rudman 1999).

$$\nabla \cdot \left(\frac{1}{\rho} \nabla \bar{P} \right)_i = \sum_j m_j \frac{8}{(\rho_i + \rho_j)^2} \frac{\bar{P}_{ij} \mathbf{r}_{ij} \cdot \nabla_i W_{h,ij}}{|\mathbf{r}_{ij}|^2}. \quad (2.36)$$

The divergence of the stress tensor is defined as:

$$\left(\frac{1}{\rho} \nabla \cdot \underline{\tau} \right)_i = \sum_j m_j \left(\frac{1}{\rho_i^2} \underline{\tau}_i + \frac{1}{\rho_j^2} \underline{\tau}_j \right) \cdot \nabla_i W_{h,ij}. \quad (2.37)$$

Finally, the laminar stress term, consisting of the velocity Laplacian term, is defined as:

$$(\nu \Delta(\bar{\mathbf{v}}))_i = \sum_j m_j \frac{4(\eta_i + \eta_j)}{(\rho_i + \rho_j)^2} \frac{\bar{\mathbf{v}}_{ij} \mathbf{r}_{ij} \cdot \nabla_i W_{h,ij}}{|\mathbf{r}_{ij}|^2}. \quad (2.38)$$

The authors used this SPH-LES model to investigate the wave interaction with a partially immersed breakwater and compared the results with experimentally obtained values of a similar setup. Their computational domain was 2D populated by $\approx 1.2 \times 10^4$ particles.

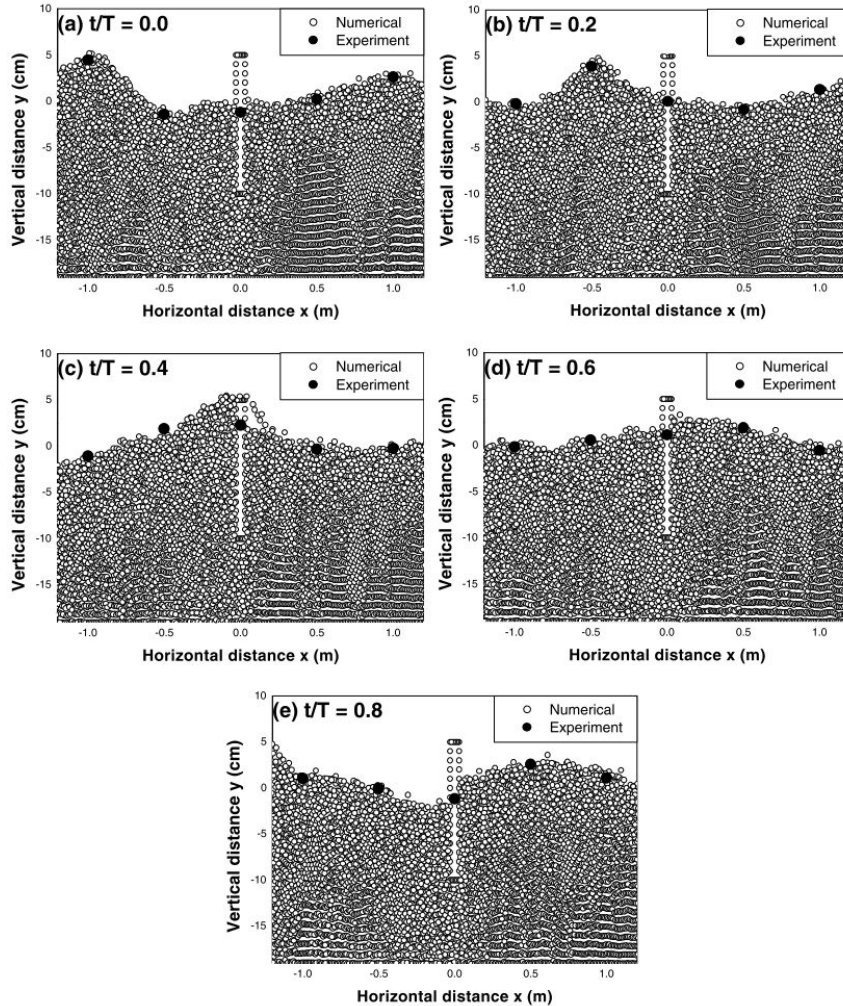


Figure 2.7: Time sequences of computational and experimental wave profiles near curtain wall (overtopping). Reproduced from Hitoshi Gotoh, Songdong Shao, and Memita 2004

As observed in the comparative plots given in Fig. 2.7, the model proves to be accurate in tracking free surfaces of large deformation without numerical diffusion. The authors also observed the model's capability to simulate turbulence and eddy vortices realistically near the curtain wall. However, the authors also conclude that a more refined turbulence model will be required for further accuracy in predicting flow involving wave interactions.

Building on the work mentioned above, Songdong Shao and Hitoshi Gotoh 2005 performed a comparative study of SPH and the Moving Particle Semi-Implicit (MPS) method coupled with an LES model. They also validated these models against experimental data.

The filtered conservation equations which the authors considered were the same as given by Eq. 2.20 - Eq. 2.23. However, they incorporated the standard Smagorinsky model (Smagorinsky 1963) given by Eq. 2.39 as opposed to the modified model Eq.

2.24.

$$\nu_t = (C_s \Delta x)^2. \quad (2.39)$$

The authors consider the same predictive-corrective scheme to evolve their system as detailed in Eq. 2.26 - Eq. 2.32. Similarly, they follow the same SPH formulation outlined in Eq. 2.33 - Eq. 2.38. They do however, slightly modify the pressure and velocity Laplacian terms as given below:

$$(\nabla^2 P)_i = \sum_j m_j \frac{4}{\rho_i + \rho_j} \frac{P_{ij} \mathbf{r}_{ij} \cdot \nabla_i W_{h,ij}}{|\mathbf{r}_{ij}|^2} \quad (2.40)$$

$$(\nu \Delta(\mathbf{v}))_i = \sum_j m_j \frac{2(\nu_i + \nu_j)}{\rho_i + \rho_j} \frac{\mathbf{v}_{ij} \mathbf{r}_{ij} \cdot \nabla_i W_{h,ij}}{|\mathbf{r}_{ij}|^2}. \quad (2.41)$$

The authors validated this SPH-LES Model using experimental data from the experimental data corresponding to a solitary wave breaking on the beach (Synolakis 1986). Their computational domain was 2D and consisted of $\approx 1.8 \times 10^4$ particles. From the computed wave profiles shown in Fig. 2.8, it can be visually observed that there is reasonable agreement between the experimental and computation data. This verifies the model's accuracy in tracking free surfaces with less or no numerical diffusion. Furthermore, by performing a convergence study of the SPH-LES model using the dam-break problem, the authors could show that the scheme's spatial and temporal accuracy is $O(\Delta t + \Delta x^{1.25})$.

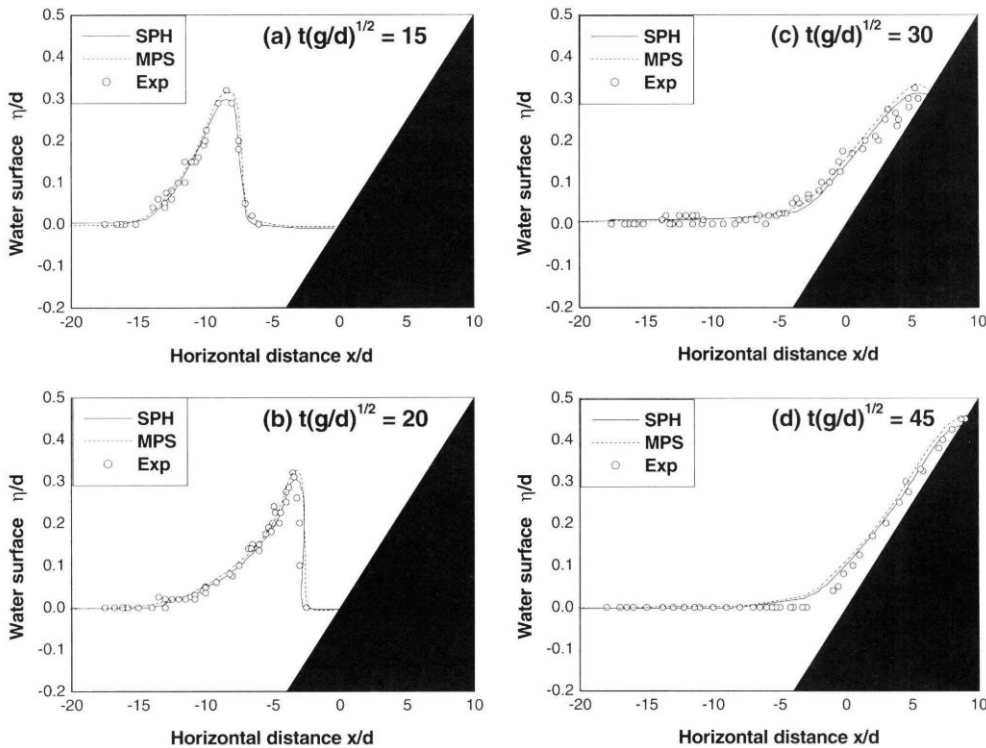


Figure 2.8: Experimental and computational wave profiles by SPH and MPS model. Reproduced from Songdong Shao and Hitoshi Gotoh 2005

2.2.2 Explicit Pressure Equation of State-based Models

2.2.2.1 Standard Smagorinsky Model

Benedict D. Rogers and Robert A. Dalrymple 2005, similar to the work on SPH-LES modelling detailed in Sec. 2.2.1, came up with an LES-type sub-particle-scale (SPS) formulation based on the weakly compressible assumption in order to develop a turbulence model for SPH.

The authors considered the mass and momentum conservation equations as already given in Eq. 2.19 and Eq. 2.17 respectively, along with the equation of state Eq. 2.1. However, for the value of (B) in the state equation, the authors considered the definition given below:

$$B' = 10u_{max}, \quad (2.42)$$

where (u_{max}) is the maximum particle velocity.

They subsequently filtered the compressible conservation equations using Favre averaging as given by:

$$\tilde{f} = \frac{\overline{\rho f}}{\overline{\rho}}. \quad (2.43)$$

The derived filtered conservation equations for mass and momentum are detailed below:

$$\frac{D\bar{\rho}}{Dt} = -\bar{\rho}\nabla \cdot \tilde{\mathbf{v}}, \quad (2.44)$$

$$\frac{D\tilde{\mathbf{v}}}{Dt} = -\frac{1}{\bar{\rho}}\nabla\bar{P} + \frac{1}{\bar{\rho}}(\nabla \cdot \bar{\rho}\mathbf{v}\nabla)\tilde{\mathbf{v}} + \frac{1}{\bar{\rho}}\nabla \cdot \underline{\tau} + \mathbf{F}, \quad (2.45)$$

where the SPS stress tensor and turbulent eddy viscosity is defined as:

$$\underline{\tau} = \bar{\rho}\left(2\nu_t\underline{S} - \frac{2}{3}\text{tr}[\underline{S}]\underline{I}\right) - \frac{2}{3}\bar{\rho}C_I\bar{\Delta}^2\underline{I} \quad , \quad C_I = 6.6 \times 10^{-4}, \quad (2.46)$$

$$\nu_t = (C_s\Delta x)^2\sqrt{2\langle \underline{S}, \underline{S} \rangle} \quad , \quad C_s = 0.12. \quad (2.47)$$

The authors derived the SPH formulations of the aforementioned governing equations. The continuity equation takes the form as detailed in Eq. 2.2. The pressure gradient term is given in Eq. 2.34. The laminar stress term, consisting of the velocity Laplacian is given by Eq. 2.48, which itself was built on the work of Morris, Fox, and Zhu 1997 as given in Eq. 2.49. Finally the stress divergence is defined by Eq. 2.37.

$$\left(\frac{1}{\rho}(\nabla \cdot \eta \nabla)\mathbf{v}\right)_i = \sum_j m_j \frac{\nu(\rho_i + \rho_j)}{\rho_{ij}^2} \frac{\mathbf{v}_{ij}\mathbf{r}_{ij} \cdot \nabla_i W_{h,ij}}{|\mathbf{r}_{ij}|^2 + \xi^2}, \quad (2.48)$$

$$\left(\frac{1}{\rho}(\nabla \cdot \eta \nabla)\mathbf{v}\right)_i = \sum_j m_j \frac{(\eta_i + \eta_j)\mathbf{v}_{ij}}{\rho_i\rho_j} \left(\frac{1}{|\mathbf{r}_{ij}|} \frac{\partial W_{h,ij}}{\partial r_i}\right) \quad , \quad \nabla_i W_{h,ij} = \frac{\mathbf{r}_{ij}}{|\mathbf{r}_{ij}|} \frac{\partial W_{h,ij}}{\partial r_i}. \quad (2.49)$$

The authors noted that the LES description of viscous effects in slightly compressible SPH could lead to unphysical behaviour at free surfaces due to density variations being magnified by the equation of state. The lack of artificial viscosity implies that such variations are not damped. They subsequently noted that averaging the density would ensure smooth and physically acceptable free surfaces, based on the work of

Panizzo 2004. Hence, they performed Shepard filtering of the density as defined in Eq. 2.50 every 40-time steps.

$$\rho_i = \frac{\sum_j \rho_j W_{h,ij} \mathcal{V}_j}{\sum_j W_{h,ij} \mathcal{V}_j}. \quad (2.50)$$

The authors simulated the problem of a weakly plunging breaker in 2D and 3D to ascertain the performance and capability of the model. Their 2D computational domain consisted of $\approx 1 \times 10^5$ particles, with the 3D domain consisting $\approx 2 \times 10^4$ particles. The authors could show that in the case of the 2D problem, the model could predict regions of high vorticity that persisted longer when compared to standard SPH utilising conventional artificial viscosity. The model also displayed the turbulent bore, which generated reverse breaking, leading to the downbursting-like phenomenon, as observed in experiments (Kubo and Sunamura 2001). In the case of the 3D problem, the authors showed the model's capability to capture near vertically-oriented eddies despite the lower resolution.

Building on this work, R A Dalrymple and B D Rogers 2006 used this scheme on a wide variety of problems, ranging from 2D Green water overtopping, 2D waves on a beach, 3D dam break and 3D waves on a beach. The quantitative analysis of the results allowed the authors to conclude that the model is especially suited for problems involving splash or flow separation. The authors also warn about the model's requirement of a large number of particles for sufficient resolution. That and the finite speed of sound stemming from the compressible flow implied that time steps had to $O(10^{-5}s)$. Hence, the authors remain cautiously optimistic about the model since the method performs well for smaller regions where the number of particles is reasonable. However, they believe that extended Boussinesq codes would more efficiently model larger domains.

2.2.2.2 Modified Smagorinsky Model

Canelas et al. 2016 constructed the wall-adapting local eddy viscosity (WALE) model to be incorporated in the SPH-LES scheme. They noted that studying turbulent flow fields required the identification of vortices themselves to study their interactions in the flow. They used the definition of Lagrangian Coherent Structures (LCS) to help capture these vortices. As a Lagrangian method, SPH is preferable for studying LCS since the technique provides the motion of individual fluid particles, thereby eliminating the need for expensive post-processing inherent to Eulerian solutions. However, they noted that typically employed SPS strategies for LES simulations, based on the standard Smagorinsky model, cannot correctly enforce wall conditions and non-vanishing stresses with laminar flows. Hence they devised the WALE model.

The authors consider the compressible NS along the continuity equation as their governing equation. They subsequently present the SPH formulation of the continuity equation as defined below:

$$\frac{D\rho_i}{Dt} = -\rho_i \sum_j m_j \mathbf{v}_{ij} \cdot \nabla_i W_{h,ij}. \quad (2.51)$$

The pressure gradient term is given in Eq. 2.34. The laminar stress term, consisting of the velocity Laplacian, is given as:

$$(\nu \Delta(\mathbf{v}))_i = \sum_j m_j \frac{4\nu}{\rho_i + \rho_j} \frac{\mathbf{v}_{ij} \mathbf{r}_{ij} \cdot \nabla_i W_{h,ij}}{|\mathbf{r}_{ij}|^2}. \quad (2.52)$$

Finally the stress divergence is defined by Eq. 2.37, with the stress tensor being defined as:

$$\underline{\tau} = \rho \left(2\nu_t \underline{S} - \frac{2\nu_t}{3} \text{tr}[\underline{S}] \underline{I} \right) - \left(\frac{4}{3} \rho C_I (\Delta x)^2 \langle \underline{S}, \underline{S} \rangle \right) \underline{I}, \quad C_I = 6.6 \times 10^{-3}. \quad (2.53)$$

The WALE model redefines the turbulent eddy viscosity as given by:

$$\nu_t = \rho (C_w \Delta x)^2 \frac{\langle \underline{S}^d, \underline{S}^d \rangle^{3/2}}{\langle \underline{S}, \underline{S} \rangle^{5/2} + \langle \underline{S}^d, \underline{S}^d \rangle^{5/4}} \quad , \quad C_w = 0.325, \quad (2.54)$$

$$\underline{S}^d = \frac{1}{2} \left((\nabla \mathbf{v})^2 + ((\nabla \mathbf{v})^T)^2 \right) - \frac{1}{3} \text{tr}[(\nabla \mathbf{v})^2] \underline{I}. \quad (2.55)$$

In order to test their model, the authors considered an array of cylinders in fluid flow as shown in Fig. 2.9, with a constant body force. They computed the vorticity field and the Finite-Time Lyapunov Exponents (FTLE) field to study the LCSs in the flow. These fields are shown in Fig. 2.10 and Fig. 2.11 respectively.

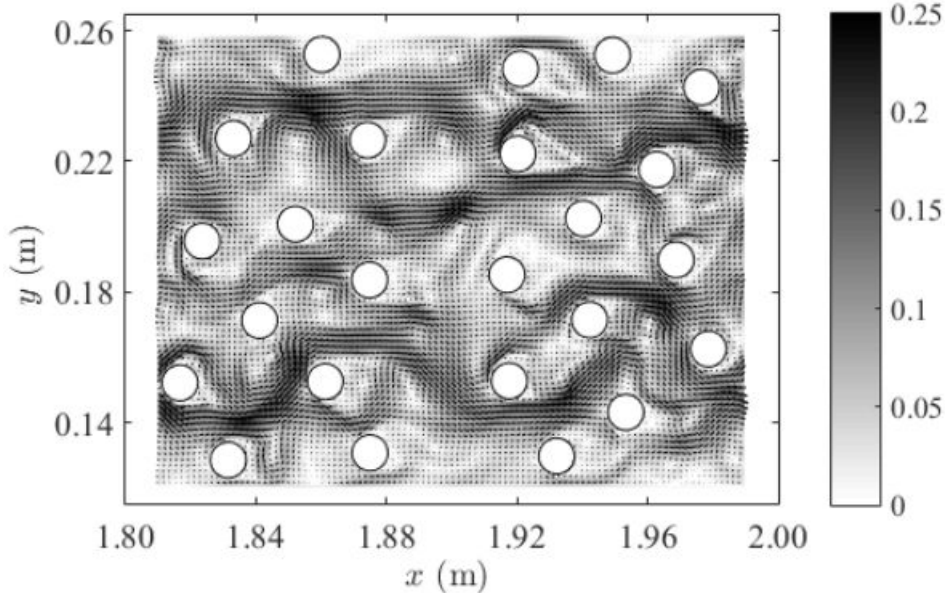


Figure 2.9: Cylinder distribution and instantaneous velocity overlapped by velocity vectors. Velocity in m/s , at $t = 20s$. The flow direction is from left to right. Reproduced from Canelas et al. 2016

The authors observed that the vortices produced, would evolve to recombine into larger structures. However, since vortex stretching is absent in 2D, the authors believe that the recombination signifies *energy injection* which leads to inverse cascade.

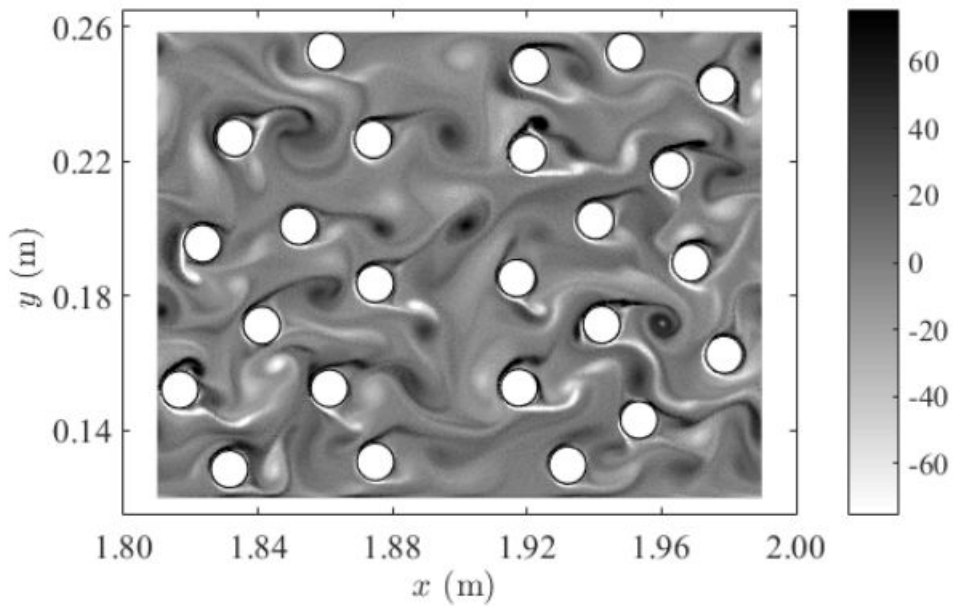


Figure 2.10: Vorticity field. Vorticity in Hz, at $t = 20s$. Reproduced from Canelas et al. 2016

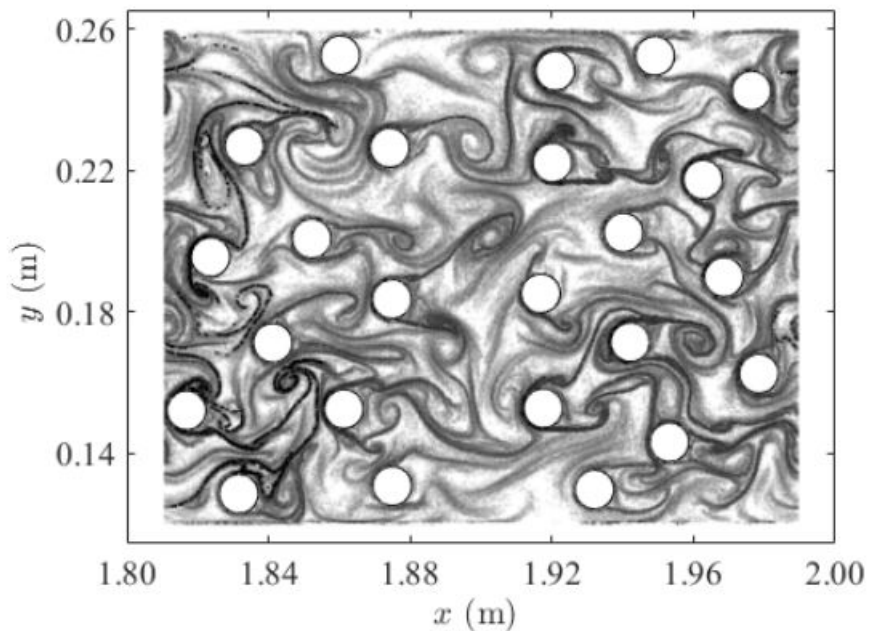


Figure 2.11: FTLE field with negative integration time ($T = -0.4s$) (unstable manifolds - attracting LCS) at $t = 20s$. Reproduced from Canelas et al. 2016

They also observed that vortices with opposing strengths would interact and subsequently lead to vorticity cancellation. Hence, the authors note that such complex interactions lead to difficulties in interpreting the energy spectrum. Therefore, they believe that studies based on coherent structures would be required going forward.

Okrashevski et al. 2022, building on the work of Hardy 1982, show that SPH should be viewed as a Lagrangian quadrature technique for the governing equations of explicit LES, raising interesting implications for SPH as a method itself. Firstly, the kernel scale limits SPH's physical resolution, rendering it unsuitable as a DNS alternative. Secondly, any deficits introduced below the kernel scale could be resolved by consideration of the stress term, from which structures above the kernel scale could benefit. The authors consider this second implication a working hypothesis to try and prove or disprove.

The authors use the compressible NS equations and subject them to a spatial average operator to obtain the filtered governing equations. They subsequently derive the SPH formulations of the mass and momentum conservation equations as given in Eq. 2.15 and Eq. 2.56.

$$\bar{\rho}_i \frac{D\tilde{\mathbf{v}}}{Dt} = - \sum_j (\bar{P}_i + \bar{P}_j) \nabla_i W_{h,ij} \mathcal{V}_j + 2(2 + n_{dim}) \eta \sum_j \frac{\tilde{\mathbf{v}}_{ij} \cdot \mathbf{r}_{ij}}{|\mathbf{r}_{ij}|^2} \nabla_i W_{h,ij} \mathcal{V}_j + \nabla \cdot \underline{\tau}, \quad (2.56)$$

where (n_{dim}) denotes the number of spatial dimensions for a given problem.

The equation of state is given by Eq. 2.57, with the SFS tensor being given by Eq. 2.58.

$$\bar{P}_i = P_o + K \left(\frac{\bar{\rho}_i}{\rho_o} - 1 \right), \quad (2.57)$$

where, (K) is a constant.

$$\underline{\tau} = 2\nu_t \bar{\rho} \underline{S}. \quad (2.58)$$

The SPH formulation for the strain rate tensor is given by Eq. 2.59, and the divergence of the SFS tensor being given by Eq. 2.60.

$$\underline{S}_i = - \sum_j \tilde{\mathbf{v}}_{ij} \otimes \nabla_i W_{h,ij} \mathcal{V}_j, \quad (2.59)$$

$$\left(\nabla \cdot \underline{\tau} \right)_i = \sum_j (\underline{\tau}_i + \underline{\tau}_j) \nabla_i W_{h,ij} \mathcal{V}_j. \quad (2.60)$$

The authors consider three models for the turbulent eddy viscosity:

- SMAG: Standard Smagorinsky model,

$$\nu_t = (C_s \Delta x)^2 \sqrt{2 \langle \underline{S}, \underline{S} \rangle}, \quad (2.61)$$

- SIGMA: σ -model (Nicoud et al. 2011), where (σ_i) denotes the i^{th} singular value of the velocity gradient,

$$\nu_t = (C_\sigma \Delta x)^2 \frac{\sigma_3(\sigma_1 - \sigma_2)(\sigma_2 - \sigma_3)}{\sigma_1^2}, \quad (2.62)$$

- SMAG–MCG: Standard Smagorinsky model discretized in the Monaghan-Cleary-Gingold (MCG) form (Cleary and Joseph J Monaghan 1999),

$$\nabla \cdot \underline{\tau} = 2(2 + n_{dim}) \sum_j \bar{\rho}_i \bar{\rho}_j \frac{\nu_{t,i} + \nu_{t,j}}{\bar{\rho}_i + \bar{\rho}_j} \frac{\tilde{\mathbf{v}}_{ij} \cdot \mathbf{r}_{ij}}{|\mathbf{r}_{ij}|^2} \nabla_i W_{h,ij} \mathcal{V}_j. \quad (2.63)$$

The authors show a correlation between the vorticity and SFS tensor. They subsequently conclude that the fluctuations in the vorticity, energy spectra and SFS tensor are correlated quantities that contain different information about the numerical dissipation dynamics.

The authors use the 3D TGV problem to study and investigate the proposed models. They consider various resolutions to study the problem, varying from $\approx 200^3 - 500^3$ particles.

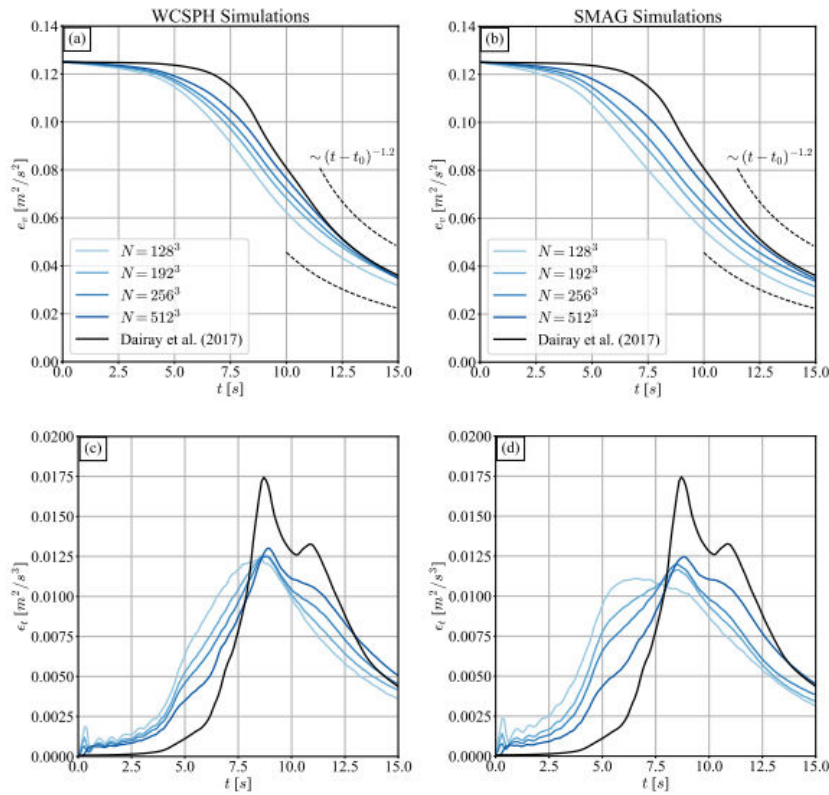


Figure 2.12: Comparison of quantitative metrics for different particle counts N . (a) & (b) Temporal evolution of the density-weighted averaged kinetic energy. (c) & (d) Temporal evolution of the averaged dissipation rate. Reproduced from Okrashevski et al. 2022

The SMAG model degrades the flow in terms of the averaged kinetic energy in Fig. 2.12 (b) and the corresponding dissipation rate in Fig. 2.12 (d). This negative attribute of the model outweighs the positive attribute of the model, in that cases with the SMAG model in Fig. 2.13 (b) appear less tattered and exhibit symmetry compared to the reference WCSPH solution in Fig. 2.13 (a). From Fig. 2.14, it becomes evident that with larger (C_s), the averaged kinetic energy is increasingly reduced, which is also reflected by the dissipation rates. This indicates that the best choice corresponds to ($C_s \rightarrow 0$).

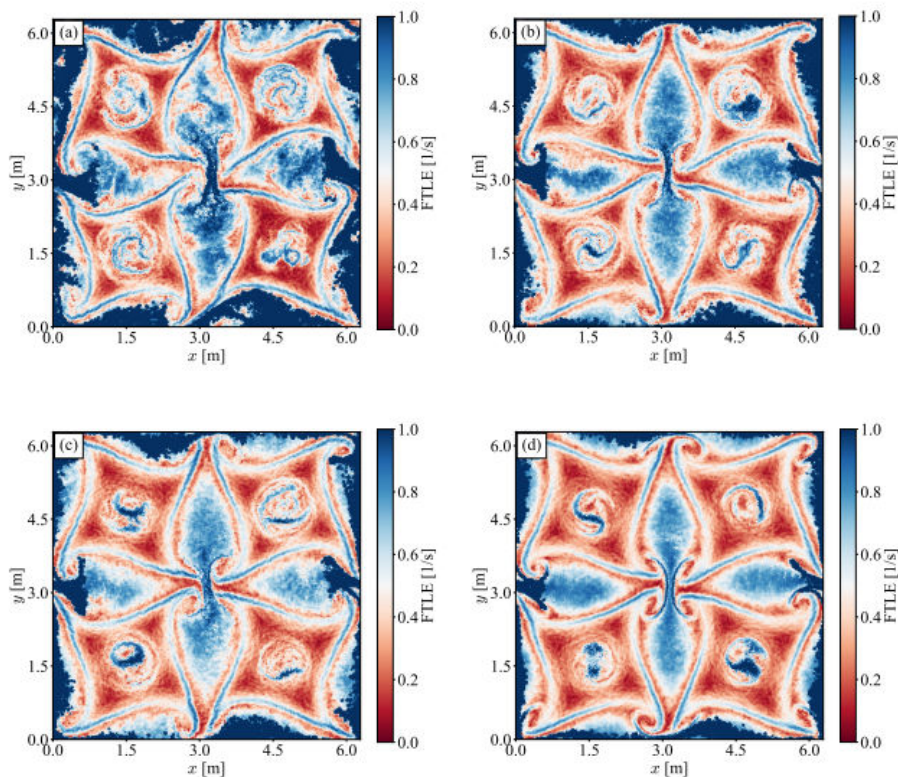


Figure 2.13: Backward FTLE at the plane $z = \pi$ for $N = 2563$ and $t = 14\text{s}$ in the range $[11; 14]\text{s}$. (a) Without explicit SFS model. (b) With the SMAg model. (c) With SIGMA model. (d) With the SMAg-MCG model. Reproduced from Okrashevski et al. 2022

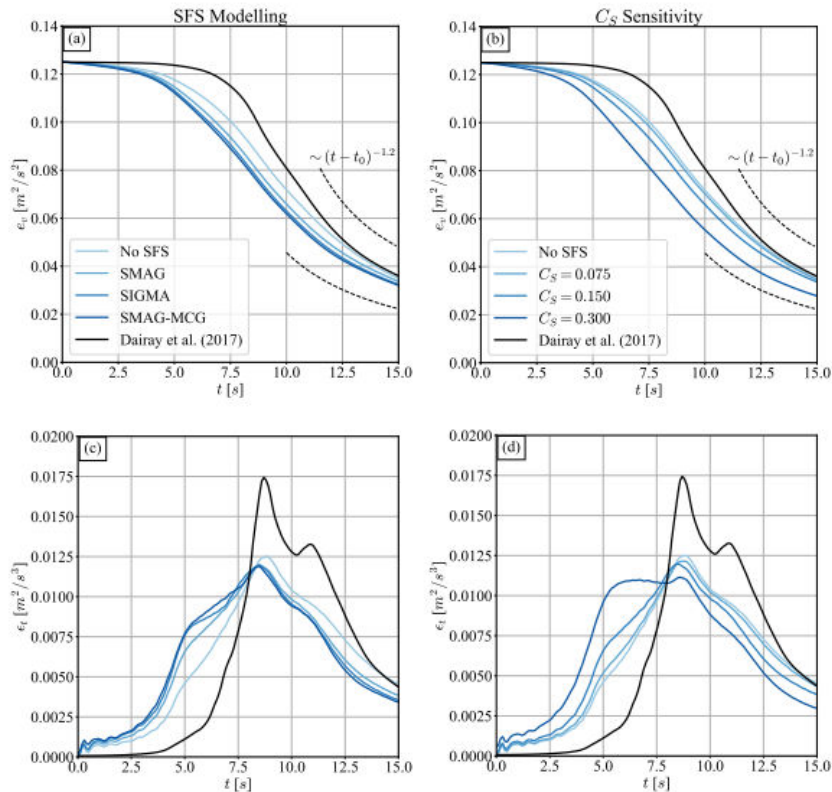


Figure 2.14: Comparison of quantitative metrics for different $N = 256^3$ runs. (a) & (b) Temporal evolution of the density-weighted averaged kinetic energy. (c) & (d) Temporal evolution of the averaged dissipation rate. Reproduced from Okrashevski et al. 2022

On a concluding note, the authors claim that the subsonic turbulence captured by SPH can correctly represent the flow field up to the kernel scale but at a high cost in the best of cases. They also note that explicit SFS models, at most, only lead to marginal improvement of LCS. However, regarding the inertial range dynamics, the dissipative SFS models remove kinetic energy, which is highly detrimental since a spectral energy deficit already characterises SPH. The authors attribute these drawbacks to the non-local character of the Lagrangian quadrature, which they explain through the concept of *Particle Duality*. The concept states that the SPH particles must represent superfluid element approximants and fluid element surrogates simultaneously, leading to an unphysical increase in particle interaction distances. The authors, hence prove Rennehen's expectation that explicit SFS models in an SPH framework can only degrade the quality of the approximation for subsonic turbulent flow (Rennehan 2021), which raises concerns for turbulence modelling in SPH. However, the authors note there might be hope from SPH native models.

2.3 Lagrangian LES-based Models

Having reviewed turbulence models developed for SPH, Di Mascio et al. 2017 concluded that LES models could serve as an excellent middle ground between RANS and DNS. This is because only the sub-grid scale eddies would be modelled, allowing for the larger eddies to be directly simulated from the NS equations. They also note that contemporary SPH-LES models use the Eulerian differential operators in an SPH formulation and therefore do not have a rigorous background. Therefore they propose a Lagrangian form of LES to tie in with the Lagrangian quadrature technique, that is, SPH.

The authors consider a weakly compressible, barotropic fluid whose conservation equations for mass and density are given by Eq. 2.19 and Eq. 2.64 respectively.

$$\frac{D\mathbf{v}}{Dt} = -\frac{1}{\rho} + \nu\Delta(\mathbf{v}) + (\lambda' + \nu)\nabla(\nabla \cdot \mathbf{v}), \quad (2.64)$$

where, $(\lambda' = \lambda/\rho)$ is the Lamé constant. The equation of state is simply given as:

$$P = F(\rho). \quad (2.65)$$

The authors subsequently define a Lagrangian filter (ϕ) with compact support of the form:

$$\phi = \phi(\tilde{\mathbf{r}}_p(t) - \mathbf{y}, t - \tau), \quad (2.66)$$

where the filter is an even function in its arguments, and $(\tilde{\mathbf{r}}_p(t))$ is the position of a material which moves with the velocity being:

$$\tilde{\mathbf{v}}(\tilde{\mathbf{r}}, t) = \int_{\mathbb{R}^3} \int_{-\infty}^{\infty} \phi(\tilde{\mathbf{r}}_p(t) - \mathbf{y}, t - \tau) \mathbf{v}(\mathbf{y}, \tau) d\tau dV_y. \quad (2.67)$$

By using the filter as defined in Eq. 2.66, the filtered governing equations are as follows:

$$\frac{D\tilde{\rho}}{Dt} = -\tilde{\rho}\nabla \cdot \tilde{\mathbf{v}} + \nabla \cdot (\tilde{\rho}\tilde{\mathbf{v}} - \tilde{\rho}\mathbf{v}), \quad (2.68)$$

$$\frac{D\tilde{\mathbf{v}}}{Dt} = -\frac{\nabla \tilde{P}}{\tilde{\rho}} + \nu\Delta(\tilde{\mathbf{v}}) + (\lambda' + \nu)\nabla(\nabla \cdot \tilde{\mathbf{v}}) - \nabla[(\tilde{\rho}) - G(\tilde{\rho})] + \nabla \cdot \underline{T}_l + \widetilde{\mathbf{v}\nabla \cdot \mathbf{v}}, \quad (2.69)$$

$$\frac{D\tilde{\mathbf{r}}}{Dt} = \tilde{\mathbf{v}}, \quad (2.70)$$

$$\tilde{\rho} = F(\tilde{P}), \quad (2.71)$$

$$\underline{\mathbf{T}}_l = \tilde{\mathbf{v}} \otimes \tilde{\mathbf{v}} - \widetilde{\mathbf{v} \otimes \mathbf{v}}, \quad (2.72)$$

$$G(\rho) = \int^{\rho} \frac{1}{s} \frac{dF}{ds} ds, \quad (2.73)$$

In order for the authors to be able to reinterpret the Lagrangian LES through SPH, they split the filter as follows:

$$\phi(\tilde{\mathbf{r}}_p(t) - \mathbf{y}, t - \tau) = W(\tilde{\mathbf{r}} - \mathbf{y})\theta(t - \tau). \quad (2.74)$$

This allows the author to provide a relationship between the various type of filtered quantities as given here below:

$$\langle f \rangle(\tilde{\mathbf{r}}, t) = \int_{\mathbb{R}^3} W(\tilde{\mathbf{r}} - \mathbf{y})f(\mathbf{y}, t)dV_y, \quad (2.75)$$

$$\bar{f}(\mathbf{y}, t) = \int_{\mathbb{R}} \theta(t - \tau)f(\mathbf{y}, \tau)d\tau, \quad (2.76)$$

$$\tilde{f} = \langle \bar{f} \rangle, \langle \bar{f} \rangle \neq \langle \bar{f} \rangle, \quad (2.77)$$

The authors, therefore, can derive the equations in an SPH formalism as given by:

$$\frac{D\tilde{\rho}}{Dt} = -\tilde{\rho}\langle \nabla \cdot \tilde{\mathbf{v}} \rangle + C_1 + C_2, \quad (2.78)$$

$$C_1 = -\tilde{\rho}\langle \nabla \cdot (\bar{\mathbf{v}} - \tilde{\mathbf{v}}) \rangle, \quad (2.79)$$

$$C_2 = \nabla \cdot (\tilde{\rho}\tilde{\mathbf{v}} - \rho\mathbf{v}), \quad (2.80)$$

$$\frac{D\tilde{\mathbf{v}}}{Dt} = -\frac{\langle \nabla \tilde{P} \rangle}{\tilde{\rho}} + \nu\langle \Delta(\tilde{\mathbf{v}}) \rangle + (\lambda' + \nu)\langle \nabla(\nabla \cdot \tilde{\mathbf{v}}) \rangle + M_1 + M_2, \quad (2.81)$$

$$M_1 = -\frac{\langle \nabla(\bar{\rho} - \tilde{\rho}) \rangle}{\tilde{\rho}} + \nu\langle \Delta(\bar{\mathbf{v}} - \tilde{\mathbf{v}}) \rangle + (\lambda' + \nu)\langle \nabla(\nabla \cdot (\bar{\mathbf{v}} - \tilde{\mathbf{v}})) \rangle, \quad (2.82)$$

$$M_2 = -\nabla\left(\widetilde{G(\rho)} - G(\tilde{\rho})\right) + \widetilde{\mathbf{v}\nabla \cdot \mathbf{v}} + \nabla \cdot \underline{\mathbf{T}}_l, \quad (2.83)$$

$$\frac{D\tilde{\mathbf{r}}}{Dt} = \tilde{\mathbf{v}}, \quad (2.84)$$

$$\tilde{P} = F(\tilde{\rho}). \quad (2.85)$$

The authors close the terms (C_2, M_2) as follows:

$$C_2 \approx \nabla \cdot (\nu_\delta \nabla \tilde{\rho}), \quad (2.86)$$

$$\nu_\delta = (C_\delta \sigma)^2 \sqrt{2\langle \underline{\mathbf{S}}, \underline{\mathbf{S}} \rangle}, \quad (2.87)$$

where (ν_δ) has the dimensions of kinematic viscosity and represents a turbulent diffusion coefficient, (C_δ) represents a dimensionless coefficient, and ($\sigma \propto h$). If the

spatial derivative of (ν_δ) is negligible then:

$$C_2 = \nu_\delta \Delta(\tilde{\rho}), \quad (2.88)$$

$$M_2 = \nabla \cdot \underline{T}_l = \nabla \cdot \left(-\frac{k^2}{3} \underline{I} - \frac{2}{3} \nu_t \text{Tr}[\tilde{\underline{S}}] \underline{I} + 2\nu_t \tilde{\underline{S}} \right), \quad (2.89)$$

$$k^2 = 4C_y \sigma^2 \langle \underline{S}, \underline{S} \rangle, \quad C_y = 0.044, \quad (2.90)$$

$$\nu_t = (C_s \sigma)^2 \sqrt{2 \langle \underline{S}, \underline{S} \rangle}, \quad C_s = 0.12, \quad (2.91)$$

where ($\text{Tr}[]$) is the trace operator, (C_y) is the Yoshizawa constant (Yoshizawa 1986), and (C_s is the Smagorinsky constant.

The above equations, coupled with the closure models, allow the authors to replace the differential operators with SPH counterparts of WCSPh.

The authors used the 2D and 3D TGV problems to validate the model. The authors considered Reynolds number up to $\approx 1.2 \times 10^5$ for the 2D case, and $\approx 1.5 \times 10^3$ for the 3D case. The authors also compared the proposed model against that of the DNS SPH scheme, which was developed by Mayrhofer et al. 2015 as observed in Fig. 2.15 and Fig. 2.16.

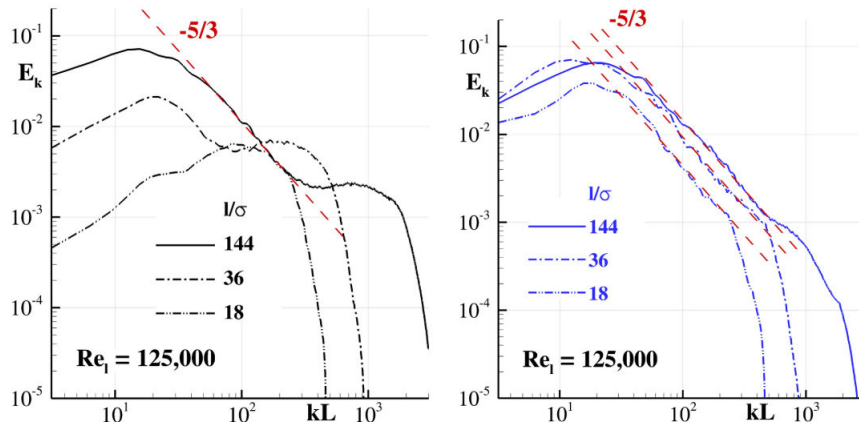


Figure 2.15: 2D freely decaying turbulence ($tU/L = 2, Re = 1.25 \times 10^5$). Left: Energy spectrum using DNS-SPH. Right: Energy spectrum using LES-SPH. Reproduced from Di Mascio et al. 2017

As seen from the results of the simulations in Fig. 2.15 and Fig. 2.16 for the 2D and 3D case, respectively, the authors were able to claim that the model captures the typical characteristics of the flow evolution with relatively coarse particle discretisation, provided an appropriate LES modelling is used.

Building on this, Antuono et al. 2021 introduced a small arbitrary velocity deviation ($\delta\tilde{\mathbf{v}}$) to the fluid particle as given by:

$$\frac{D\tilde{\mathbf{r}}}{Dt} = \tilde{\mathbf{v}} + \delta\tilde{\mathbf{v}}. \quad (2.92)$$

This was done since the Lagrangian nature of the proposed model was proving to be an obstacle for accurate simulations of high Reynolds number problems. Therefore, they modified the model with the transport equation given in Eq. 2.92 to obtain

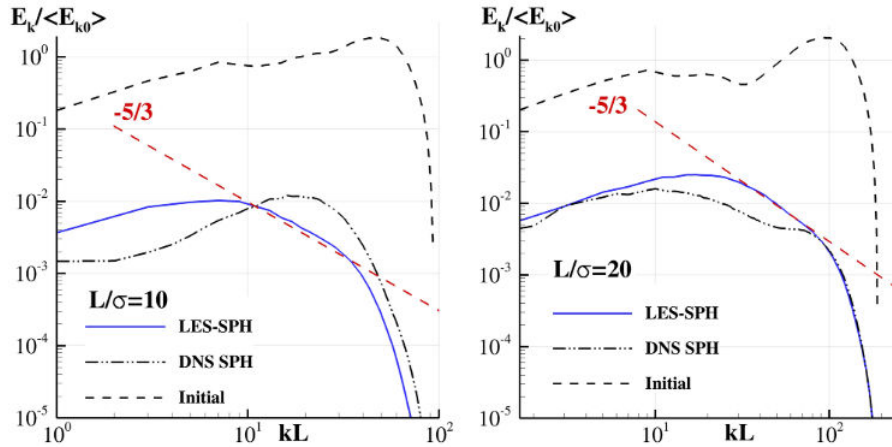


Figure 2.16: 3D homogeneous turbulence decay. Comparison between DNS-SPH and LES-SPH simulations ($tU/L = 5$). Left: Particle resolution = 64^3 . Right: particle resolution = 128^3 . Reproduced from Di Mascio et al. 2017

a quasi-Lagrangian LES-SPH model. The small velocity deviation to the actual Lagrangian velocity was based on the work done on particle shifting technique (PST) and tensile instability control (TIC) technique by Sun, Andrea Colagrossi, et al. 2018 in their δ -SPH scheme.

The authors subsequently employed this δ -LES-SPH scheme with the same set of closure models as detailed by Di Mascio et al. 2017. They compared their proposed model with standard LES-SPH on the 2D and 3D TGV problems for Reynolds numbers up to 1×10^6 .

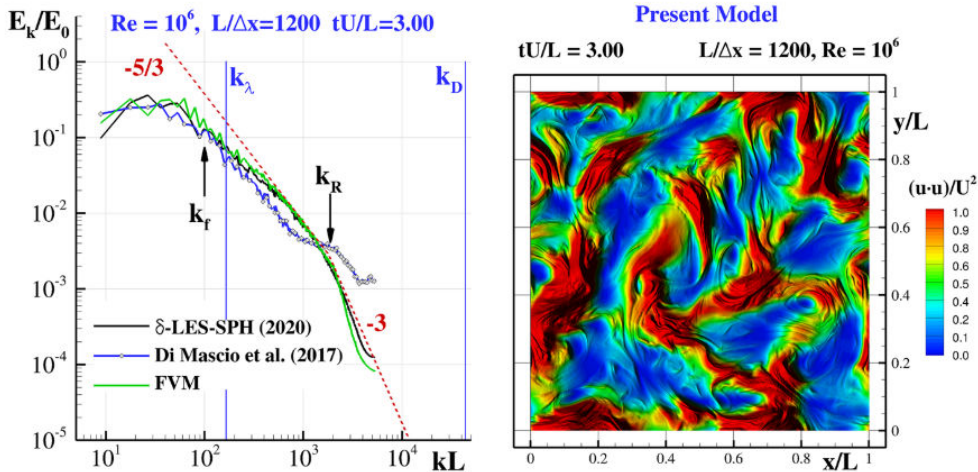


Figure 2.17: Left: Energy spectrum at ($tU/L = 3, Re = 1 \times 10^6$) as predicted by the δ -LES-SPH model and a finite volume scheme. Symbols k_f and k_R indicate the wave numbers of the external forcing and the kernel radius, respectively, while k_λ and k_D are the wave numbers associated with the Taylor and Kolmogorov scales. Right: k field at the same instant. Reproduced from Antuono et al. 2021

As seen from the results of the simulations in Fig. 2.17 and Fig. 2.18 for the 2D

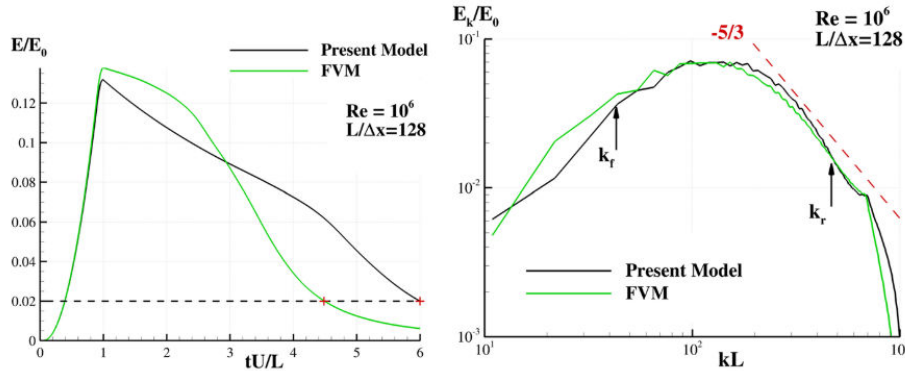


Figure 2.18: Left: Time histories of k as predicted by finite volume scheme and the δ -LES-SPH model. Right: Energy spectra. Symbols k_f and k_R denote the wave numbers of the external forcing and the kernel radius, respectively. Reproduced from Antuono et al. 2021

and 3D case respectively, the authors claimed that the proposed model could overcome issues of high Reynolds number flows, such as generation of spurious high-frequency noise and the onset of the tensile instability. Furthermore, comparing the proposed model's and an FVM solve's energy spectra with the theoretical decay rate confirmed the model's accuracy and reliability.

The authors conclude that the δ -LES-SPH model would need to be validated for flows with a Reynolds number larger than 1×10^6 with experimental or numerical data. They believe that the inclusion of wall functions to deal with solid boundaries and the extension of the model to free-surface flows can further improve the model's effectiveness. Finally, the authors believe that a higher-order approach could significantly improve the model results.

2.3.1 Extension to EDAC-SPH Scheme

The Entropically Damped Artificial Compressibility (EDAC) SPH scheme, based on the work of Clausen 2013, is an explicit SPH method devised for incompressible flow by Prabhu Ramachandran and Puri 2019. In this scheme, the authors consider a transport equation for pressure instead of density derived from the continuity equation, as given below:

$$\frac{DP}{Dt} = -c_s^2 \rho \nabla \cdot \mathbf{v} + \nu \nabla^2 P. \quad (2.93)$$

Considering the pressure evolution equation above, an equation of state is longer required by the scheme. By filtering Eq. 2.93 with the Lagrangian LES technique (Di Mascio et al. 2017), we arrive at the result given by Eq. 2.94 (Refer Appendix A for derivation).

$$\frac{D\tilde{P}}{Dt} = -c_s^2 \rho \nabla \cdot \tilde{\mathbf{v}} + \nu \nabla^2 \tilde{P} + \tilde{\mathbf{v}} \cdot \nabla \tilde{P} - \widetilde{\mathbf{v} \cdot \nabla P}. \quad (2.94)$$

In Eq. 2.94, we see that the term $(\widetilde{\mathbf{v} \cdot \nabla P})$ cannot be reduced further to a form of $(f(\tilde{\mathbf{v}}, \tilde{P}))$. Hence, we cannot proceed with the SPH formulation for the pressure equation, implying that the EDAC scheme might not be compatible with the Lagrangian LES model.

2.4 RANS-based $k - \epsilon$ Models

Songdong Shao 2006 demonstrated that the two-equation $k - \epsilon$ model, an extensively studied model derived from the Reynolds-averaged Navier-Stokes (RANS) equations, can be incorporated in the truly incompressible version of SPH (ISPH). By attempting to extend RANS equations, which are hugely successful in practical fields, to a mesh-free method such as SPH, the author provides a framework to build on the wide variety of closure models available.

To discretise the RANS equations to an SPH form, the author considers the Reynolds averaged mass and momentum conservation equations as given in Eq. 2.95 and Eq. 2.96 respectively. Note: The averaged flow properties are represented without any over-line (...) hereafter.

$$\frac{1}{\rho} \frac{D\rho}{Dt} + \nabla \cdot \mathbf{v} = 0 \quad , \quad \frac{D\rho}{Dt} = 0 \text{ (Incompressible)}, \quad (2.95)$$

$$\frac{D\mathbf{v}}{Dt} = -\frac{1}{\rho} \nabla P + \nu \Delta(\mathbf{v}) + \frac{1}{\rho} \nabla \cdot \underline{\tau} + \mathbf{F}. \quad (2.96)$$

The stress tensor is given by Eq. 2.23, while the turbulent eddy viscosity is defined below:

$$\nu_t = c_d \frac{k^2}{\epsilon}. \quad (2.97)$$

The transport equations for the turbulent kinetic energy and dissipation rate is given by Eq. 2.98 and Eq. 2.99 respectively.

$$\frac{Dk}{Dt} = \nabla \cdot \left(\frac{\nu_t}{\sigma_k} \nabla k \right) + P_k - \epsilon, \quad (2.98)$$

$$\frac{D\epsilon}{Dt} = \nabla \cdot \left(\frac{\nu_t}{\sigma_\epsilon} \nabla \epsilon \right) + c_{1\epsilon} \frac{\epsilon}{k} P_k - c_{2\epsilon} \frac{\epsilon^2}{k}, \quad (2.99)$$

$$P_k = 2\nu_t \langle \underline{\mathbf{S}}, \underline{\mathbf{S}} \rangle, \quad (2.100)$$

where, $(\sigma_k, \sigma_\epsilon, c_{1\epsilon}, c_{2\epsilon}) = (1.0, 1.3, 1.44, 1.92)$ are empirical constants dependent on the nature of the flow, and (P_k) is the turbulence production rate, which satisfies the relation given by Eq. 2.101 (Stephen B Pope and Stephen B Pope 2000).

$$\frac{P_k}{\epsilon} = c_d \left(\frac{\sqrt{2\langle \underline{\mathbf{S}}, \underline{\mathbf{S}} \rangle}}{\epsilon} \right). \quad (2.101)$$

These governing equations are solved and evolved using the same predictive-corrective time integrator as seen in the work of Hitoshi Gotoh, Songdong Shao, and Memita 2004, and outlined in Eq. 2.26 - Eq. 2.32.

As for the SPH formulations of the governing equations, the author builds on the work of Hitoshi Gotoh, Songdong Shao, and Memita 2004, and uses the same discretization as defined in Eq. 2.33 - Eq. 2.37. However, the author uses a slightly modified version of the laminar stress term given in Eq. 2.38 and redefines it as

given below:

$$(\nu \Delta(\mathbf{v}))_i = \sum_j m_j \frac{2(v_i + v_j)}{\rho_i + \rho_j} \frac{\mathbf{v}_{ij} \mathbf{r}_{ij} \cdot \nabla_i W_{h,ij}}{|\mathbf{r}_{ij}|^2}. \quad (2.102)$$

The author tested the model on the problem of 2D wave breaking and overtopping of a sloping wall and compared the results obtained against the experimental data from the work of T. Li, Troch, and De Rouck 2004 to validate the model—the computational domain of $\approx 6 \times 10^3$ particles.

As seen from the evolution of the water surface elevation plotted in Fig. 2.19, the author could ascertain that the proposed model produced better results than those of T. Li, Troch, and De Rouck 2004, compared to the experimental data in Fig. 2.19(a) and Fig. 2.19(b). This could be attributed to the free surfaces being accurately tracked by particles without numerical diffusion. In Fig. 2.19(c) and Fig. 2.19(d), despite the wave profiles being consistent with each other in phase and shape, the proposed model predicts smaller elevation levels. Li et al. use a dynamic Smagorinsky model, whereas the proposed model uses constant empirical coefficients. The author believes these coefficients derived from a quasi-steady state may behave sub-optimally in transient flow, such as the problem at hand.

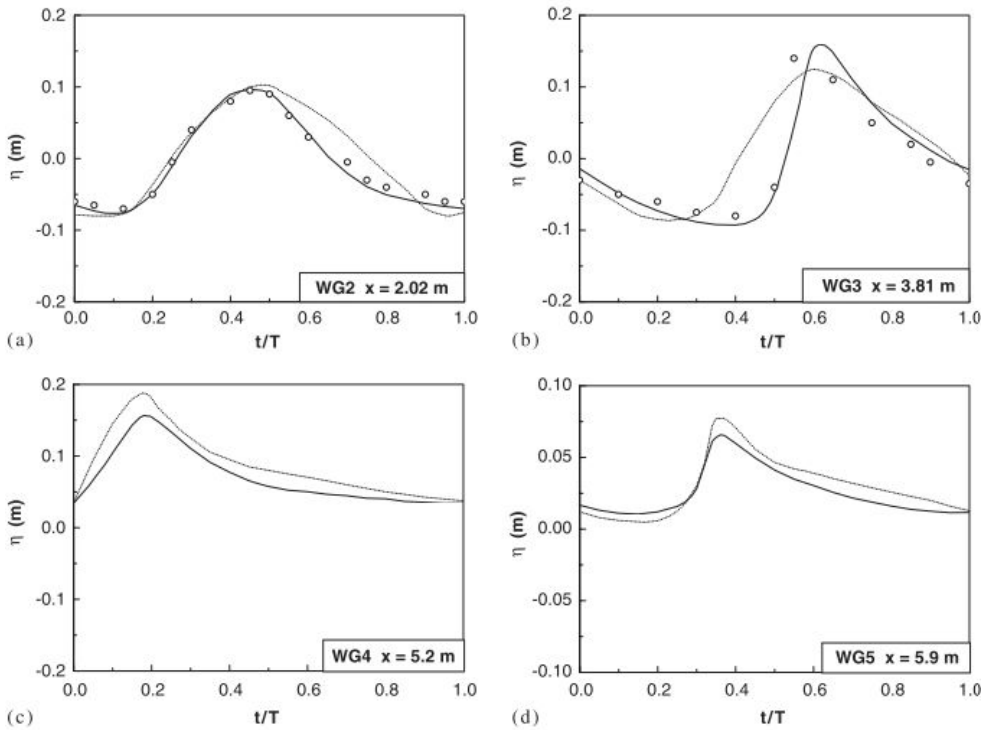


Figure 2.19: Comparisons of computed water surface elevations by SPH (solid lines) with experimental (○) and numerical (dotted lines) data of T. Li, Troch, and De Rouck 2004. Reproduced from Songdong Shao 2006

The author concludes that the $k - \epsilon$ model would require further sensitivity analysis for the turbulence model and spatial resolution for improved results, despite being reasonably accurate in tracking free surfaces.

Wang and P. L. Liu 2020 build on the work of Songdong Shao 2006 to further improve the ISPH $k - \epsilon$ model. They achieved this by using the modelling and computational developments which SPH has benefited from since the work of Shao. The authors here consider the same SPH discretised equations and two-step time integrator as Shao, with two distinct modifications in the Pressure Poisson equation as given by Eq. 2.103 instead of Eq. 2.30. They also redefined propagation equation for (\mathbf{r}) using Eq. 2.104 instead of Eq. 2.32.

$$\nabla \cdot \left(\frac{1}{\rho_o} \nabla P_{t+1} \right) = \frac{1}{\Delta t} \nabla \cdot \mathbf{u}_*, \quad (2.103)$$

$$\mathbf{r}_{t+1} = \mathbf{r}_* + \Delta \mathbf{v}_{**} \Delta t. \quad (2.104)$$

The authors also provided SPH discretization for the transport equations for (k) and (ϵ) using Eq. 2.106 and Eq. 2.107 which requires the use of particle density (φ) as given in Eq. 2.105.

$$\varphi_i = \sum_j W_{h,ij}, \quad (2.105)$$

$$\nabla \cdot \left(\frac{\nu_t}{\sigma_k} \nabla k \right)_i = - \sum_j \frac{1}{\varphi_j} \left(\frac{\nu_{t,i}}{\sigma_k} + \frac{\nu_{t,i}}{\sigma_k} \right) \frac{k_{ij} \mathbf{r}_{ij} \nabla_i W_{h,ij}}{|\mathbf{r}_{ij}|^2}, \quad (2.106)$$

$$\nabla \cdot \left(\frac{\nu_t}{\sigma_\epsilon} \nabla \epsilon \right)_i = - \sum_j \frac{1}{\varphi_j} \left(\frac{\nu_{t,i}}{\sigma_\epsilon} + \frac{\nu_{t,i}}{\sigma_\epsilon} \right) \frac{\epsilon_{ij} \mathbf{r}_{ij} \nabla_i W_{h,ij}}{|\mathbf{r}_{ij}|^2}. \quad (2.107)$$

The authors also derived an SPH formulation for the strain rate tensor defined in Eq. 2.108, which is based on the studies done on kernel correction (Bonet and Lok 1999; Khayyer, Gotoh, and SD Shao 2008) and given by Eq. 2.109 and Eq. 2.110.

$$\underline{S}_i = \frac{1}{2} \left(\nabla \mathbf{v}_i + (\nabla \mathbf{v}_i)^T \right), \quad (2.108)$$

$$\nabla \mathbf{v}_i = - \sum_j \frac{1}{\varphi_j} \mathbf{v}_{ij} \otimes \underline{\mathbf{L}}_i \nabla_i W_{h,ij}, \quad (2.109)$$

$$\underline{\mathbf{L}}_i = \left(- \sum_j \frac{1}{\varphi_j} \nabla_i W_{h,ij} \otimes \mathbf{r}_{ij} \right)^{-1}. \quad (2.110)$$

The authors validated the model against the problem of a solitary wave propagating over a bottom-mounted barrier in 2D. Its results are shown in Fig. 2.20. They also considered the problem involving wave breaking on a slopping wall in 2D, which is shown in Fig. 2.21.

Given the model's accuracy, as observed from the figures, the authors conclude that the model's capabilities have been demonstrated, especially in tracking transient-free surfaces. They also reproduce the evolution of turbulence and its intensity due to flow separation. However, they note that the model under-predicts the max turbulent kinetic energy and is sensitive to the initial seeding of the turbulent kinetic energy property. The authors also state that the counteracting effects of the physical viscous dissipation and numerical dissipation, dependent on the particle resolution, would have to be appropriately balanced. Finally, the authors conclude on the

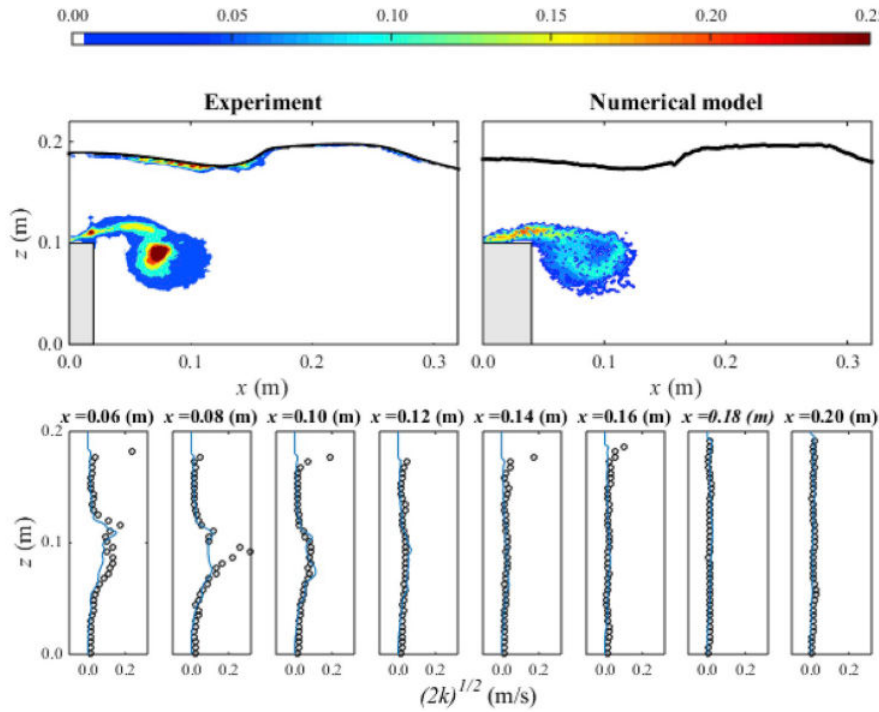


Figure 2.20: Comparisons between experimental data (left) and numerical results (right) for turbulence intensity (m/s) at $t = 0.6s$ (top panels) and the corresponding vertical cross-sections (lower panels). In the lower panels, solid lines and \circ represent the numerical and experimental results, respectively. Reproduced from Wang and P. L. Liu 2020

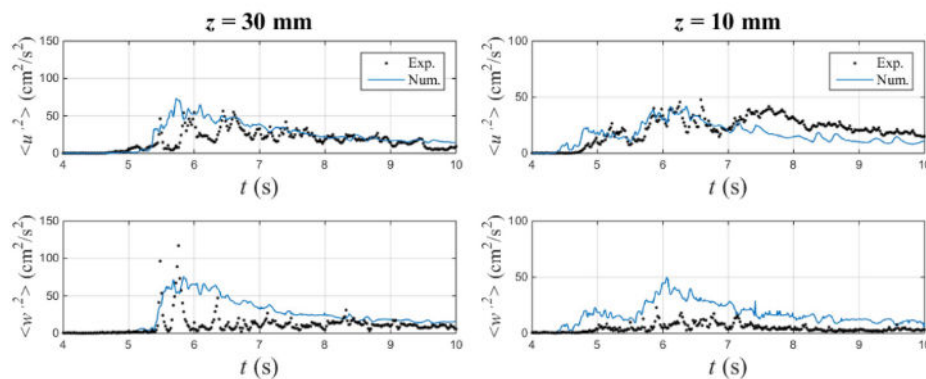


Figure 2.21: Comparisons of numerical and experimental turbulent kinetic energy in x-direction and y-direction. Reproduced from Wang and P. L. Liu 2020

importance of boundary treatment and the need for more sophisticated boundary models to extend the model to 3D domains.

2.5 LANS-based Models

So far, having dealt with RANS and LES models of turbulence, a few fundamental drawbacks of these techniques have been brought to light. In the case of RANS, the flow field is decomposed into an averaged mean flow and a fluctuating field. Such a decomposition of the NS equations provides differential equations for the mean flow containing contributions from the time-varying turbulent motion. Therefore a closure model is required to capture the effects of the fluctuations on the mean flow. However, by studying only the mean flow quantities, the complete nature of the flow, notwithstanding the complex structures stemming from these fluctuations, cannot be studied, let alone appreciated.

On the face of it, LES would have made for a reasonable alternative to model turbulent flows. This is because the large scales in the flow are resolved by the standard NS equations, while the effects of smaller scales are modelled. However, this remains easier said than done since inhomogeneous and wall-bounded flows necessitate the LES filter width to vary dynamically to capture the average size of turbulent eddies.

The other widespread method of tackling turbulence involves Direct Numerical Simulation (DNS). However, since the number of degrees of freedom for a 3D flow grows rapidly with the Reynolds number ($\propto Re^{9/4}$), this technique effectively places an inviolable upper bound on the Re for a given simulation because of computational limitations.

In order to tackle the issues above and address them reasonably, we look for possible solutions. One such solution is the Lagrangian averaging method introduced by Holm, Jerrold E Marsden, and Ratiu 1998 and J. E. Marsden and Shkoller 2001. In this method, unlike the averaging or filtering of the NS equations as done in RANS or LES, the Lagrangian averaging approach averages at the level of the variational principle from which the Navier–Stokes equations are derived. This procedure yields the Lagrangian-averaged Navier Stokes- α (LANS- α) equations, which describe the time evolution of large eddies in turbulent flows. It can be stated that this approach is similar to that of LES.

The LANS- α equations, assuming incompressibility and isotropic turbulence, are derived and simplified by Mohseni et al. 2003. These equations are as follows:

$$\nabla \cdot \mathbf{v} = 0, \quad (2.111)$$

$$\frac{D\mathbf{v}}{Dt} = \underline{\sigma}(\mathbf{v}), \quad (2.112)$$

$$\underline{\sigma}(\mathbf{v}) = -P\mathbf{I} + 2\nu(1 - \alpha^2\Delta)\underline{\mathcal{S}} + 2\alpha^2\underline{\dot{\mathcal{S}}}, \quad (2.113)$$

$$\underline{\dot{\mathcal{S}}} = \frac{D\underline{\mathcal{S}}}{Dt} + \underline{\mathcal{S}\mathcal{R}} - \underline{\mathcal{R}\mathcal{S}}, \quad (2.114)$$

$$\underline{\mathcal{R}} = \frac{1}{2} \left(\nabla \mathbf{v} - (\nabla \mathbf{v})^T \right), \quad (2.115)$$

where α denotes the scale of rapid fluctuations in the flow map, such that for scales smaller than α , the wave activity is filtered by a nonlinear energy redistribution. Here, $(1 - \alpha^2 \Delta)$ denotes the Helmholtz operator.

J. J. Monaghan 2002, building on the work of Holm, Jerrold E Marsden, and Ratiu 1998, attempted to formulate an SPH version of the continuum LANS- α equations. His work provided one of the earliest models of turbulence in compressible flow. The author incorporated some of his earlier work on XSPH (J. Monaghan 1989), in which particles are moved with a smoothed velocity, leaving the acceleration equation unchanged. The smoothed velocity denoted an average over the velocities of the neighbouring particles. This facilitated the author in writing the Lagrangian analysed by Holm in an SPH form, allowing for the subsequent derivation of the momentum equation, albeit being elaborate and highly complicated. Nevertheless, in conjunction with the continuity equation, the derived momentum equation formulated the SPH- α model, which essentially consisted of an SPH particle moving with the transport velocity smoothed from momentum velocity by an iterative algorithm with an additional dissipation term meant to mimic the standard LES model.

X. Y. Hu and N. A. Adams 2015 also devised a turbulence model for incompressible flow based on spatial filtering of the NS equations using SPH approximations termed the SPH- σ model. The model shares similarities with the LANS- α model and the SPH- α model, differing by the additional stress term in the model and its approach in evaluating the particle transport velocity. The proposed model is also built on the authors' previous work (X. Hu and Nikolaus A Adams 2007), and hence shares similar numerical techniques. The authors also validated the proposed model on 2D flow comprising decaying and forced turbulence cases. Their results suggested that the model could simulate incompressible turbulent flow.

Monaghan (J. J. Monaghan 2011, 2017) subsequently improved on the SPH- α model and derived a more amenable variant of the momentum equation. Since, in this case, the model was parameterised around the smoothing parameter (ε), the turbulence model was termed the SPH- ε model. The linearly smoothed velocity ($\hat{\mathbf{v}}$) is given below:

$$\hat{\mathbf{v}}_i = \mathbf{v}_i - \varepsilon \sum_j \frac{m_j}{M_o} \mathbf{v}_{ij} K_{h',ij} \quad , \quad \varepsilon \in [0, 1], \quad (2.116)$$

where (K) is a smoothing kernel, which can be different from the kernel used in SPH, its corresponding smoothing length being (h'). It is noted that the smoothed velocity preserves the shape of the spectrum of the unsmoothed velocity for short-length scales. However, it reduces the magnitude of the unsmoothed velocity by a factor $(1 - \varepsilon)$.

The equation of state is given by Eq. 2.1, and the momentum equation is given by Eq. 2.117. The momentum equation's third term on the right-hand side is an extra stress term determined by the smoothing. Its overall effect is to redistribute energy without dissipation.

$$\frac{D \mathbf{v}_i}{D t} = - \sum_j m_j \left(\frac{P_i}{\rho_i^2} + \frac{P_j}{\rho_j^2} \right) \nabla_i W_{h,ij} - \sum_j m_j \Pi_{ij} \nabla_i W_{h,ij} + \frac{\varepsilon}{2} \sum_j \frac{m_j}{M_o} |\mathbf{v}_{ij}| \nabla_i W_{h,ij}, \quad (2.117)$$

where the viscosity term (Π_{ij}) is given by Eq. 2.118, in which (α) is a constant.

$$\Pi_{ij} = -\frac{2\alpha c_s \mathbf{v}_{ij} \cdot \mathbf{r}_{ij}}{(\rho_i + \rho_j) |\mathbf{r}_{ij}|^2}. \quad (2.118)$$

The particles are subsequently transported as given below:

$$\frac{D \mathbf{r}_i}{D t} = \hat{\mathbf{v}}_i. \quad (2.119)$$

The author validated the proposed model by simulating 2D flow past a cylinder moving along a Lissajous curve. The author demonstrated the model's capabilities to predict satisfactory results for the velocity correlation functions, energy spectrum and mixing while having particle resolution be half of that required for a DNS with a resolution the Reynolds length. The author concludes that the model's effectiveness for higher Reynolds numbers and other boundary conditions, such as free surfaces, will need to be studied further.

2.6 Miscellaneous Models

S. Liu et al. 2019 approached the problem of turbulence modelling from the perspective of computer 3D visualisation to visualise flows with realistic features. The authors' viscosity-based vorticity correction model offers more advantages to the computer visual-effects audience. However, the model would still be a worthwhile investigation.

The authors define a vorticity field ($\boldsymbol{\omega}$) in the system as given below:

$$\boldsymbol{\omega}_i = \nabla \times \mathbf{v}_i = -\frac{1}{\rho} \sum_j m_j \mathbf{v}_{ij} \times \nabla_i W_{h,ij}. \quad (2.120)$$

The contribution to the SPH particle's momentum velocity from the viscous term is calculated as given by:

$$\mathbf{v}_{v,i} = \mathbf{v}_i + \mathbf{a}_i^{(visc)} \Delta t. \quad (2.121)$$

If the magnitude of viscous velocity ($\mathbf{v}_{v,i}$) is greater than (\mathbf{v}_i) for a given particle, then its vorticity field is updated as given by:

$$\delta \boldsymbol{\omega}_i = (\alpha \sqrt{R_i}) \boldsymbol{\omega}_i, \quad (2.122)$$

$$R_i = \frac{\delta E_i}{E_i} = \frac{\mathbf{v}_{v,i}^2 - \mathbf{v}_i^2}{\mathbf{v}_i^2}. \quad (2.123)$$

A stream function (Ψ) is subsequently defined as given by:

$$\Psi_i = \sum_j \frac{\delta \boldsymbol{\omega}_j \mathcal{V}_j}{4\pi |\mathbf{r}_{ij}|}. \quad (2.124)$$

The velocity correction ($\delta \mathbf{v}$) for the particle is subsequently defined by:

$$\delta \mathbf{v}_i = \nabla \times \Psi_i. \quad (2.125)$$

Obeidat and Bordas 2018, tackle the problem of turbulence by devising a hybrid remeshed method (hrSPH) for the simulation of three-dimensional turbulent flows. The authors essentially use an Eulerian mesh with Lagrangian particles to gain advantages of both schemes. The governing equations are evaluated using the properties at the mesh nodes, which are interpolated from the particles. After evaluating the system of equations, the new properties on the mesh nodes are used to update the properties of the particles through mesh-to-particle interpolation. The authors consider the turbulent sub-grid stresses using the Smagorinsky model.

The proposed model remeshes the particles when the distribution is not uniform. The authors validated the model against the 2D and 3D TGV problems, thin double shear layer problems, and 3D isotropic turbulence obtained from DNS. The model predicts the energy spectra and energy dissipation reasonably well. Despite the model's accuracy, not much information can be gathered to help solely improve the state of turbulence modelling in SPH.

3 Evaluation of Turbulence Models

Turbulence, as a phenomenon, has been notoriously difficult for a detailed physical analysis. This is further exacerbated by the seemingly endless complex interactions it gives rise to in the flow as long as any form of energy is provided. Therefore, while modelling turbulence remains one facet of the problem, visualising and analysing the model is another equally challenging task.

As seen in the previous [Chapter 2](#), numerous Lagrangian turbulent models seem to be tested for only complex surface flows. However, a systematic analysis of isotropic turbulence problems provides greater insight into the energy spectrum and its corresponding cascade across varying length scales. A reasonable model should be able to capture the characteristic hierarchy of scales through which the energy cascade takes place. The dissipation of kinetic energy finally occurs at the scales of the order of Kolmogorov length, where the flow subsequently becomes laminar. In contrast, the injection of energy in turbulent flow generally occurs at much larger scales.

Hence, appropriate test cases must be used when analysing turbulence.

3.1 Benchmark Problems

3.1.1 Taylor-Green Vortex Problem

The Taylor-Green vortex problem is a challenging case to tackle. The flow is periodic, incompressible and consists of decaying vortices. The 2D case of the problem is analytically defined as given by [Eq. 3.1](#) - [Eq. 3.3](#).

$$v_x = -Ue^{bt} \cos(2\pi x) \sin(2\pi y), \quad (3.1)$$

$$v_y = Ue^{bt} \sin(2\pi x) \cos(2\pi y), \quad (3.2)$$

$$p = (Ue^{bt})^2 \frac{\cos(4\pi x) + \cos(4\pi y)}{4}, \quad (3.3)$$

$$b = -\frac{8\pi}{Re}, \quad Re = \frac{UL}{\nu}, \quad (3.4)$$

where (U, Re, L) are flow constants.

The 3D case of the problem, defined for a tri-periodic domain with boundary ($\Omega = [0, 2\pi]^3$) is initially set-up as given in [Eq. 3.5](#) - [Eq. 3.7](#).

$$v_{x,0} = \sin(x) \cos(y) \cos(z), \quad (3.5)$$

$$v_{y,0} = -\cos(x) \sin(y) \cos(z), \quad (3.6)$$

$$v_{z,0} = 0. \quad (3.7)$$

The corresponding initial pressure field (P_0) obtained from solving the pressure Poisson equation for incompressible flow is given by Eq. 3.8 (Pereira et al. 2021).

$$P_0 = P_o + \frac{\rho_o v_o^2}{16} \left(2 + \cos(2z) \right) \left(\cos(2x) + \cos(2y) \right). \quad (3.8)$$

3.1.2 Thin Double-Shear Layer

The thin double-shear layer is a problem often considered to be too difficult to simulate due to the small scales which are produced. The main challenge of the problem, as shown by Minion and Brown 1997, occurs when a numerical method produces spurious structures, especially when the flow is sufficiently under-resolved. Drikakis and Smolarkiewicz 2001 studied the problem's spurious structure to understand its numerical mechanism. They indicated that the spurious structure's generation depends on the advective scheme's choice.

The initial conditions for the 2D periodic flow is given by:

$$v_{x,0} = \tanh(80 \times \min[y - 0.25, 0.75 - y]), \quad (3.9)$$

$$v_{y,0} = \delta \sin(2\pi(x + 0.25)). \quad (3.10)$$

3.1.3 3D Isotropic Turbulence

The JHU Turbulence Database Cluster (Y. Li et al. 2008) provide a direct numerical simulation (DNS) data set for isotropic, forced turbulence. The data set consists of the DNS output on 1024^3 spatial points and 1024 time samples spanning about one large-scale turnover time.

The entire 1024^4 space-time history of the incompressible DNS simulation ($Re \approx 1460$) is accessible to users remotely through an interface based on the Web-services model. The data from the database contains the three velocity components and the pressure. A uniform non-dimensionalised pressure ($P^* = \frac{p}{\rho U^2} + 1$) is added to the database pressure, with Mach number Ma 0.1.

3.1.4 2D Confined & Driven Turbulence

Based on the test case employed by J. J. Monaghan 2017, a 2D fluid confined to a square solid impenetrable boundary is considered ($\Omega = [0, 1]^2$). A cylinder of radius ($r = 0.7$) is placed at the centre of the box. The circle is subsequently provided with a Lissajous trajectory to follow given by:

$$x = 0.5 + 0.25 \sin\left(\frac{2\pi t}{5}\right), \quad (3.11)$$

$$y = 0.5 + 0.25 \sin\left(\frac{4\pi t}{5}\right). \quad (3.12)$$

3.1.5 Free Surface Flows

As seen in numerous works involving turbulence models in the previous chapter, there does not appear to be any dearth of experimental and numerical research on free-surface flows. Problems ranging from the classic 2D and 3D dam break to wave

propagation, wave breaking, water overtopping, and dyke-flow inspired problems can be simulated. The only caveat involved in such cases includes the resolution requirements of the problem and the approach taken in free surfaces boundary condition implementation.

3.2 Post-Simulation Analysis

3.2.1 Energy Spectral Density

In order to analyse the predicted flow and validate the turbulent model, energy spectra are the most used description since it has to fall off as prescribed by the Kolmogorov - 5/3 Law. Typical mesh or grid-based methods facilitate the calculation of the energy spectrum ($E[\mathbf{k}]$) by using the Fourier transform of the velocity field as given in Eq. 3.13, to obtain the velocity spectrum as defined in Eq. 3.14.

$$\mathbf{V}(\mathbf{k}) = \frac{1}{L^3} \int \exp(-i\mathbf{k} \cdot \mathbf{r}) \mathbf{v}(\mathbf{r}) d\mathbf{r}, \quad (3.13)$$

where ($d\mathbf{r} = dx dy$) for 2D and ($d\mathbf{r} = dx dy dz$) for 3D, and [$\mathbf{k} = (k_x, k_y, k_z)$] is the wave-number vector.

$$E(\mathbf{k}) = \frac{1}{2} |\mathbf{V}(\mathbf{k}) \cdot \mathbf{V}^*(\mathbf{k})|. \quad (3.14)$$

The energy spectrum is subsequently defined as given by Eq. 3.15 for the case of isotropic turbulence.

$$E(k) = B \langle E(\mathbf{k}) \rangle, \quad k = |\mathbf{k}|, \quad (3.15)$$

where ($B = 2\pi k$) for 2D and ($B = 4\pi k^2$) for 3D.

However, SPH does not have such grid-like data to calculate the energy spectrum directly. Hence, the data has to be reconstructed using interpolation methods as outlined by Shi et al. 2013. The authors provide three distinct methods of interpolating the data across a grid-like space. The SPH interpolation method specified by the authors is given below:

$$A(\mathbf{r}) \approx \sum_j A_j W(|\mathbf{r} - \mathbf{r}_j|, h) \mathcal{V}_j. \quad (3.16)$$

The remeshed interpolation method is given by:

$$A(\mathbf{r}) \approx \sum_j A_j \tilde{W}(|x - x_j|, h) \tilde{W}(|y - y_j|, h) \tilde{W}(|z - z_j|, h), \quad (3.17)$$

where (\tilde{W}) represents the kernel where the volume of the particle (\mathcal{V}_j) has been absorbed.

The authors also detail the moving least squares (MLS) method as an interpolation tool. Building on the work of Lancaster and Salkauskas 1981, who were able to extend the 2D interpolation technique proposed by Shepard 1968 to a general higher-order case. The authors state that they start with a weighted least squares formulation for an arbitrary fixed point and then move said point across the entire domain. This allows for the computation of a weighted least squares fit function, which can be used to evaluate grid-like points.

3.2.2 Lagrangian Coherent Structures

Complex flow cannot only be analysed through primitive flow properties such as pressure, velocity or energy density for a deep understanding of the flow interactions. Techniques using only such properties would fail to identify general coherent structures (CS) in the flow. To facilitate that, quantities such as those employing the velocity gradient, such as the vorticity, Q-criterion, Δ -criterion, swirling strength criterion, etc., are used. However, Haller 2005 was able to show that in some situations, most of the definitions of the vortex are not objective and suitable for studying the flow, particularly in the context of 3D flow.

Therefore, Sun, Colagrossi, et al. 2016 utilise the Lagrangian Coherent Structures (LCSs) as an alternative way with specific advantages for drawing the CSs from a given flow field. In order to identify the LCSs with an objective quantity, the authors use the Finite-time Lyapunov Exponent (FTLE), which represents the rate of separation of the nearby fluid particles over a finite time interval. FTLEs can be evaluated both in forward and backward time directions.

The authors summarise the main advantages of FTLEs over different velocity gradient-based metrics as follows:

- Local fluctuations of the velocity field do not induce noise to FTLEs since they are integrated in time.
- FTLE is formulated in the Lagrangian frameworks allowing for better identification of the LCSs with respect to quantities derived from the velocity gradient.
- FTLE can identify LCSs with an accuracy that, in some cases, resemble those obtained from advanced experimental techniques.

The forward-in-time FTLE is calculated using the forward-in-time Right-Cauchy–Green strain tensor, while backward-in-time FTLE requires the Left-Cauchy–Green strain tensor. The authors propose two methods to calculate a flow's Cauchy–Green strain tensors.

The first method uses SPH formulations for the deformation gradient to compute the Cauchy–Green strain tensors. The backward-in-time FTLE can be computed using limited resources during run-time concurrently in this method. However, the forward-in-time FTLE can only be computed during post-processing.

In the second method, the forward-in-time deformation gradient is evolved as a property within the simulation's time integration step employing a governing equation for the property. This method does not need to keep track of the spatial relation between the points. This allows for the process to be suitable for Eulerian solvers as well. Building on this work, Dauch et al. 2018 developed an efficient GPU-based implementation to accelerate the computation of FTLE fields or, depending on the architecture of the solver, completely move the step from being calculated on the CPU to the GPU. Their proposition is highly enticing, especially for 3D flows.

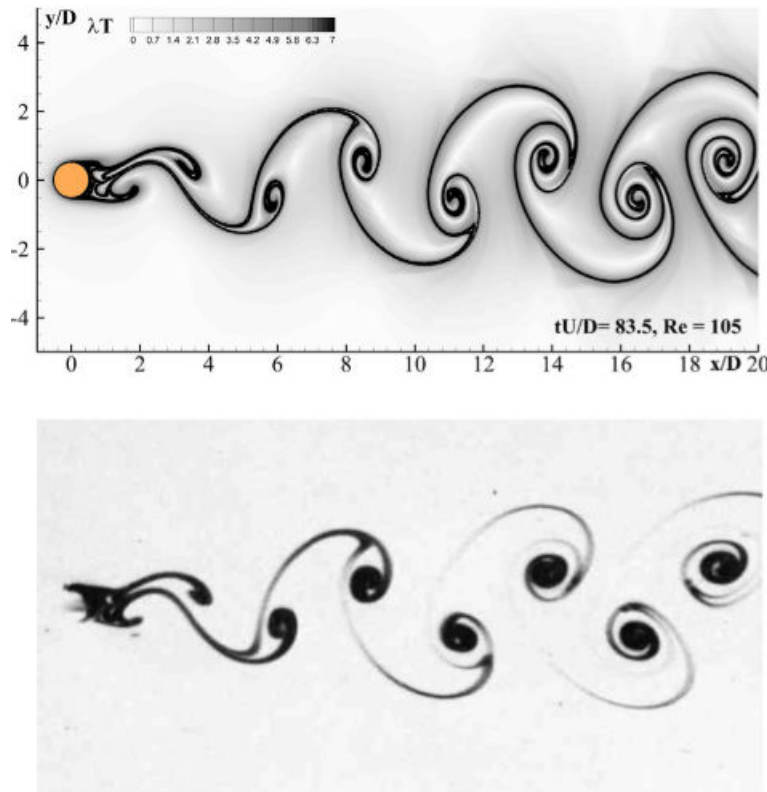


Figure 3.1: Viscous flow past a circular cylinder at $Re = 105$. Top: Attracting FTLE contour plot from SPH simulation. Bottom: Photo from experiments conducted by Taneda 1977 with electrolytic precipitation in water technique for vortex street visualisation. Reproduced from Sun, Colagrossi, et al. 2016

4 Results

4.1 Turbulence-specific Post-processing

In order to make available all of the turbulence-specific post-processing from a given simulation output of PySPH (Prabhu Ramachandran, Bhosale, et al. 2021), generated through the `Application` class, a `TurbulentFlowApp` class was created. This class inherits from the `Application` class and adds additional post-processing attributes and methods, such as:

- class attributes:
 - number of interpolation points along each axis,
 - kernel to be used for the interpolation, and the corresponding kernel radius,
 - interpolation method,
 - norm order to be used for the computation of the 1D energy spectrum (also referred to as the *scalar energy spectrum*),
 - expected slope for the 1D energy spectrum,
 - type of FTLE field (either *forward* or *backward*),
- class methods:
 - `compute_interpolated_vel_field`: to compute the interpolated velocity field at specified indices of the output files,
 - `compute_ek`: to compute the 1D energy spectrum from the corresponding interpolated velocity field,
 - `compute_ek_slope`: to compute the slope of the 1D energy spectrum, using the `scipy.stats.linregress` function,
 - `compute_ftle`: to compute the FTLE (Finite-time Lyapunov Exponent) field, using the corresponding interpolated velocity field between two specific output files,
 - plotter functions that can plot the 1D energy spectrum for a specific output file (along with a fit line), plot the evolution of the 1D energy spectrum over a range of output files, or plot the FTLE field.

The derived class is also coded to log the details of the interpolator used, which includes details on the kernel, radius scale, problem dimension, and SPH equations involved in the interpolation scheme in the original problem.log file created by the default `Application` class. This enables the user to keep track of the simulation's relevant details, including its post-processing, in a single log file.

The following subsections detail the implementation of the energy spectrum and FTLE field computation and essential observations made from the same.

4.1.1 Energy Spectral Density

In order to compute the energy spectrum, the following steps are performed:

- the velocity field is interpolated along a grid of uniformly spaced rectangular points,
- the velocity field is then transformed to Fourier space, using the `numpy.fft.fftn` function (Harris et al. 2020), and subsequently normalised as given as:

$$\hat{v}_i(\mathbf{k}) = \frac{\text{fft}\{\mathbf{v}_i(\mathbf{r})\}}{U_0 \times \text{len}(\mathbf{v}_i)}, \quad (4.1)$$

where U_0 is a reference velocity and \mathbf{v}_i is the i^{th} component of the velocity field,

- the corresponding energy spectrum is then computed as:

$$E_i(\mathbf{k}) = \frac{1}{2} \hat{v}_i^2, \quad (4.2)$$

- the 1D energy spectrum $E(k)$ is then computed from the energy vector field $E_i(k_x, k_y, k_z)$, by integrating it over the surface of a sphere of appropriate dimension between the limits $k = 0$ and $k = k_{max}$, where k_{max} is the maximum wavenumber of the energy spectrum, where:

$$k_{max} = \text{round}(1 + \text{ceil}((l_x, l_y, l_z)/2)). \quad (4.3)$$

The function to compute the 1D energy spectrum was coded using three different backends, namely, pure python, `numba` (Lam, Pitrou, and Seibert 2015), and `compyle` (Bhosale and Ramachandran 2020). The speedup results of the three implementations are shown in Fig. 4.1 for 1D, 2D, and 3D velocity fields, respectively.

The speedup plots show that the `numba` implementation is around $50 - 100 \times$ faster than the pure python implementation. In comparison, the `compyle` implementation is around $80 - 150 \times$ faster than the pure python implementation for various resolution scales. These trends are observed across all dimensions of the velocity field. The `compyle` implementation, in addition, to being faster than the `numba` implementation, also has the added advantage of not requiring any additional dependencies, which are not already required by PySPH, unlike the `numba` implementation, which requires the `numba` package to be installed separately. Hence, the `compyle` implementation was chosen for the final implementation of the 1D energy spectrum computation.

In order to test the code for correctness, the following test cases were devised. The velocity field for 1D, is given as:

$$v_x = - \sum_{i=1}^N i^{-\gamma} \cos(2\pi i x), \quad (4.4)$$

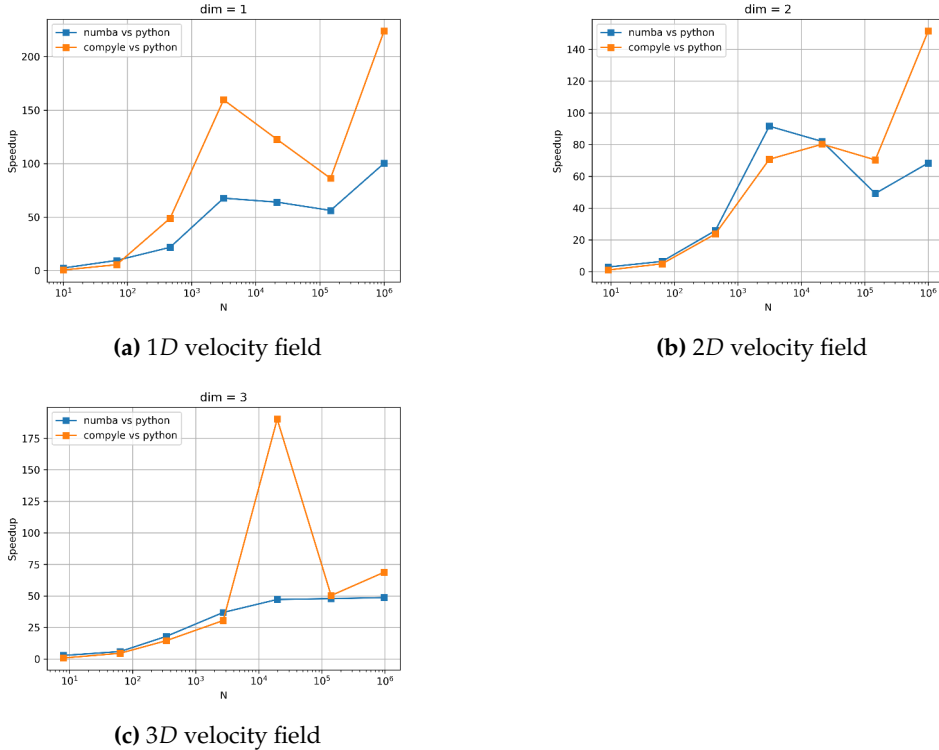


Figure 4.1: Speedup of the 1D energy spectrum computation for various dimensions of the velocity field.

where, N is the number of modes, and γ is the decay rate of the modes. For 2D, the velocity field is given as:

$$v_x = - \sum_{i=1}^N i^{-\gamma} \cos(2\pi i x) \sin(2\pi i y), \quad (4.5)$$

$$v_y = \sum_{i=1}^N i^{-\gamma} \sin(2\pi i x) \cos(2\pi i y). \quad (4.6)$$

For 3D, the velocity field is given as:

$$v_x = - \sum_{i=1}^N i^{-\gamma} \cos(2\pi i x) \sin(2\pi i y) \sin(2\pi i z) \quad (4.7)$$

$$v_y = \sum_{i=1}^N i^{-\gamma} \sin(2\pi i x) \cos(2\pi i y) \sin(2\pi i z) \quad (4.8)$$

$$v_z = \sum_{i=1}^N i^{-\gamma} \sin(2\pi i x) \sin(2\pi i y) \cos(2\pi i z). \quad (4.9)$$

Since the energy in the flow field is a function of the square of the velocity, the corresponding decay rate in the energy spectrum will be 2γ .

The first order of correctness involved running the energy spectral calculation for the above test cases, using only one mode ($N = 1$) and zero decay rate ($\gamma = 0$).

The vector energy spectral fields are shown in Fig. 4.2. It should be noted that

the plots are shown by shifting the energy spectrum such that the centre of the plot corresponds to the zero wavenumber. This is done since the energy spectrum is symmetric about the zero wavenumber, and hence, the plot is more informative when the zero wavenumber is at the centre of the plot. Here, it can be observed that in both the 1D and 2D cases, the energy spectrum peaks only for $k = 1$ and is zero for every other wavenumber, indicating the nature of the velocity field, consisting of only one mode.

The scalar energy spectral fields are shown in Fig. 4.3. As can be seen, the energy spectrum peaks only for $k = 1$ and is zero for every other wavenumber for all dimensions.

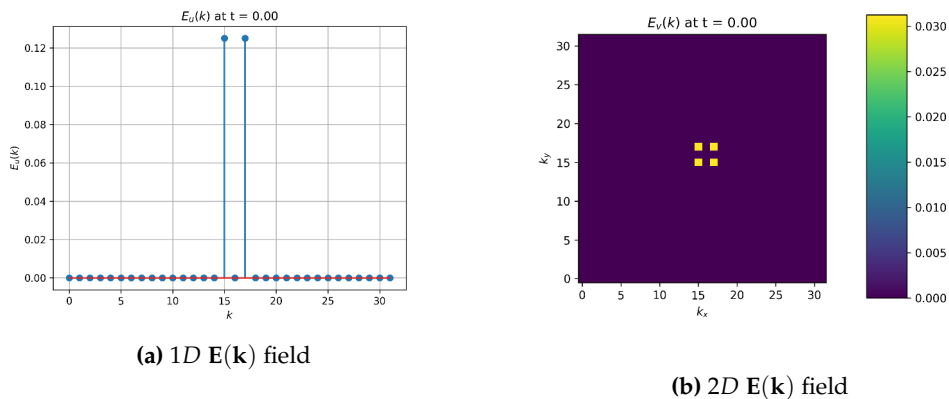


Figure 4.2: The vector fields $\mathbf{E}(\mathbf{k})$ for 1D and 2D case, with decay rate $\gamma = 0$, and $N = 1$. Note: The plots are shown by shifting the energy spectrum such that the centre of the plot along each axis corresponds to the zero wavenumber for that axis.

Subsequently, the test cases were reconsidered to test the correctness when multiple modes are involved, with $\gamma = 1$ and N equal to half the number of particles along one axis of the problem.

The vector energy spectral fields are shown in Fig. 4.4. Here, it can be observed that in both the 1D and 2D case, the energy spectrum peaks for $k = 1$ and is non-zero up to $k = n_x/2$, indicating the nature of the velocity field, consisting of multiple modes. The amplitudes are also observed to have an exponential drop-off, as is expected, given the nature of the amplitude weighting.

This is made all the more apparent with the scalar energy spectral fields shown in Fig. 4.5. The log-log plots here allow for the exponential drop-off to be observed more clearly, by fitting a straight line to the log-log plot between wavenumbers $k \in [1, n_x/4]$. The green-dashed lines, which represent the scalar energy spectrum computed for the original velocity field (which is uniform and rectangular) without interpolation, represent the ‘best’-case scenario, where the energy spectrum is computed without any loss of information in the velocity field, and the source of noise can be solely attributed to numerical errors from the discrete Fourier transform. The scalar energy spectrum computed from the interpolated velocity is plotted in blue.

It is observed that the energy spectrum computed without interpolation is indeed the ‘best’-case scenario since it much more closely follows the exact trend. However, with the computed energy spectrum from the interpolated velocity field, the trend is

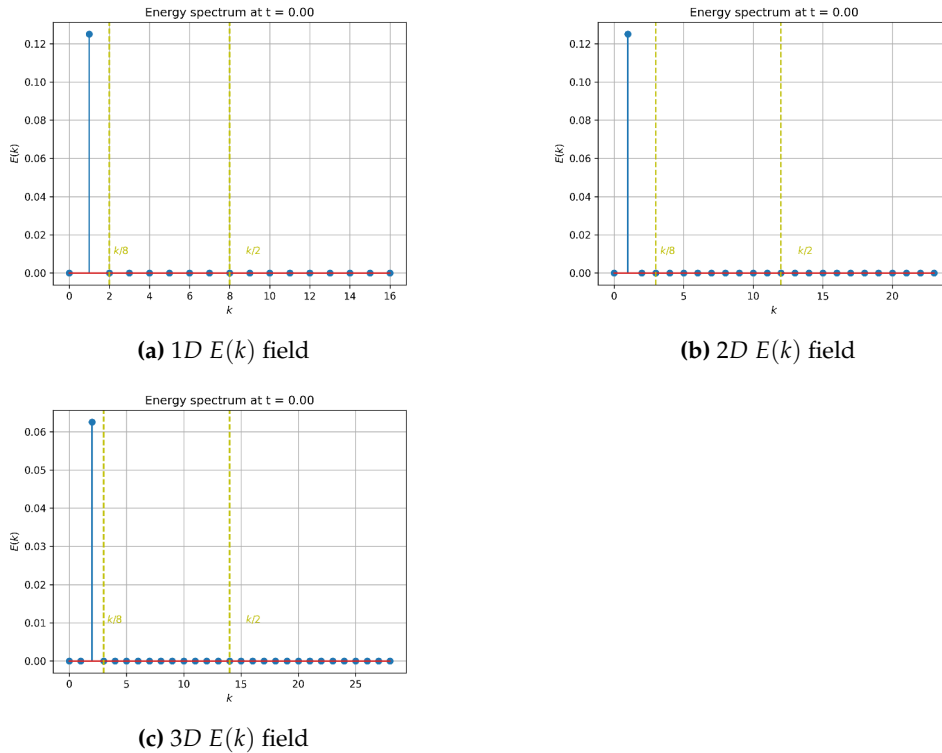


Figure 4.3: The scalar fields $E(k)$ for 1D, 2D, and 3D case, with decay rate $\gamma = 0$, and $N = 1$.

still observed to be followed, but only up to the $k/8$ wavenumber, beyond which the trend is lost, and the computed energy spectrum is observed to be much lower than the green-dashed line, with the difference increasing with the wavenumber. This seems to indicate that the act of interpolation itself is introducing some amount of noise in the velocity field, which is reflected by the jagged nature of the blue line, and also seems to decrease the energy at lower scales, which is reflected by the blue line being consistently lower than the green-dashed line at lower wavenumbers. This allows for the conclusion that the interpolation scheme behaves as a low-pass filter, which is expected since the interpolation scheme is essentially a convolution of the velocity field with the kernel function, which is a low-pass filter.

Therefore, it was concluded that the 1D energy field, computed from the interpolated velocity field, typically will underestimate the energy at higher wavenumbers. Hence, the slope of the energy spectrum computed from the interpolated velocity field will be lower than the slope computed from the original velocity field, as reflected in Fig. 4.5 as well.

The same set of test cases, with $\gamma = 1$ and $N = n_x/2$, are considered to identify the effect of various interpolation schemes, kernels, perturbation, and resolutions on the computed energy spectrum.

In order to measure the effect of the perturbation in the particle spacing on the computed energy spectrum, once a rectangular grid of uniform particles is defined, its coordinates are perturbed by a uniform random number $\delta\hat{x} \in [0, 1)$, scaled by a perturbation amplitude. The perturbed grid is then initialised with the corresponding velocity profile, and the energy spectrum is computed for the perturbed grid. From the results shown in Fig. 4.6, it can be observed that by increasing the perturbation

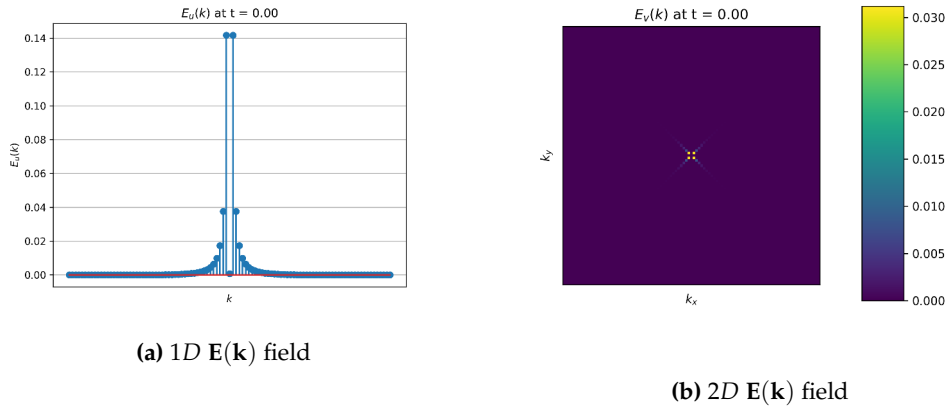
(a) 1D $\mathbf{E}(\mathbf{k})$ field(b) 2D $\mathbf{E}(\mathbf{k})$ field

Figure 4.4: The vector fields $\mathbf{E}(\mathbf{k})$ for 1D and 2D case, with decay rate $\gamma = 1$, and $N = n_x/2$. Note: The plots are shown by shifting the energy spectrum such that the centre of the plot along each axis corresponds to the zero wavenumber for that axis.

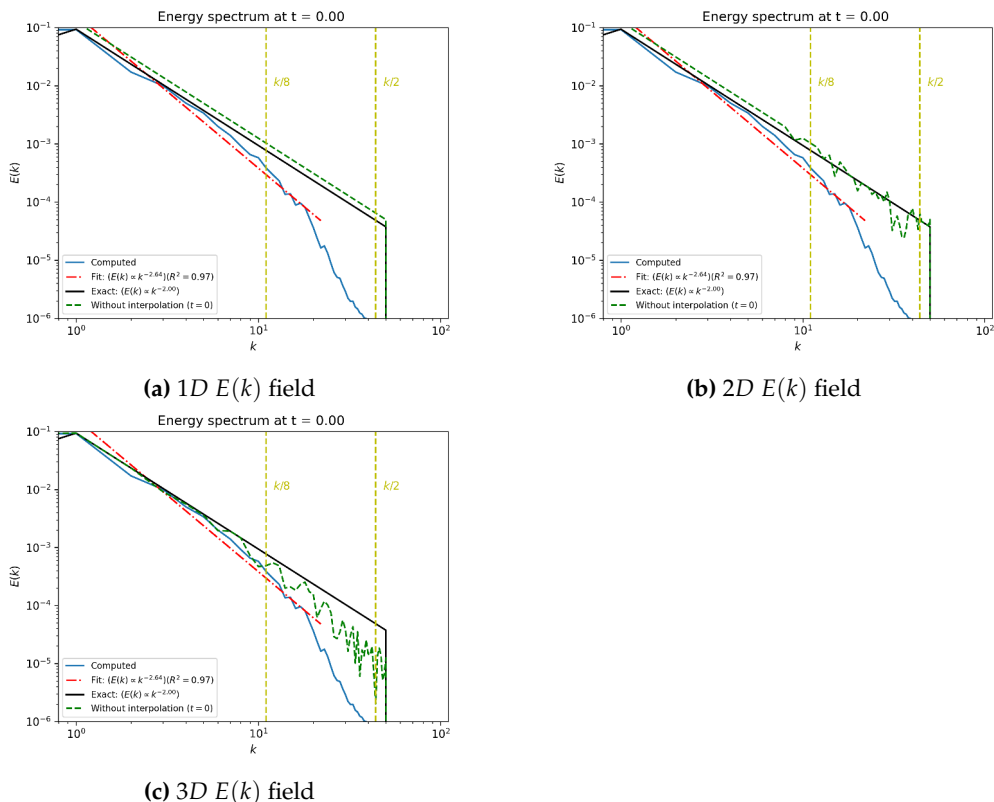


Figure 4.5: The scalar fields $E(k)$ for 1D, 2D, and 3D case, with decay rate $\gamma = 1$, and $N = n_x/2$.

amplitude, energy seems to be introduced at lower resolution scales, which is reflected by the increased energy at higher wavenumbers. This trend seems to hold for all dimensions. Therefore, we can infer that the low-pass energy dissipation effect of the interpolation scheme will to an extent, be countered by the perturbation in the particle spacing (which is typically the case in a simulation since the particles become disturbed), which will introduce energy at lower resolution scales, and hence, the slope of the energy spectrum computed from the interpolated velocity field will be closer to the slope of the energy spectrum computed from the original velocity field.

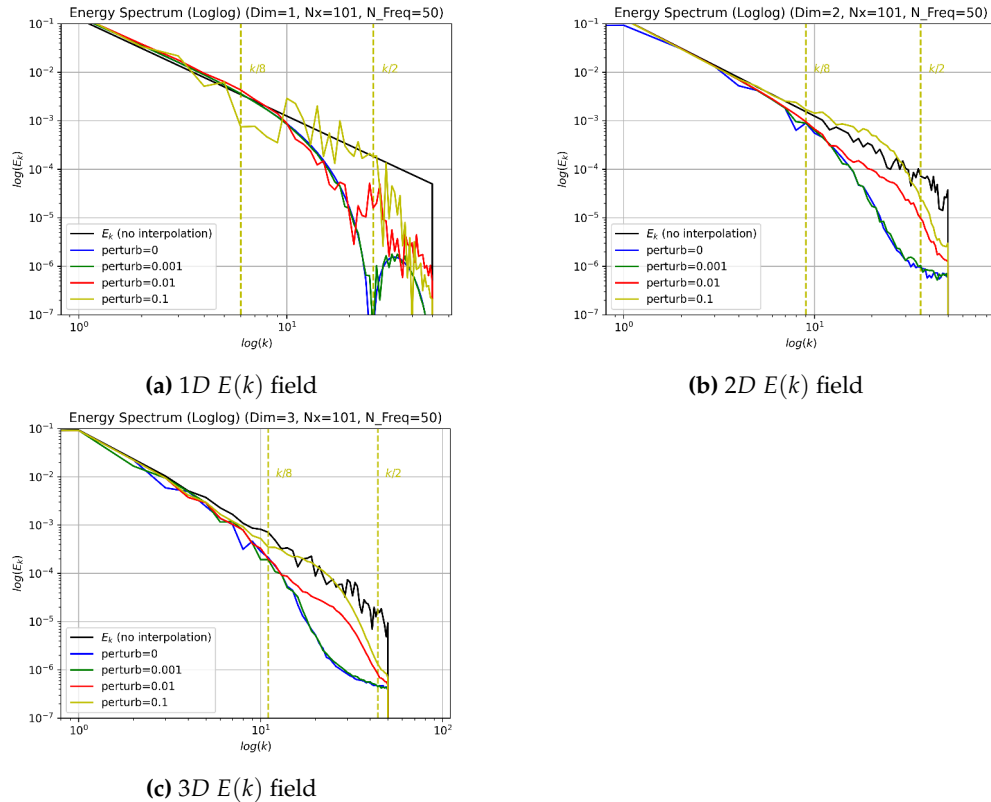


Figure 4.6: The scalar fields $E(k)$ for 1D, 2D, and 3D case, for various perturbation amplitudes.

Then, in order to measure the effect of the interpolation scheme on the computed energy spectrum, the following interpolation schemes were considered:

- sph:

$$\hat{\phi}_i = \sum_{ij} \frac{m_j}{\rho_j} \phi_j \nabla_i W_{h,ij}, \quad (4.10)$$

where ϕ is the quantity to be interpolated, and $\hat{\phi}$ is the interpolated quantity,

- shepard:

$$\hat{\phi}_i = \frac{\sum_{ij} \phi_j W_{h,ij}}{\sum_{ij} W_{h,ij}}, \quad (4.11)$$

- order1 (M. B. Liu and G. R. Liu 2006):

$$\underline{A}_{4 \times 4} \mathbf{x}_{4 \times 1} = \mathbf{b}_{4 \times 1}, \quad (4.12)$$

where \mathbf{A} is the moment matrix, $\mathbf{b} = [\phi, \nabla\phi]^T$ is the interpolated property, and its gradient is calculated using basic SPH, and $\mathbf{x} = [\hat{\phi}, \nabla\hat{\phi}]^T$ is the unknown interpolated property and its gradient,

- `order1BL`: same as Eq. 4.12, but with the $\nabla_i W_{h,ij}$ term corrected using the Bonet-Lok correction (Bonet and Lok 1999),
- `order1MC`: same as Eq. 4.12, but with the $\nabla_i W_{h,ij}$ term corrected using the Mixed-Kernel correction (Bonet and Lok 1999).

From the results shown in Fig. 4.7, it can be observed that the `order1MC` interpolation scheme seems to introduce the least amount of energy at lower resolution scales, with the `sph` scheme introducing the most amount of energy at lower resolution scales. This trend seems to hold for all dimensions. Therefore, because the `sph` interpolation scheme would appear to counter the loss in energy at lower resolution scales due to the act of interpolation, it is chosen as the default interpolation scheme for the computation of the energy spectrum.

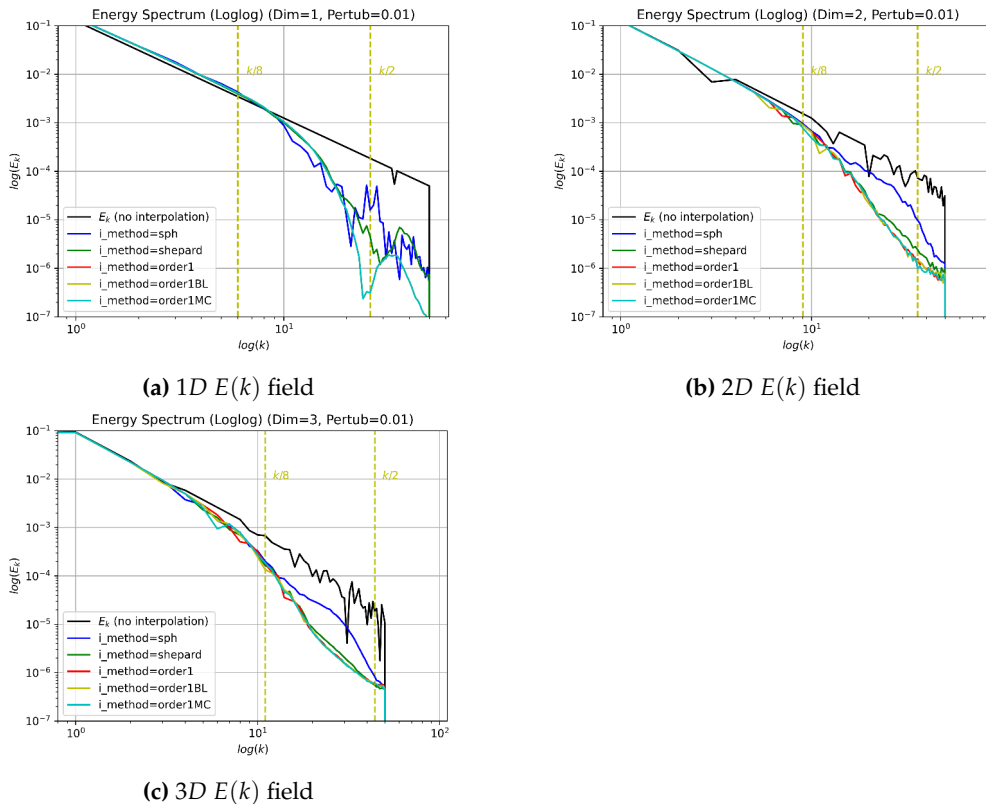


Figure 4.7: The scalar fields $E(k)$ for 1D, 2D, and 3D case, for various interpolation schemes.

Then, in order to measure the effect of the kernel on the computed energy spectrum, the following kernels were considered:

- `CubicSpline`,
- `WendlandQuinticC2`,
- `WendlandQuinticC4`,
- `WendlandQuinticC6`,

- Gaussian,
- SuperGaussian,
- QuinticSpline.

From the results shown in Fig. 4.8, it can be observed that all kernels underestimate the energy at lower length scales, with the Gaussian kernel underestimating the most. The WendlandQuinticC6 kernel seems to predict the energy spectrum closest to the exact trend, which holds for all dimensions. Therefore, the WendlandQuinticC6 kernel is chosen as the default kernel for the computation of the energy spectrum.

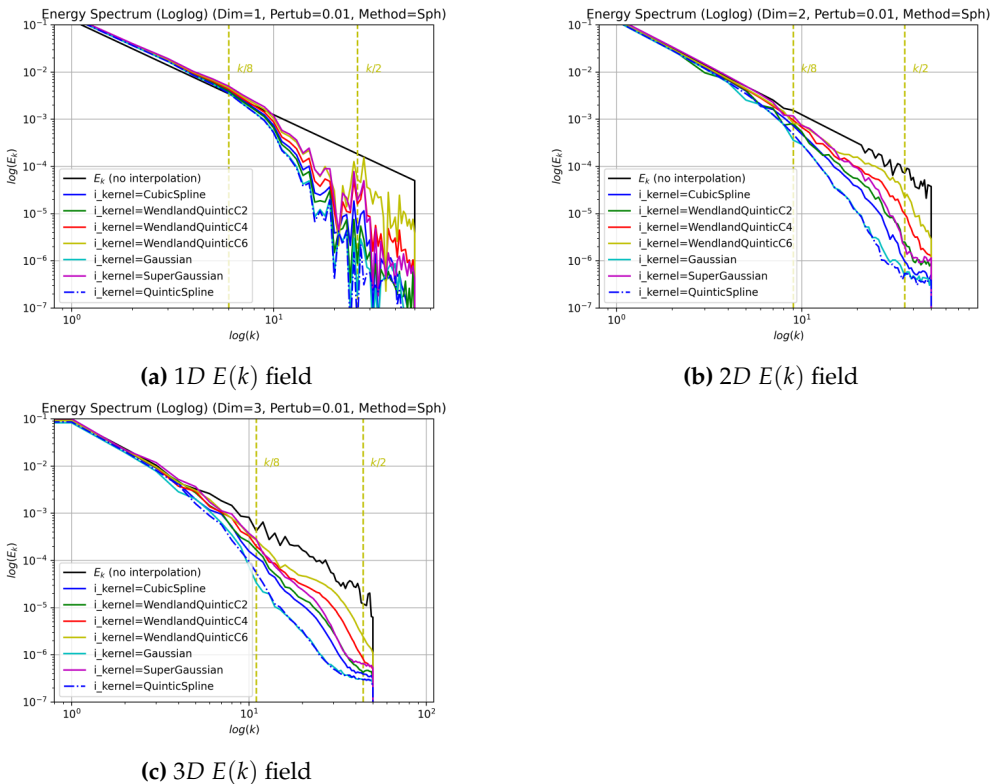


Figure 4.8: The scalar fields $E(k)$ for 1D, 2D, and 3D case, for various interpolation kernels.

Finally, in order to measure the effect of particle resolution on the computed energy spectrum, test cases with a $\gamma = 1$ and $N = 30$ were considered for all dimensions, with the range of the number of particles along each axis being [61, 91, 121]. From the results shown in Fig. 4.9, it can be observed that the energy spectrum computed for the highest resolution is observed to be the closest to the exact trend for all dimensions.

4.1.2 Finite-time Lyapunov Exponent (FTLE) Field

In order to compute the FTLE field, the flow field, at two different time instances, is required, i.e., t_i and t_f . The flow field corresponding to the earlier time instance is stored in the `initial` particle array, while the flow field corresponding to the later time instance is stored in the `final` particle array.

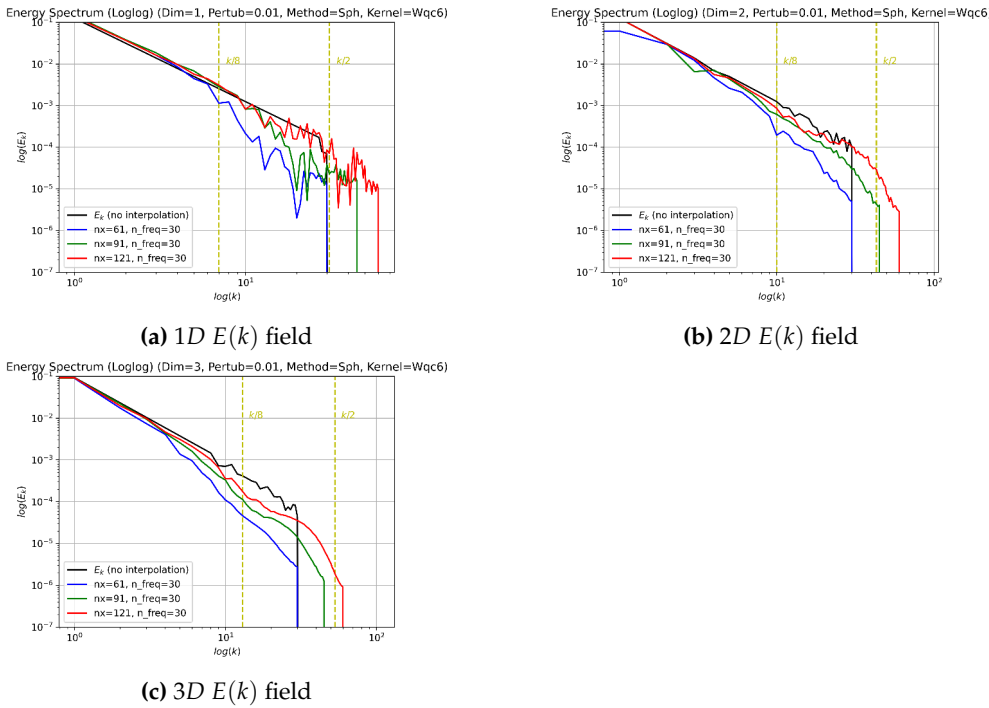


Figure 4.9: The scalar fields $E(k)$ for 1D, 2D, and 3D case, for various particle resolutions.

The forward-in-time (FIT) FTLE field is calculated as defined in the work of Sun, Colagrossi, et al. 2016:

$$\lambda_{t_i}^{t_f}(\mathbf{x}) = \frac{1}{|t_f - t_i|} \ln \left(\sqrt{\Lambda_{\max}[\mathbb{C}_{t_i}^{t_f}(\mathbf{x})]} \right), \quad (4.13)$$

$$\mathbb{C}_{t_i}^{t_f}(\mathbf{x}) = \mathbb{F}_{t_i}^{t_f}(\mathbf{x})^T \mathbb{F}_{t_i}^{t_f}(\mathbf{x}), \quad (4.14)$$

where, $\mathbb{F}_{t_i}^{t_f}(\mathbf{x})$ is the deformation gradient tensor, and Λ_{\max} is the maximum eigenvalue of the Cauchy-Green tensor $\mathbb{C}_{t_i}^{t_f}(\mathbf{x})$. Correspondingly, the backward-in-time (BIT) FTLE field is calculated as:

$$\lambda_{t_f}^{t_i}(\mathbf{x}) = \frac{1}{|t_f - t_i|} \ln \left(\sqrt{\frac{1}{\Lambda_{\min}[\mathbb{C}_{t_i}^{t_f}(\mathbf{x})]}} \right). \quad (4.15)$$

The corresponding SPH approximations for the above equations are:

$$\mathbb{F}_{t_i}^{t_f}(\mathbf{x}_i) = \sum_j \frac{m_j}{\rho_j} \mathbf{X}_{ji} \otimes \nabla \mathbb{L}(\mathbf{x}_i) \nabla_i W_{h,ij}, \quad (4.16)$$

$$\mathbb{L}(\mathbf{x}_i) = \left[\sum_j \mathbf{x}_{ji} \otimes \nabla_i W(|\mathbf{x}_{ji}|, h_i) \right]^{-1}, \quad (4.17)$$

where $(\mathbf{x}_i, \mathbf{X}_i)$ corresponds to the initial and final position of the same particle.

In order to test the correctness of the FTLE field computation, the following test cases were devised.

- parabolic:

$$X = 1.5x, \quad Y = x^2 + y, \quad (4.18)$$

- spiral:

$$X = x + 0.1 \cos(2\pi r^2), \quad Y = y + 0.1 \sin(2\pi r^2), \quad r = \sqrt{x^2 + y^2}. \quad (4.19)$$

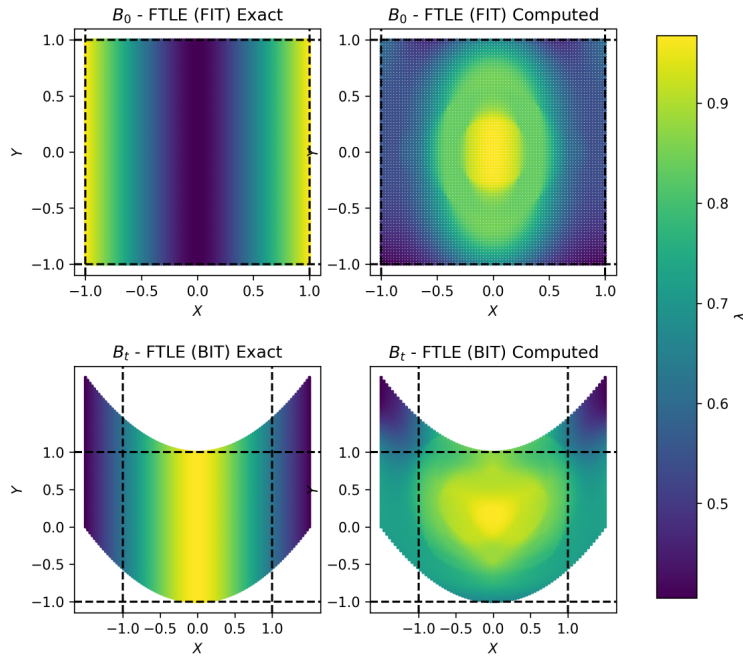


Figure 4.10: Parabolic displacement field

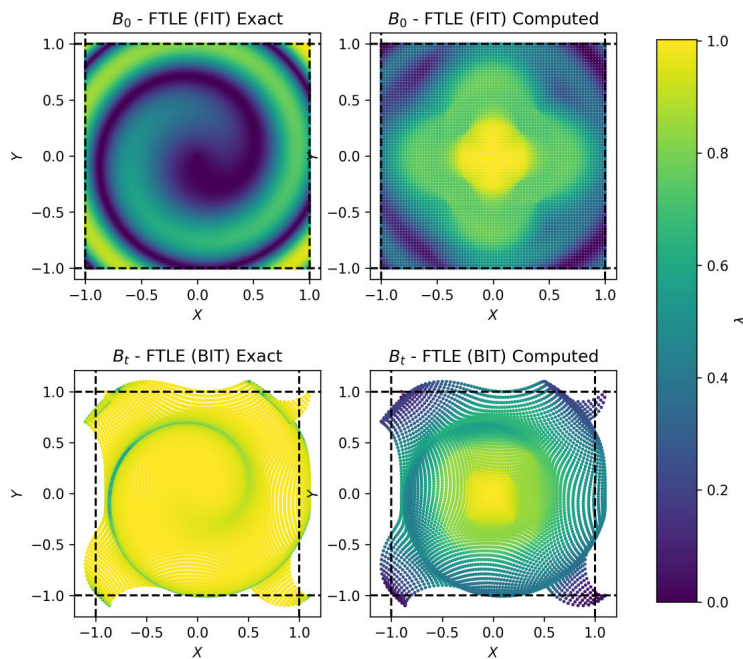


Figure 4.11: Spiral displacement field

As seen in [Fig. 4.10](#) and [Fig. 4.11](#) (B_0 : initial configuration, B_t : final configuration), it can be observed that although the FTLE field is capable of qualitatively capturing the evolution of the configurations, i.e., attracting/repelling pathlines, it is however, not as accurate in terms of actually capturing the exact pathlines. Therefore, it was concluded that in place of FTLE fields, tracer particles could be used to visualise the flow field, which would be more accurate in terms of capturing the exact pathlines but would be computationally more expensive since the tracer particles would have to be advected along with the flow field, and would also require additional post-processing to visualise the pathlines. They would also have to be done in situ, i.e., during the simulation itself, as opposed to the FTLE fields, which can be computed post-simulation or in situ.

4.2 Turbulence Modelling

4.2.1 Implementation of Models

A broad classification of the major categories of turbulence models has already been discussed in [Chapter 2](#). In order to better understand the nature of each major category and to subsequently understand the implementation of the same, a select few representative schemes from each of these models are considered, which are listed in [Table 4.1](#).

Turbulence Model	Review Section	Scheme Name	Reference
Viscosity-based Model	Sec. 2.1	Lagrangian with iterative PST and coupled_c viscosity formulation (L-IPST-C)	Negi and Prabhu Ramachandran 2022
Large Eddy Simulation-based Model	Sec. 2.2	SPH-LES	Okrashevski et al. 2022
Lagrangian LES-based Model	Sec. 2.3	δ -LES-SPH	Antuono et al. 2021
RANS-based k-epsilon Model	Sec. 2.4	$k - \epsilon$ SPH	Songdeng Shao 2006
LANs-based Model	Sec. 2.5	SPH-e	J. J. Monaghan 2017

Table 4.1: Implementation of representative turbulence models.

In order to test the schemes for SOC, the Taylor-Green vortex (TGV) problem is chosen. The test cases are coded using `automan` (P. Ramachandran [2018](#)), an open-source, Python-based automation framework. All of the simulations run hereafter are run upto a final time of $t_f = 0.1$, with the resolution for each run consisting of $N = [25^2, 50^2, 100^2]$ particles respectively, with the Reynolds number ranging between $Re = [100, 1000, 10000]$ respectively. All simulations are run using the `WendlandQuinticC4` kernel, with a radius multiplier of 2.0. This choice was based on the work of Negi and Prabhu Ramachandran [2022](#).

The L_1 error for each simulation in a run is computed and plotted against the particle spacing inverse to evaluate the scheme's order of convergence (OOC). The L_1 error at a given time instance is computed as:

$$L_1(t) = \frac{\text{mean}|\mathbf{v}^2(t) - \mathbf{v}_{\text{exact}}^2(t)|}{\text{mean}|\mathbf{v}_{\text{exact}}^2(t)|}, \quad (4.20)$$

where, $\mathbf{v}(t)$ is the velocity field at time t , and $\mathbf{v}_{\text{exact}}(t)$ is the exact velocity field at time t . Subsequently, the L_1 error for the entire simulation is defined as the mean over all the time instances, i.e.,

$$L_1 = \frac{1}{n_t} \sum_{i=1}^{n_t} L_1(t_i). \quad (4.21)$$

4.2.2 L-IPST-C Scheme

The L-IPST-C scheme was considered over the other viscosity-based schemes since it was observed to be second-order convergent (SOC) by Negi and Prabhu Ramachandran 2022, for a wide variety of problems, which included the Gresho vortex problem, Kelvin-Helmholtz instability problem, and the Taylor-Green vortex problem. This scheme considers the weakly-compressible NS equations the governing equations and uses the `coupled_c` viscosity formulation, which is corrected using the Bonet and Lok correction (Bonet and Lok 1999). Hence, since the scheme, by definition, has the viscous term in its governing equation, it does not require any additional ‘artificial’-viscosity term to be added. The scheme also incorporates the iterative particle shifting technique (IPST) by Huang et al. 2019 in order to redistribute the particles to obtain a reasonably uniform grid of particles in the domain. Besides shifting the position of the particles, the scheme also updates the particles’ properties, such as the density and velocity, to keep the approximation of the particle $O(h^2)$. Based on the parametric study conducted by Negi and Prabhu Ramachandran 2022, the proposed scheme is observed to be SOC by considering the speed of sound to be $c_s = 20$ and the shifting frequency for the particles through PST to be at every ten iterations $f_{pst} = 10$.

Since the study dealt with problems of low Re , the scheme was tested for various time integrators from the Runge-Kutta family of integrators to identify their effects and the most suitable integrator for problems of high Re . The integrators considered were:

- Predict-Evaluate-Correct (PEC),
- Runge-Kutta 2 (RK2),
- Runge-Kutta 2 with adaptive time-step (RK2 Adaptive),
- Runge-Kutta 3 (RK3), and
- Runge-Kutta 4 (RK4),

with a corresponding CFL values of [1, 1, 1.5, 2, 2] respectively.

From the results shown in Fig. 4.12, it is evident that the order of the integrator does not appear to have much effect on the OOC and almost negligible effect on the actual magnitude of the L_1 errors as well. This highlights a much more important aspect of the effect and role of time integrators in SPH: the time-step size is the most critical factor. The order of the integrator is less important since the time-step size is typically chosen to be small enough to ensure stability. Hence, the error introduced by the time integrator is typically negligible. As the Re number increases, the scheme loses SOC, which is also evident in Fig. 4.12, irrespective of the time integrator used. This effect will be discussed in the sections on long-time simulations of the TGV problem, with efforts made to provide a potential explanation.

Also, when the run-times of these integrators were analysed, the higher order integrators were observed to be more computationally expensive, allowing for the PEC integrator to be around $\approx 1.6 \times$ faster, which is reflected in the run-times shown in Fig. 4.13. Typically, higher-order integrators can be used with much larger CFL values, allowing for larger time steps and faster run times. However, in the case of SPH, such generalisations cannot be made since the stability of the scheme is not only dependent on the time-step size but also on the particle spacing, and hence, the

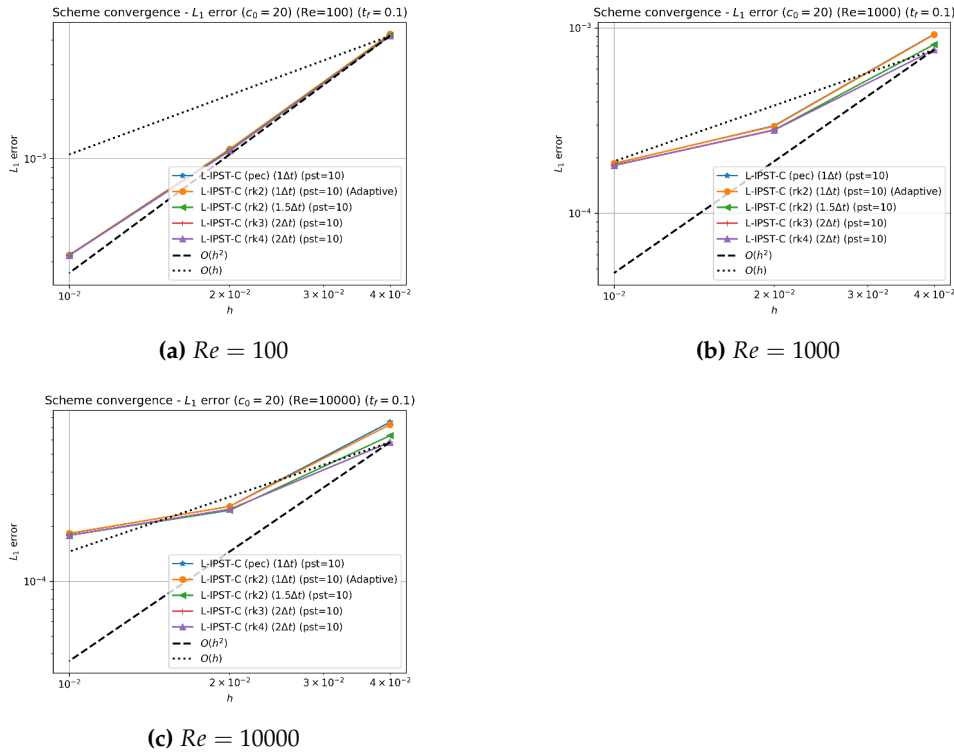


Figure 4.12: Convergence of the L-IPST-C scheme for various time-integrators.

CFL value is typically chosen to be close to 1.0 – 2.0. Therefore, the PEC integrator is chosen as the default integrator for the L-IPST-C scheme.

4.2.3 SPH-LES Scheme

The SPH-LES scheme was considered over the other LES-based schemes since the scheme utilised the compressible NS equations, which were treated with a spatial averaging operator to obtain the filtered governing equations. They also considered three different models for the turbulent eddy viscosity, which included the standard Smagorinsky model, σ -model and the standard model discretised in the Monaghan-Cleary-Gingold (MCG) form (detailed in Sec. 2.2.2.2). Therefore, the model appeared comprehensive in terms of its implementation and hence, was chosen, along with the SMAG model, which is the standard Smagorinsky model, since their study revealed that this model was the most accurate relatively in terms of its prediction of the energy spectrum while using the PEC integrator.

In order to identify the effects of the PST on the scheme, the following values were considered: $f_{pst} = [None, 10, 50, 100]$, with the speed of sound for the particles through PST to be $c_s = 20$. The results are shown in Fig. 4.14, where it can be seen that the scheme worryingly appears to be zero-order convergent. The velocity magnitude field and the energy spectrum are plotted to help provide a deeper insight into the issue. In Fig. 4.15, it can be observed that the particles get clustered without PST, and there are marked regions devoid of particles. It is also evident that high values of f_{PST} are also not desirable since the particles are still clustered and hence the formation of regions devoid of particles. Also, in Fig. 4.16, it can be observed that the slope of the energy spectrum at the final time instance (yellow line)

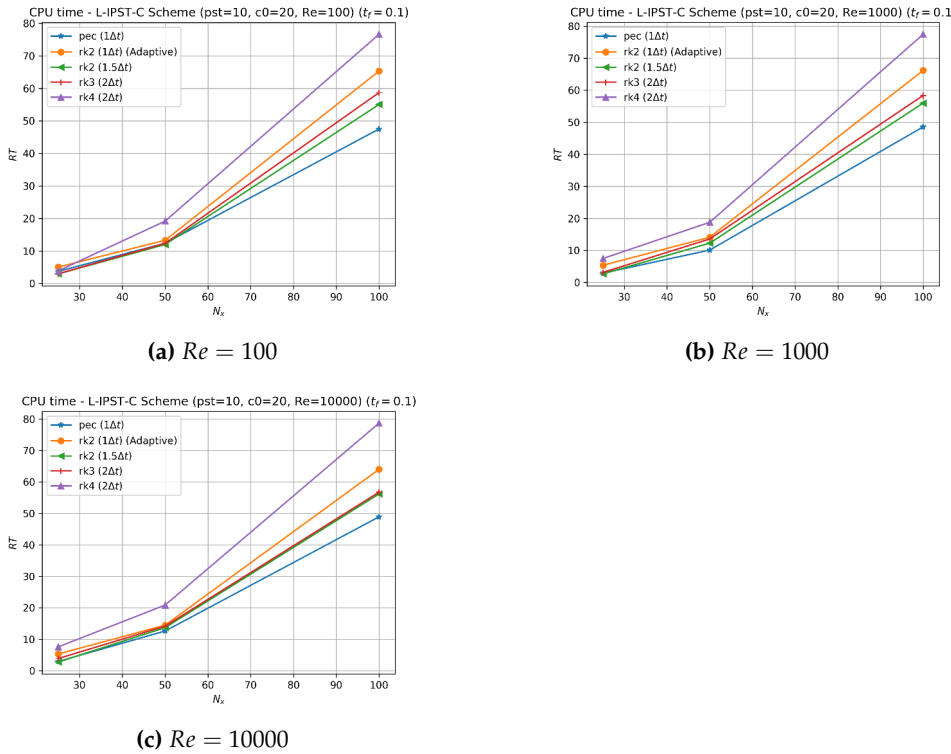


Figure 4.13: Run-time (in s) of the L-IPST-C scheme for various time-integrators.

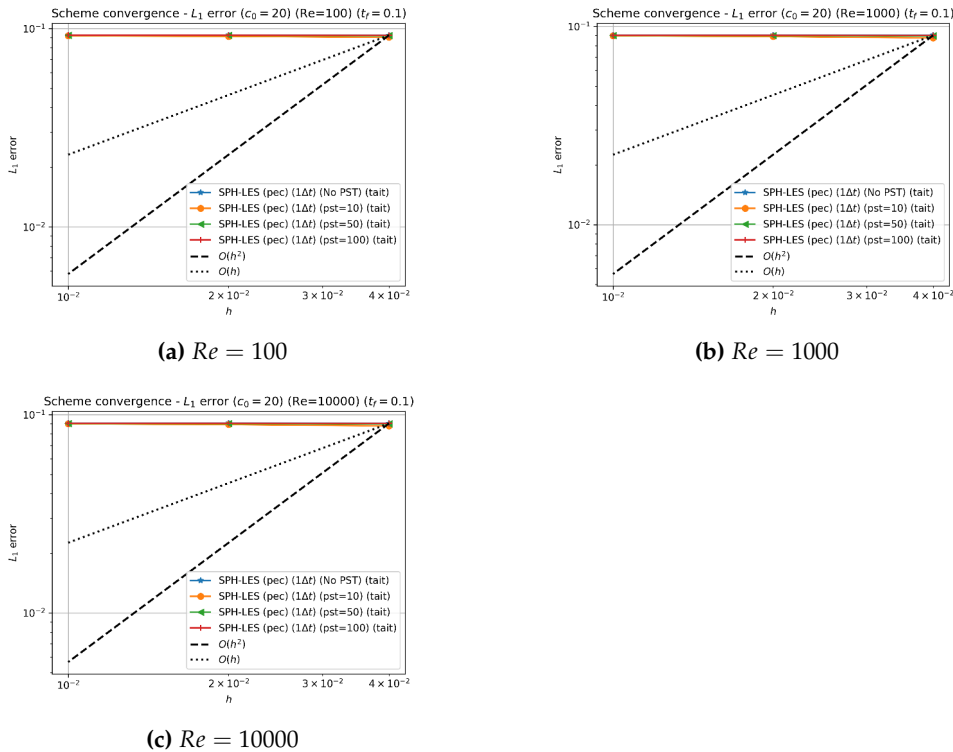


Figure 4.14: Convergence of the SPH-LES scheme for various f_{pst} values.

increases with increasing values of f_{pst} , which is indicative of the fact that the energy is being concentrated at the higher resolution scales, which is expected for the high Re case. Therefore, $f_{pst} = 10$ is chosen as the default value for the PST.

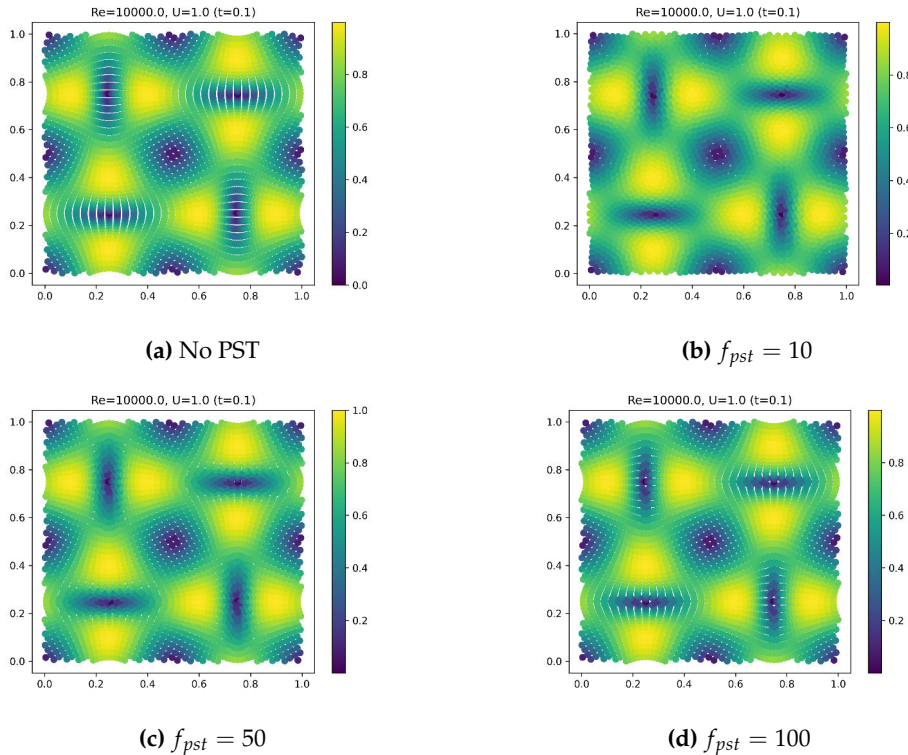


Figure 4.15: Velocity magnitude field for the SPH-LES scheme for various f_{pst} values ($N = 50^2$, $t_f = 0.1$, $Re = 10000$, $c_s = 20$).

In order to test the effect of the speed of sound on the scheme, the following values were considered: $c_s = [20, 40, 60]$. The results are shown in Fig. 4.17, where it can again be seen that the scheme is zero order convergent, irrespective of the value of c_s . In Fig. 4.18, it can be observed that the higher c_s values, which lead to smaller Δt values, lead to a more uniformly distributed group of particles, while also leading to an increased $|v|_{max}$ value. This seems to add credence to the fact that increasing the resolution in the time domain is dumping additional energy into the system as noise. This is also reflected in the energy spectrum shown in Fig. 4.19, where it can be observed that the slope of the energy spectrum increases with increasing values of c_s . Therefore, a value of $c_s = 20$ is chosen as the default value for the speed of sound, with the caveat that this scheme possibly cannot be used for problems of lower Re at all since they require dissipation of energy, which does not appear to be the case for this scheme.

Hence, the SPH-LES scheme is unsuitable for problems of low Re due to the lack of energy dissipation and zero-order convergence. For the cases of high Re , the scheme would require much more testing for each specific problem before the computed flow field can be considered accurate. This is reflected in the velocity magnitude plots shown in Fig. 4.15 and Fig. 4.18, where the flow field at the final time instance, is not the expected TGV profile, and instead distorted vortex structures are observed.

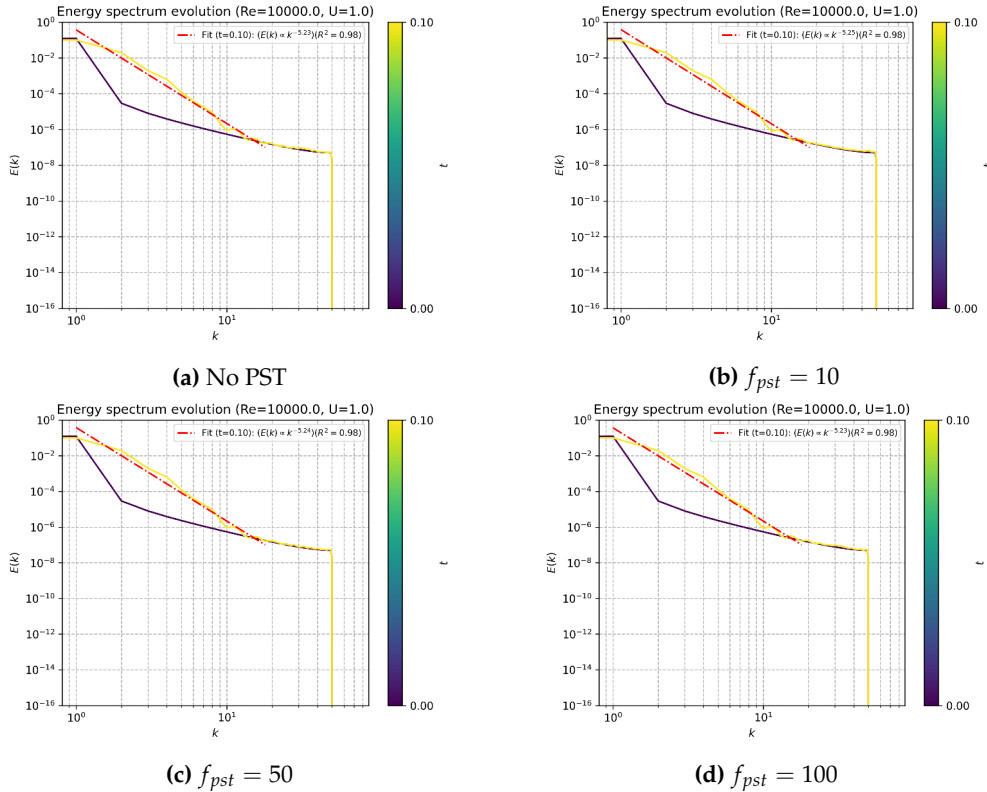


Figure 4.16: Evolution of the energy spectrum for the SPH-LES scheme for various f_{pst} values ($N = 100^2$, $t_f = 0.1$, $Re = 10000$, $c_s = 20$). The initial energy spectrum is plotted in dark blue, and the final energy spectrum is plotted in yellow.

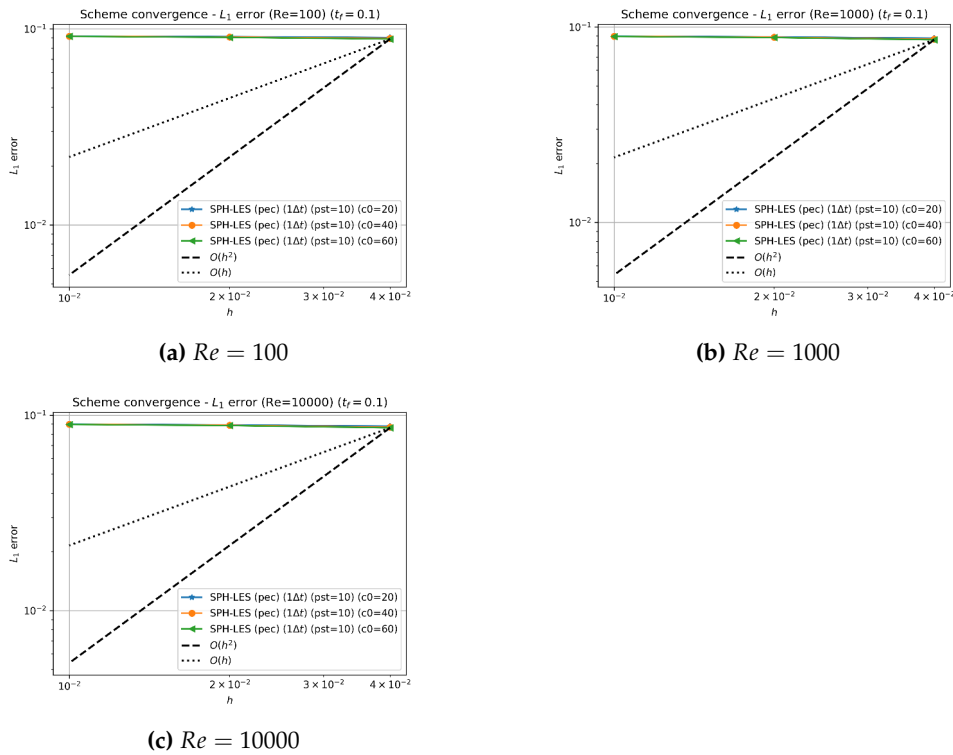


Figure 4.17: Convergence of the SPH-LES scheme for various speed of sound values.

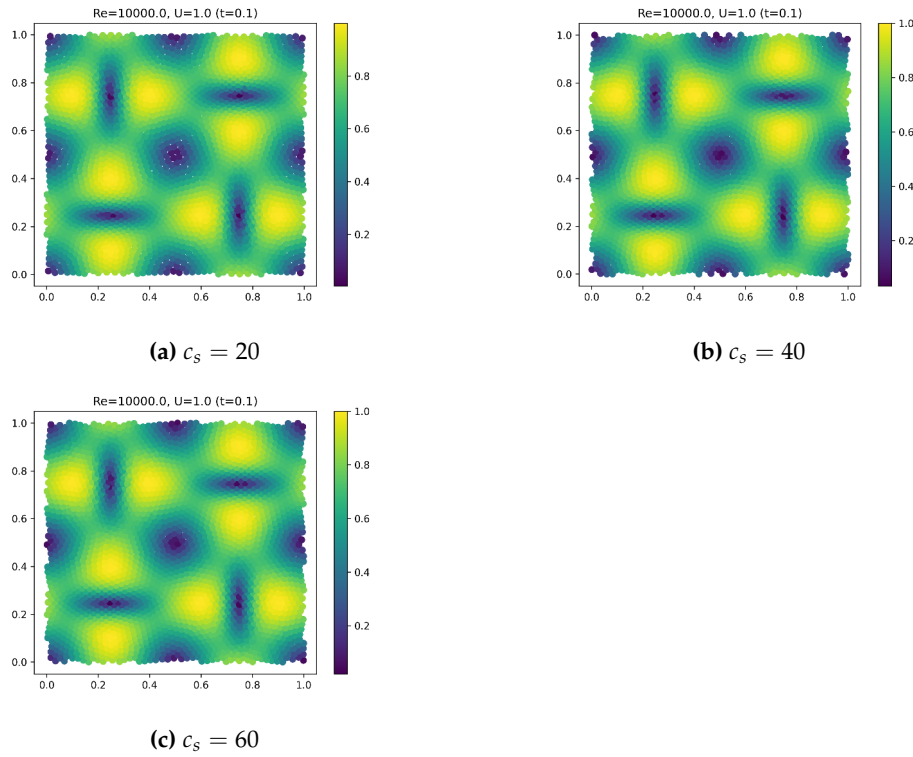


Figure 4.18: Velocity magnitude field for the SPH-LES scheme for various speed of sound values ($N = 50^2, t_f = 0.1, Re = 10000, f_{pst} = 10$).

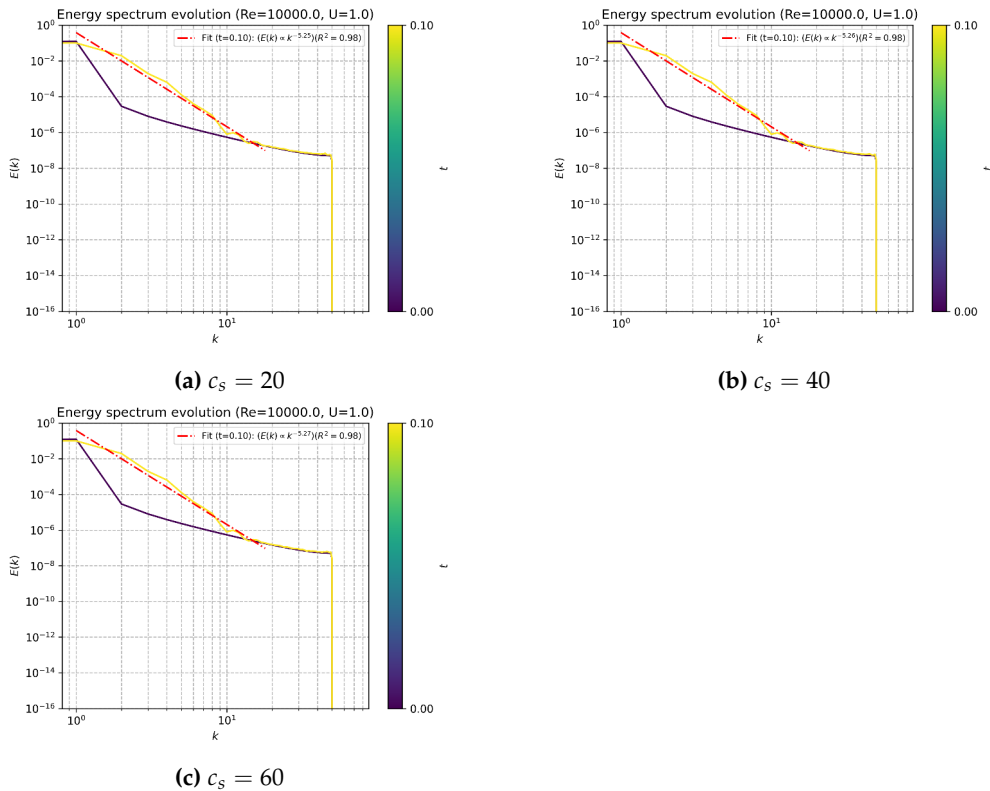


Figure 4.19: Evolution of the energy spectrum for the SPH-LES scheme for various speed of sound values ($N = 100^2, t_f = 0.1, Re = 10000, f_{pst} = 10$).

4.2.4 δ -LES-SPH Scheme

The Lagrangian LES-based models have only two major schemes to offer. One is the LES-SPH scheme of Di Mascio et al. 2017, and the other is the δ -LES-SPH scheme of Antuono et al. 2021. The latter was chosen since their scheme introduced a small arbitrary velocity deviation ($\delta\tilde{\mathbf{v}}$) to the fluid particles, which allowed for improved accuracy in simulations of high Reynolds number problems. This scheme also included PST and tensile instability control (TIC). This allowed the scheme to tackle the issue of spurious high-frequency noise and the onset of the tensile instability and was hence chosen.

During the scheme's implementation, two choices were made regarding the treatment of the fluid density. The first choice was to note that the fluid density ρ_c is independent of the summation density ρ , and in the second choice, both were treated as the same. This was done based on the work of Negi and Prabhu Ramachandran 2022, where they observed that the former choice led to improved OOC since the ρ_c should not depend on the particle configuration and should be prescribed with an initial condition. Therefore, these two variants, i.e, δ -LES-SPH (ρ_c) and δ -LES-SPH (ρ), corresponding to the two choices respectively, were considered.

In order to test the influence of the equation of state type on the scheme, the following equations of state were considered:

- TaitEOS:

$$P_i = P_0 + \frac{\rho_0 c_0^2}{\gamma} \left(\left(\frac{\rho_i}{\rho_0} \right)^\gamma - 1 \right), \quad (4.22)$$

- LinearEOS:

$$P_i = c_0^2 (\rho_i - \rho_0). \quad (4.23)$$

The results shown in Fig. 4.20 and Fig. 4.21 highlight clearly that the δ -LES-SPH (ρ_c) implementation with the TaitEOS, clearly offers the best OOC, and hence, is chosen as the default implementation for the δ -LES-SPH scheme.

Subsequently, to test for the effects of the PST on the scheme, multiple values of f_{pst} were considered, and the results are shown in Fig. 4.22. The trends are hard to decipher here since the magnitude of the error itself is lower for high values of f_{pst} or even without PST, while the OOC is better for lower values of f_{pst} . Therefore, to better analyse these results, the velocity magnitude field and the energy spectrum are plotted in Fig. 4.23 and Fig. 4.24 respectively. Here, it can be observed from the velocity magnitude plot that PST is necessary, particularly with a low f_{pst} value, since without PST, the particles become clustered, and the flow field no longer represents the expected TGV profile. The energy spectrum plot shows that the energy distribution at the final instance has barely changed, indicating that the scheme appears conservative w.r.t energy, with or without PST. Therefore, long-term studies would be required to ascertain PST's effects on the evolution of the energy spectrum. Hence, for subsequent studies, a value of $f_{pst} = 10$ is chosen as the default value for the PST.

The original scheme of Antuono et al. 2021 used a RK4 time-integrator with a $CFL = 1.5$. Therefore, to study the effects of the time-integrator, the following schemes were considered: PEC, RK2 and RK4, with an appropriate CFL value for each scheme. The results are shown in Fig. 4.25, where it can be observed that the RK2 scheme offers the best OOC and hence, is chosen as the default time-integrator

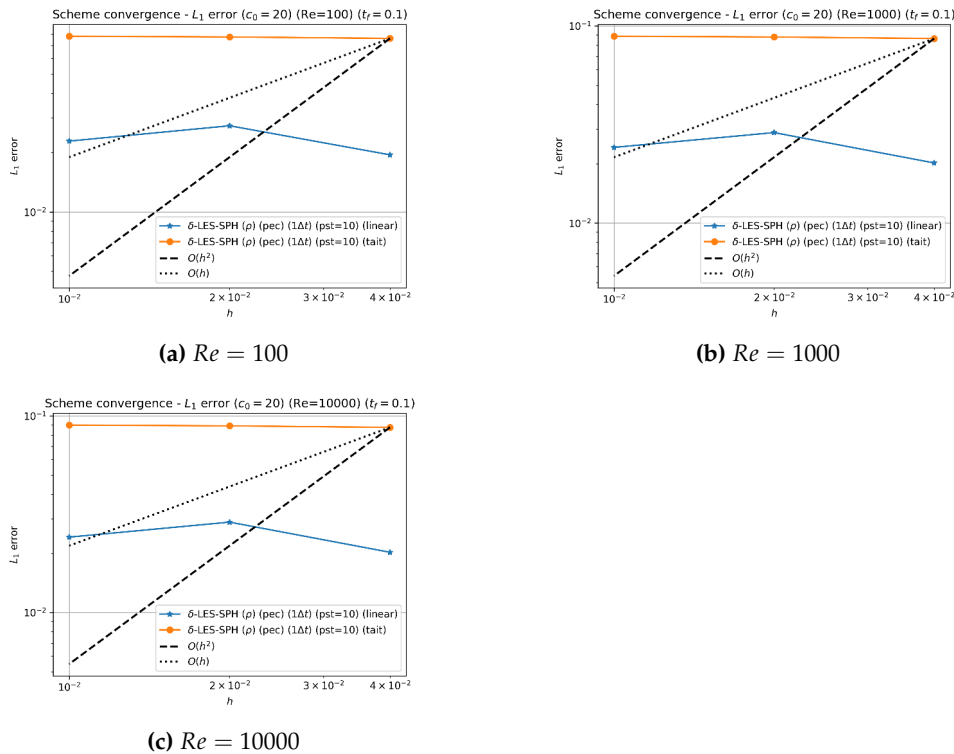


Figure 4.20: Convergence of the δ -LES-SPH (ρ) scheme for various equations of state.

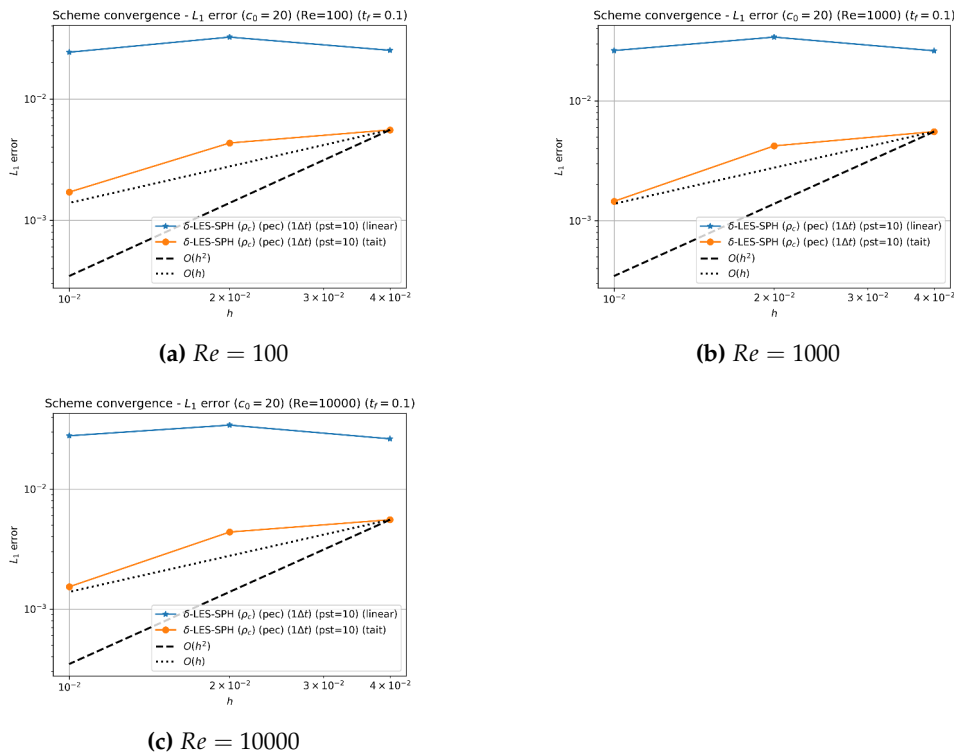


Figure 4.21: Convergence of the δ -LES-SPH (ρ_c) scheme for various equations of state.

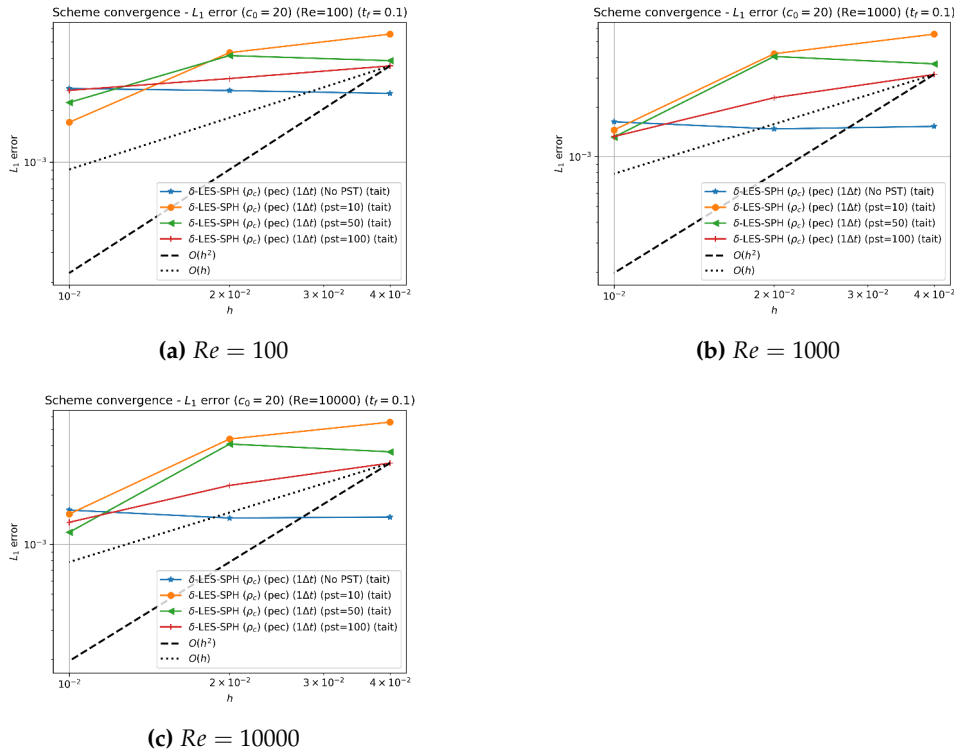


Figure 4.22: Convergence of the δ -LES-SPH (ρ_c) scheme for various f_{pst} values.

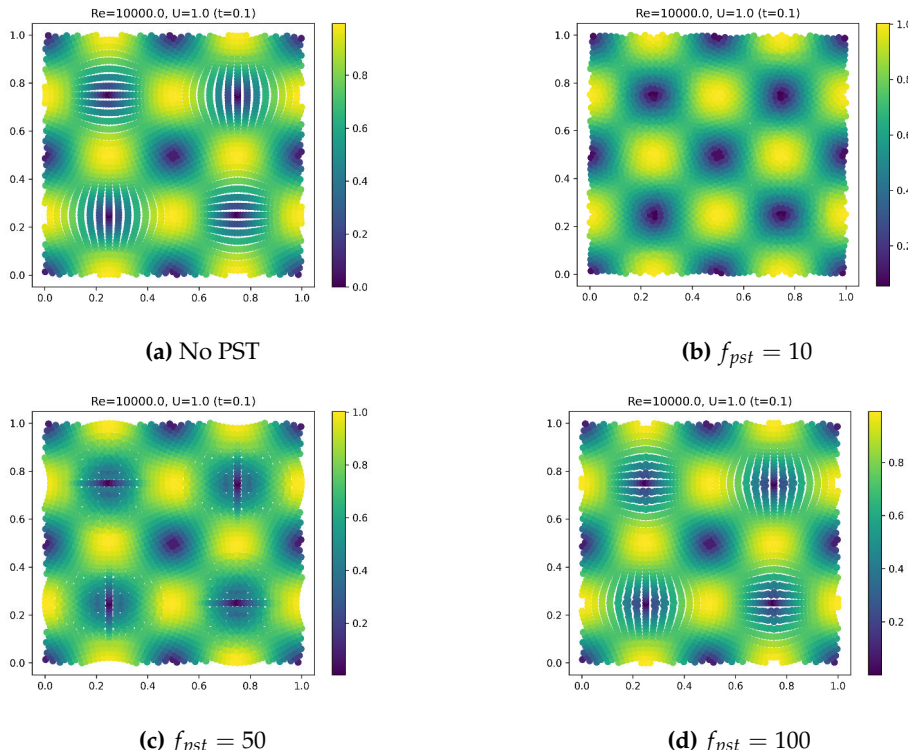


Figure 4.23: Velocity magnitude field for the δ -LES-SPH (ρ_c) scheme for various f_{pst} values ($N = 50^2$, $t_f = 0.1$, $Re = 10000$, $c_s = 20$).

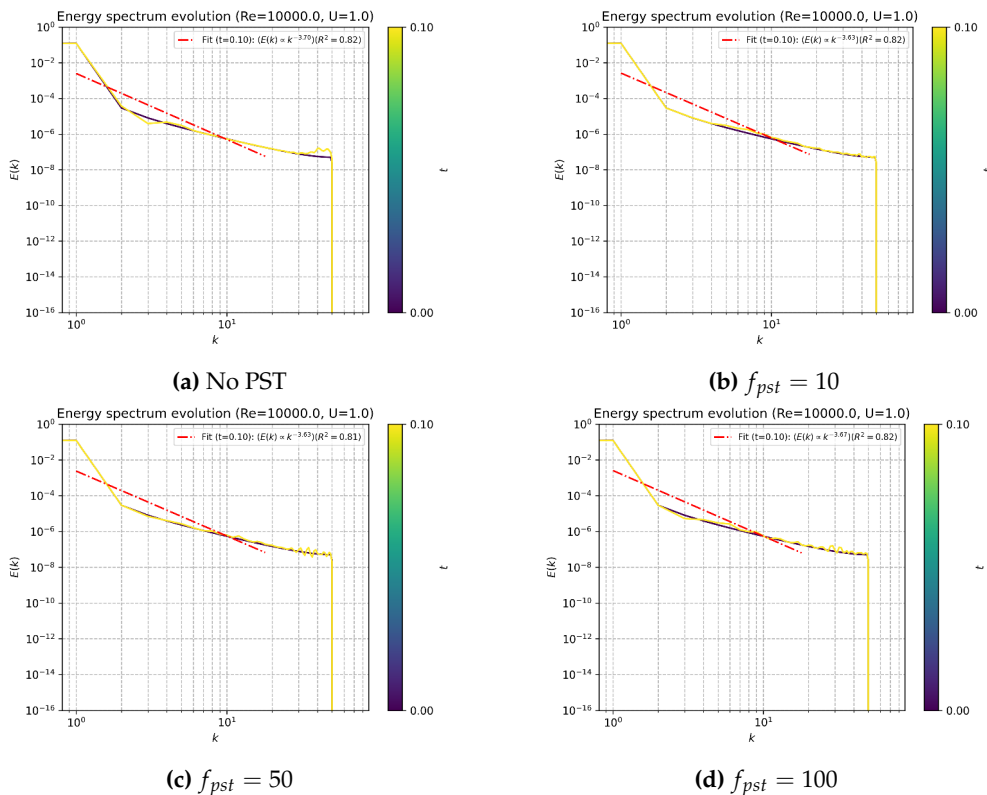


Figure 4.24: Evolution of the energy spectrum for the δ -LES-SPH (ρ_c) scheme for various f_{pst} values ($N = 100^2$, $t_f = 0.1$, $Re = 10000$, $c_s = 20$). The initial energy spectrum is plotted in dark blue, and the final energy spectrum is plotted in yellow.

for the δ -LES-SPH scheme. It is also to be noted that the RK2 integrator is also the fastest, as shown in Fig. 4.26, while offering a speedup of ≈ 1.6 times over the RK4 integrator. It is also noted that there are no significant differences to be observed in the velocity magnitude field and the energy spectrum, as shown in Fig. 4.27 and Fig. 4.28 respectively, for the different time-integrators.

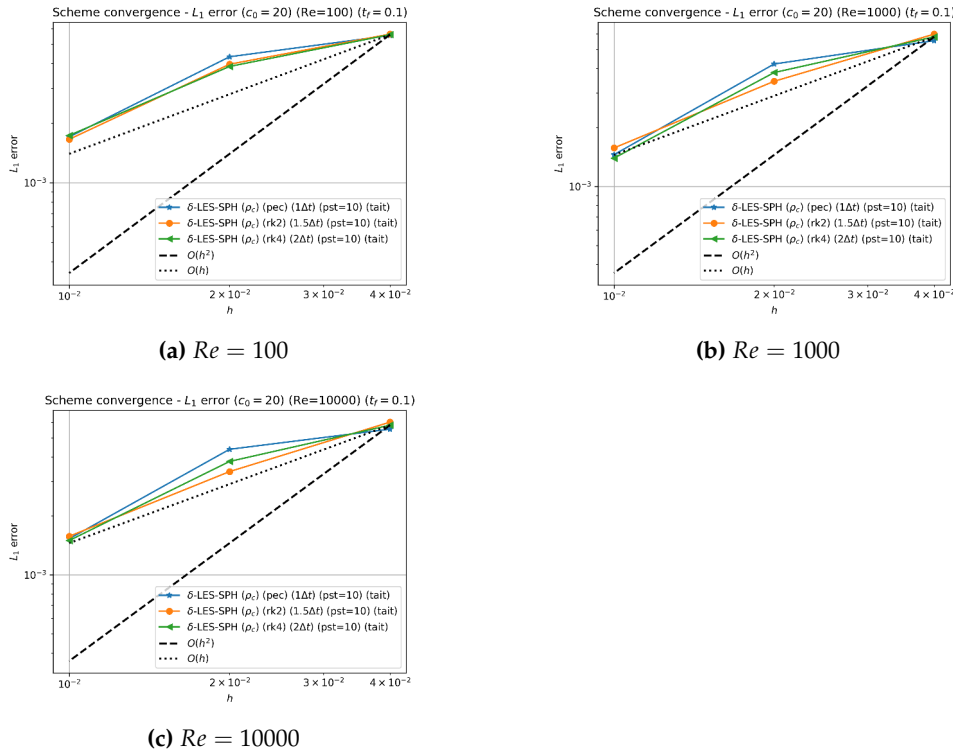


Figure 4.25: Convergence of the δ -LES-SPH (ρ_c) scheme for various time-integrators.

4.2.5 $k - \epsilon$ SPH Scheme

The $k - \epsilon$ SPH scheme of Songdong Shao 2006 was chosen over the other RANS-based schemes since the authors considered the typical RANS-based $k - \epsilon$ equations, as the governing equations for their scheme, with an implicit pressure Poisson equation that needed to be solved for the time integration of the scheme. However, it was decided that since such an implicit pressure Poisson equation solver would be computationally expensive, as well as complicated to general to other problems, the scheme was implemented with a different SPH discretisation of the $k - \epsilon$ transport equations to avoid that step.

Therefore, two choices were available when discretising the $k - \epsilon$ transport equations. The first would involve discretising the original $k - \epsilon$ equations as detailed below:

$$\frac{Dk}{Dt} = \nabla \cdot \left(\frac{\nu_t}{\sigma_k} \nabla k \right) + P_k - \epsilon, \quad (4.24)$$

$$\frac{D\epsilon}{Dt} = \nabla \cdot \left(\frac{\nu_t}{\sigma_\epsilon} \nabla \epsilon \right) + c_{1\epsilon} \frac{\epsilon}{k} P_k - c_{2\epsilon} \frac{\epsilon^2}{k}. \quad (4.25)$$

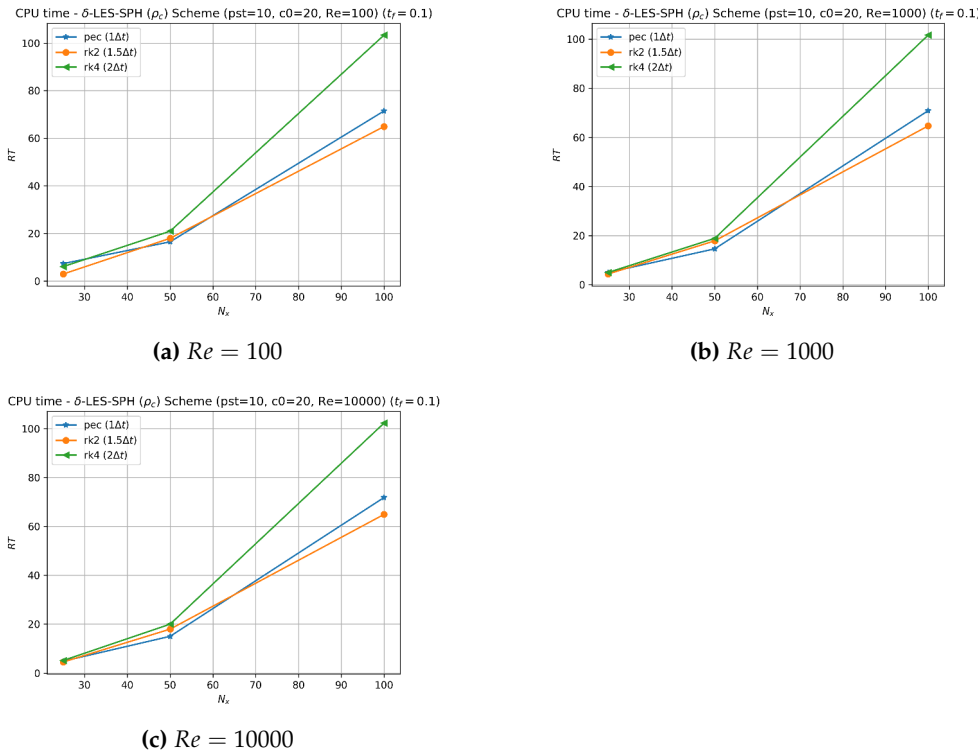


Figure 4.26: Run-time (in s) of the δ -LES-SPH (ρ_c) scheme for various time-integrators.

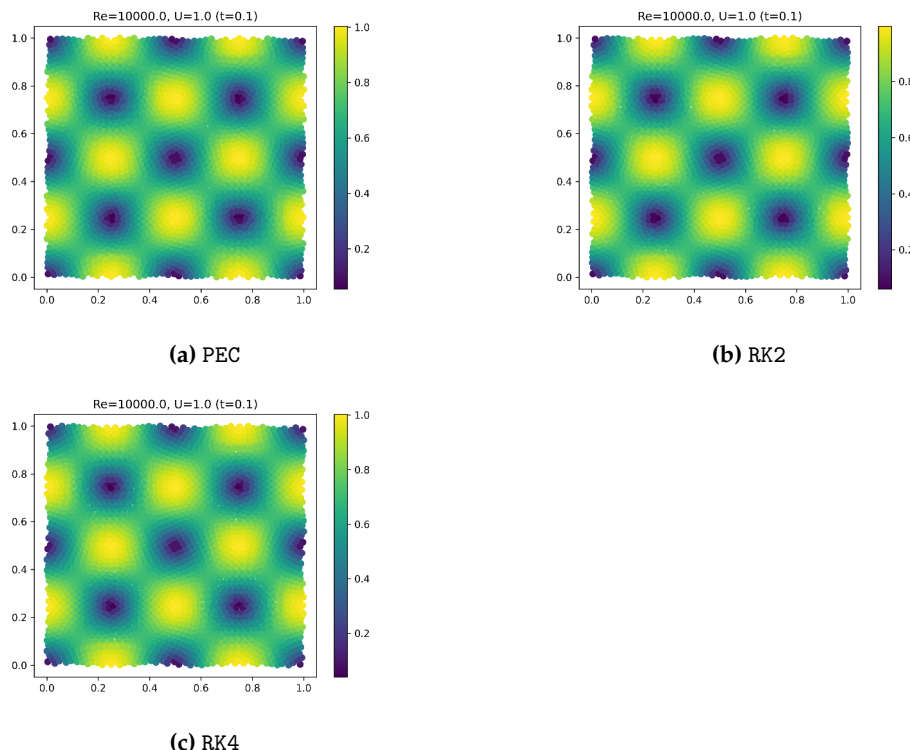


Figure 4.27: Velocity magnitude field for the δ -LES-SPH (ρ_c) scheme for various time-integrators ($N = 50^2$, $t_f = 0.1$, $Re = 10000$, $c_s = 20$, $f_{pst} = 10$).

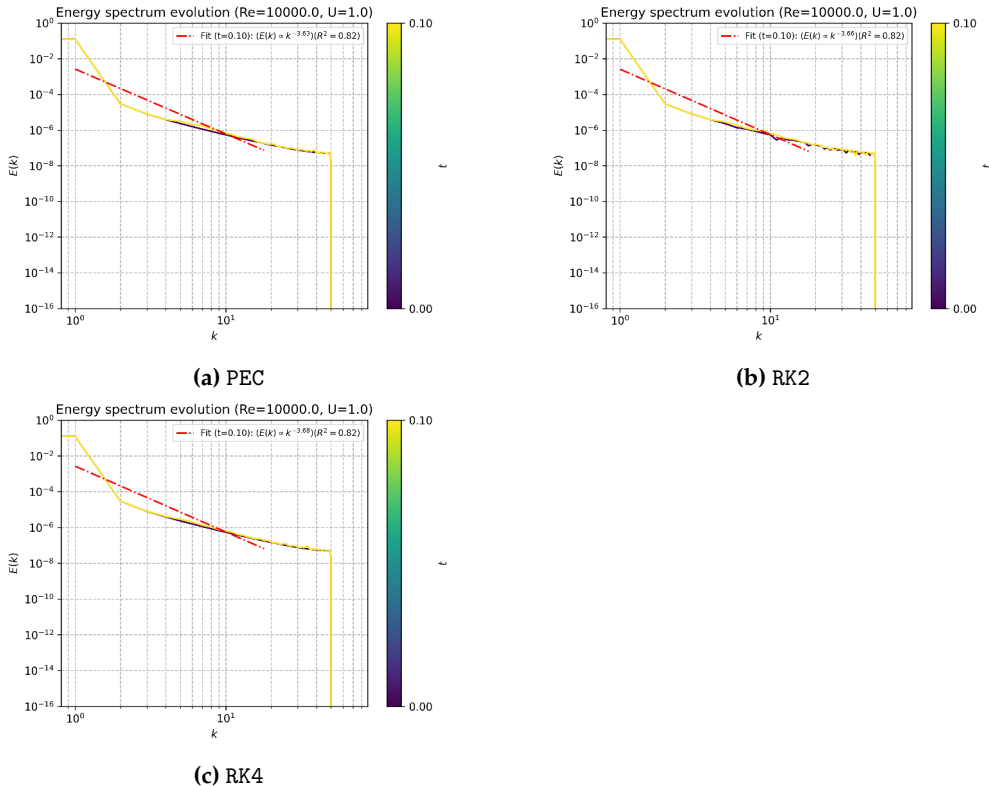


Figure 4.28: Evolution of the energy spectrum for the δ -LES-SPH (ρ_c) scheme for various time-integrators ($N = 100^2, t_f = 0.1, Re = 10000, c_s = 20, f_{pst} = 10$).

Alternatively, the above equations can also be expanded, using standard identities from calculus and substituting for the turbulent eddy viscosity ν_t to obtain:

$$\frac{Dk}{Dt} = \frac{c_d}{\sigma_k} \left(\frac{k^2}{\epsilon} \nabla^2 k + \frac{2k}{\epsilon} (\nabla k)^2 - \frac{k^2}{\epsilon^2} \nabla k \cdot \nabla \epsilon \right) + P_k - \epsilon, \quad (4.26)$$

$$\frac{D\epsilon}{Dt} = \frac{c_d}{\sigma_\epsilon} \left(\frac{k^2}{\epsilon} \nabla^2 \epsilon + \frac{2k}{\epsilon} \nabla k \cdot \nabla \epsilon - \frac{k^2}{\epsilon^2} (\nabla \epsilon)^2 \right) + c_1 \epsilon P_k - c_2 \frac{\epsilon^2}{k}. \quad (4.27)$$

Therefore, the two variants, i.e., $k - \epsilon$ simplified and $k - \epsilon$ expanded, corresponding to the two choices for the pair of transport equations are discretised using SOC SPH operators as detailed in the work of Negi and Prabhu Ramachandran 2022. In order to verify the correctness of the SPH discretisation of the $k - \epsilon$ transport equations, in either case, and study the OOC of the transport equations, a single time-step of the scheme was run on a predetermined set of initial conditions for the flow properties, including k and ϵ . The computed RHS of the k and ϵ transport equations were then compared with the analytical RHS of the equations, and the appropriate L_1 error was computed and plotted for various resolutions. This test was designed based on the more complex work done by Negi and Prabhu Ramachandran 2021, which involved the comprehensive testing of the OOC of an SPH scheme through the method of manufactured solutions (MMS) in a robust and efficient manner.

Three test cases were devised to represent three distinct functional forms. Flow properties such as the velocity, pressure and density were modelled after the initial conditions of the 2D TGV problem, as detailed in Sec. 3.1.1. In contrast, the

initial conditions for k and ϵ fields were defined as follows:

- Test-case 1:

$$k_0 = 1.5U^2, \quad \epsilon_0 = 0.09^{0.75} \frac{k_0^{1.5}}{L}, \quad (4.28)$$

where U and L are the characteristic velocity and length scales. This test case represents a constant and uniform initial condition for the $k - \epsilon$ fields.

- Test-case 2:

$$k_0 = |\mathbf{v}_0|^2, \quad \epsilon_0 = k_0, \quad (4.29)$$

where \mathbf{v}_0 is the initial velocity field. This test case represents a $k - \epsilon$ field proportional to the velocity field.

- Test-case 3:

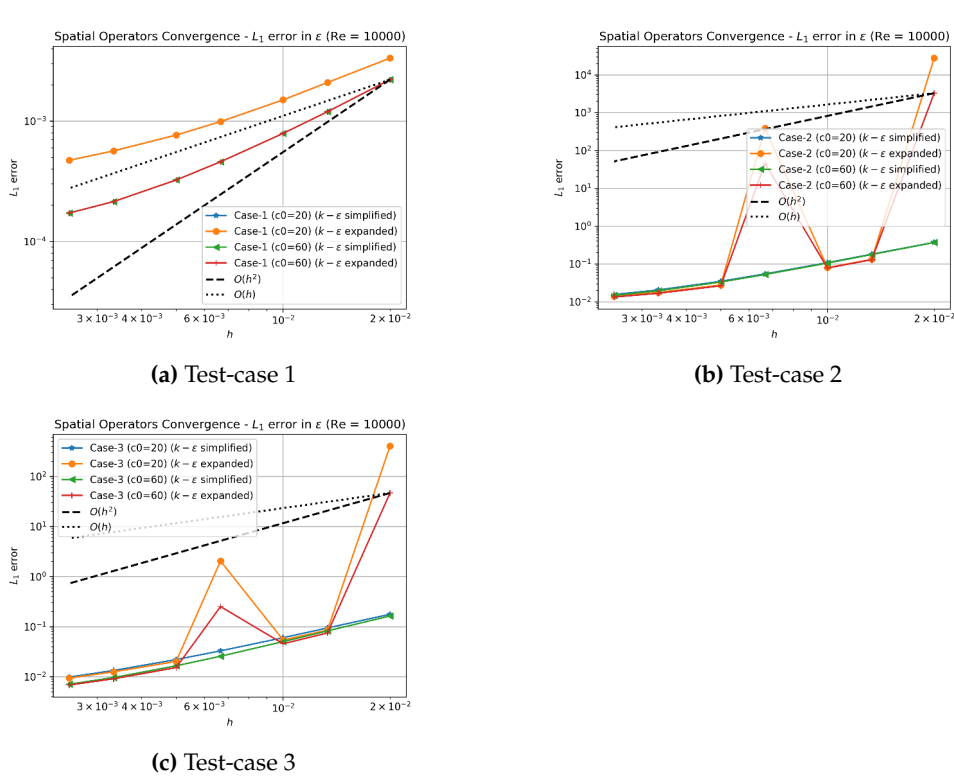
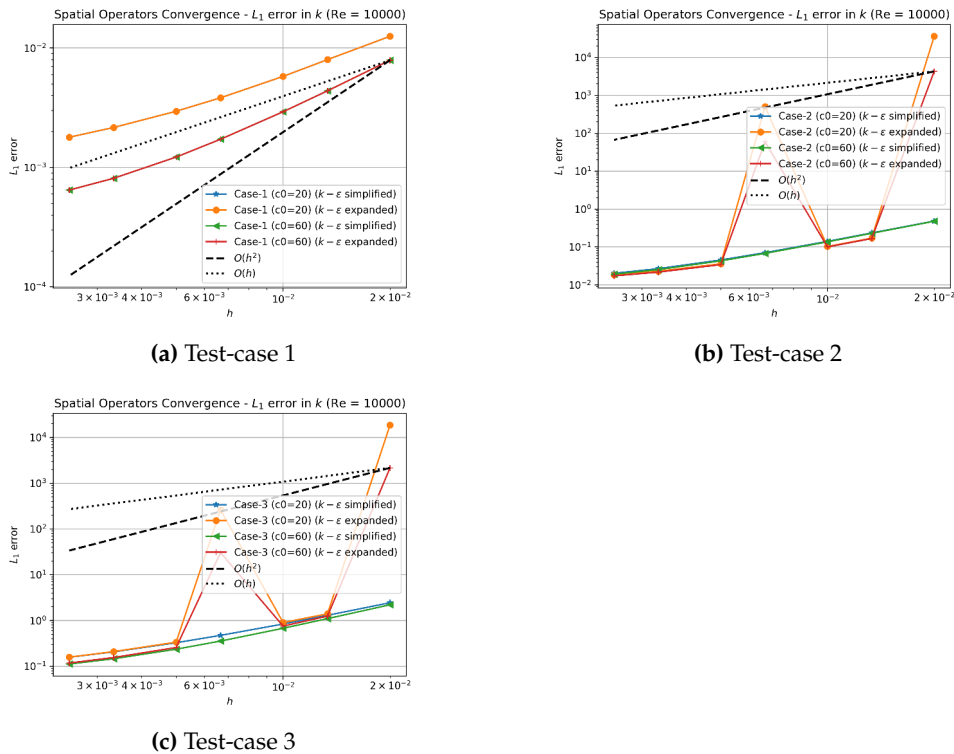
$$k_0 = \frac{1}{2} |\mathbf{v}_0|^2, \quad \epsilon_0 = 0.09 \frac{k_0^{3/2}}{L}, \quad (4.30)$$

this test case represents a $k - \epsilon$ field that is non-linearly proportional to the velocity field.

For all of the above cases, the analytical values of the RHS of the k and ϵ transport equations are computed using SymPy (Meurer et al. 2017), a symbolic package in order to automate the process and avoid any errors in the analytical computation.

The results for the k and ϵ transport equations are shown in Fig. 4.29 and Fig. 4.30 respectively. It can be observed here that for the first test case, the OOC for the spatial operators in the transport equation agrees well, irrespective of the variant of discretisation. However, the $k - \epsilon$ simplified variant in the subsequent test cases shows a better OOC than the $k - \epsilon$ expanded variant. This can be attributed to the fact that in the expanded equations of (4.26) and (4.27), the terms involve either higher-order derivatives or products of derivatives, which are not well approximated by the SPH operators, and hence, lead to increased errors. It appears that the advantage of dealing with single-term derivatives (e.g., ∇k) in the expanded equations, compared to having multi-term derivatives (e.g., $\nabla \cdot (k^2 \nabla k / \epsilon)$) in the simplified equations, is not enough to offset the increased numerical errors due to the higher-order derivatives. This is also made more evident in the actual $k - \epsilon$ fields, as shown in Fig. 4.31 and Fig. 4.32, respectively, where the significant error caused by the $k - \epsilon$ expanded variant is visible. This is also corroborated by the fact that the expanded variant shows sudden and massive spikes in the OOC plot of Fig. 4.30 for specific resolutions, which are not observed in the simplified variant. This would indicate that the expanded variant is sensitive to the resolution of the problem and hence, is unsuitable for general use. Therefore, the $k - \epsilon$ simplified variant is chosen as the default variant for the $k - \epsilon$ SPH scheme.

In order to study the effects of the various equations of state on the, the convergence study was performed on the $k - \epsilon$ SPH scheme, involving the SPH discretisation of simplified $k - \epsilon$ transport equations, and the PEC time-integrator. The results are shown in Fig. 4.33, where it can be observed that both the LinearEOS and TaitEOS appear to offer zeroth-order convergence. To gain further insight, Fig. 4.34 and Fig. 4.35 are referred to, where it can be observed that the velocity field computed using the TaitEOS appears to better correspond to the typical TGV profile. The energy spectrum is interesting because the LinearEOS appears to redistribute energy from the larger to smaller scales. In contrast, the TaitEOS appears to dissipate energy in the system for all scales. Although the former behaviour is more desirable, as it



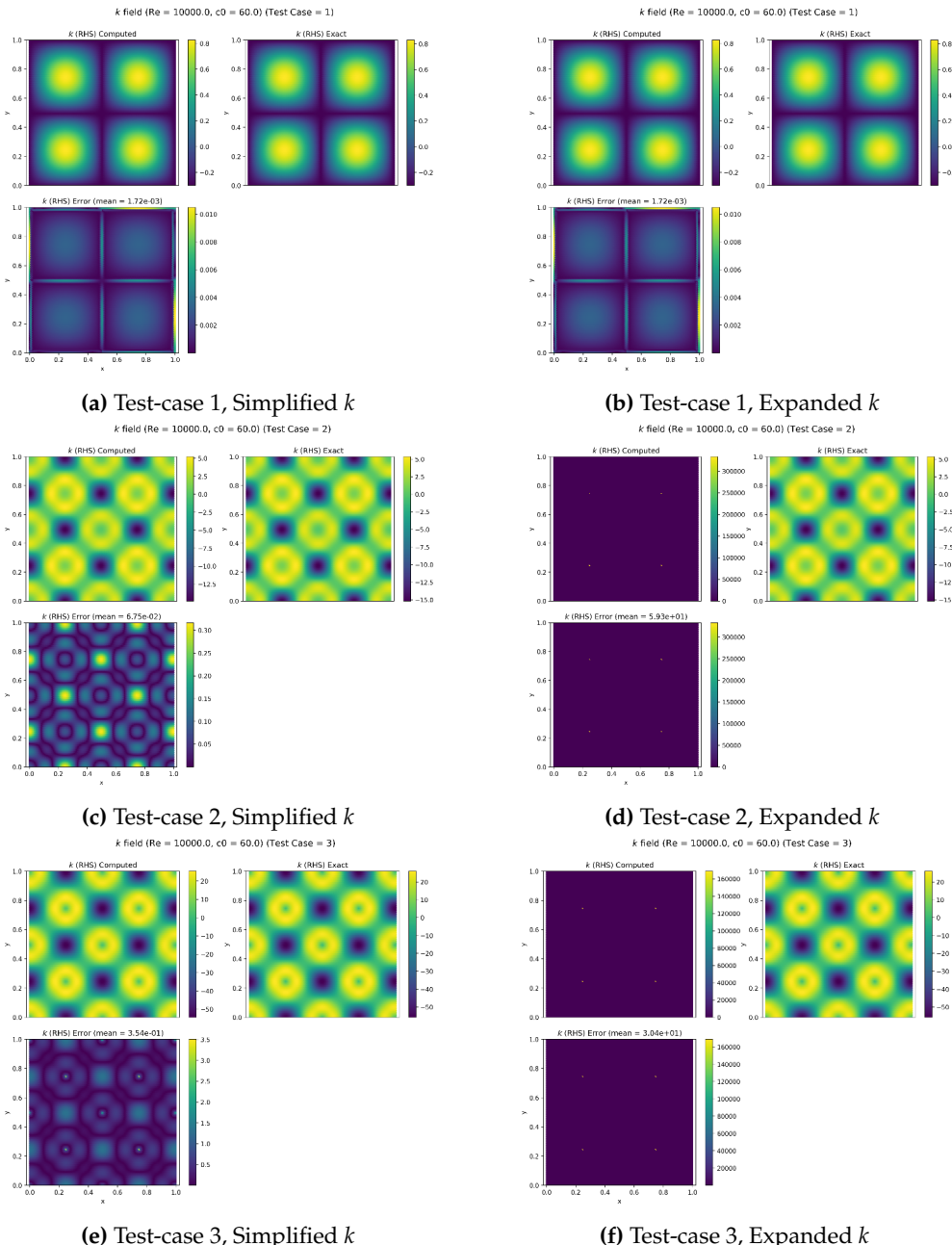


Figure 4.31: RHS of the k transport equation for various test-cases ($N = 150^2, t_f = 1\Delta t, Re = 10000, c_s = 60$).

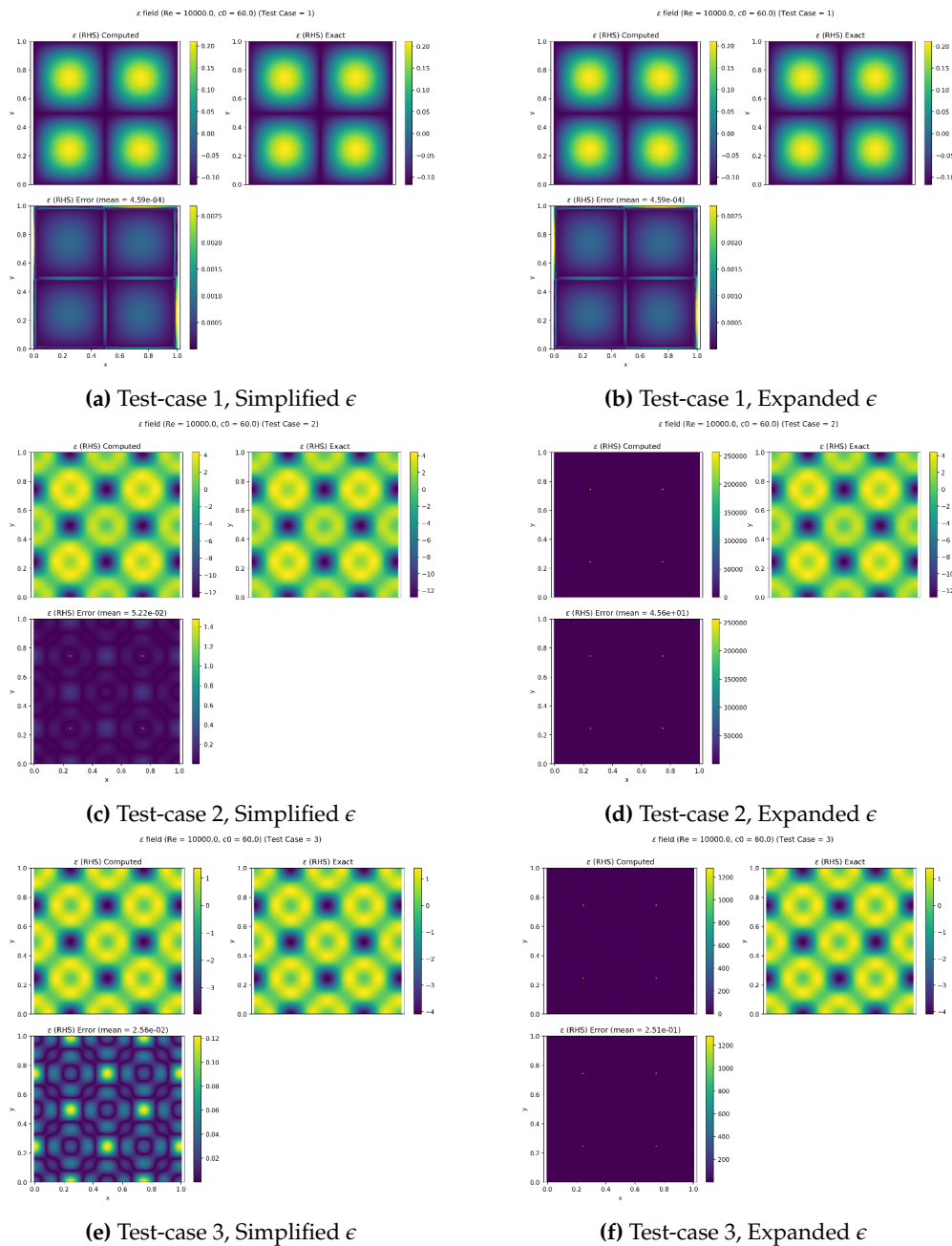


Figure 4.32: RHS of the ϵ transport equation for various test-cases ($N = 150^2, t_f = 1\Delta t, Re = 10000, c_s = 60$).

is more representative of the physical system, the actual velocity field plot for the LinearEOS scheme indicates its instability, and hence, the TaitEOS is chosen as the default equation of state for the $k - \epsilon$ SPH scheme.

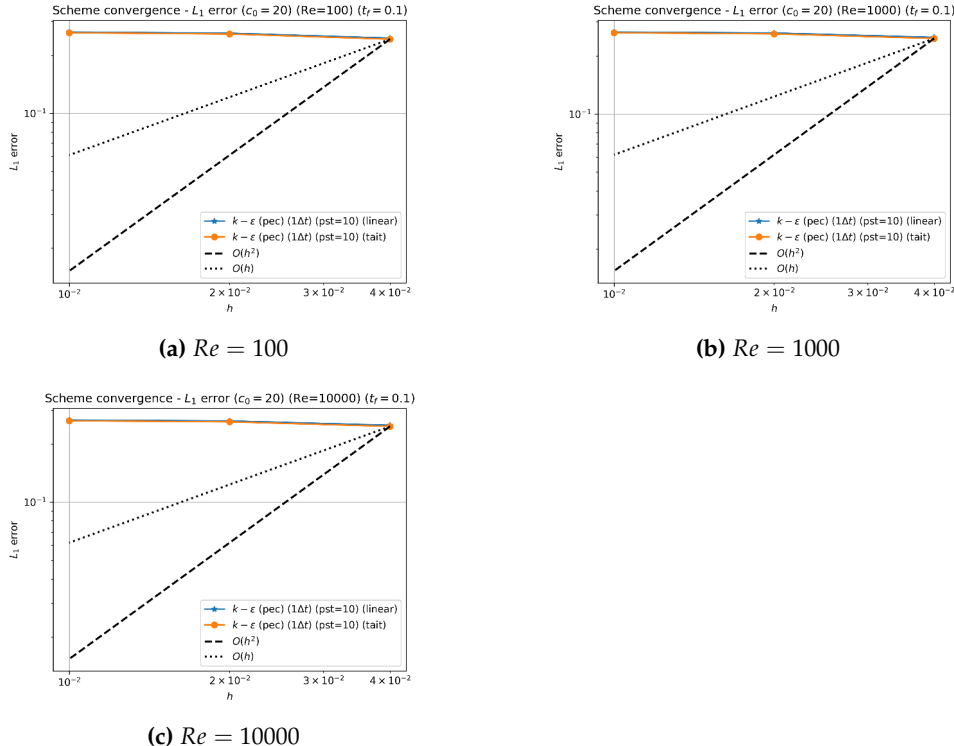


Figure 4.33: Convergence of the $k - \epsilon$ SPH scheme for various equations of state.

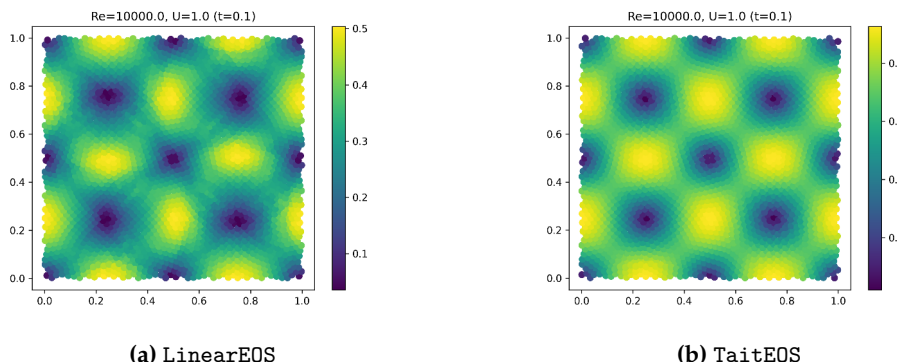


Figure 4.34: Velocity magnitude field for the $k - \epsilon$ SPH scheme for various equations of state ($N = 50^2$, $t_f = 0.1$, $Re = 10000$, $c_s = 20$, $f_{pst} = 10$).

A similar study was undertaken on the effects of f_{pst} on the $k - \epsilon$ SPH scheme. The results are shown in Fig. 4.36, where it can again be observed that the scheme appears to offer zeroth-order convergence for all values of f_{pst} . Looking into the velocity magnitude field, as shown in Fig. 4.37, similar trends are observed, in that, higher values of f_{pst} or lack of one leads to clustering of particles, and hence, the velocity field appears jagged. No other noticeable differences are observed in the energy

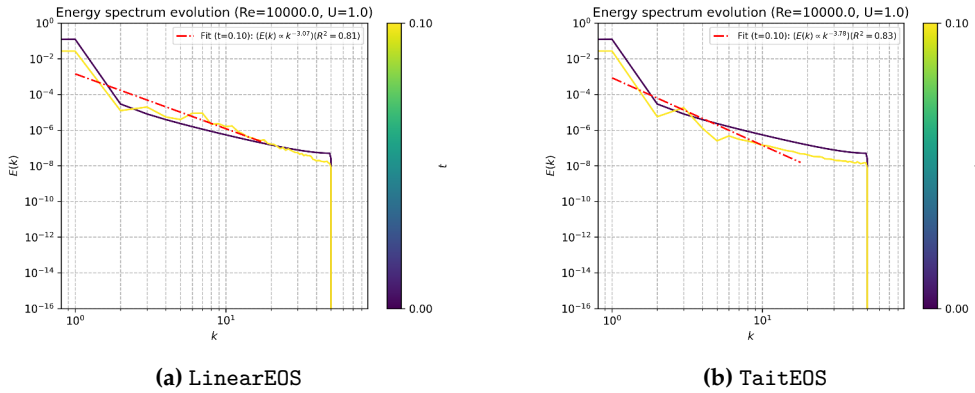


Figure 4.35: Evolution of the energy spectrum for the $k - \epsilon$ SPH scheme for various equations of state ($N = 100^2, t_f = 0.1, Re = 10000, c_s = 20, f_{pst} = 10$).

spectrum, as shown in Fig. 4.38, which seems to indicate the f_{pst} does not seem to have a substantial effect on the energy spectrum, at least for short time simulations.

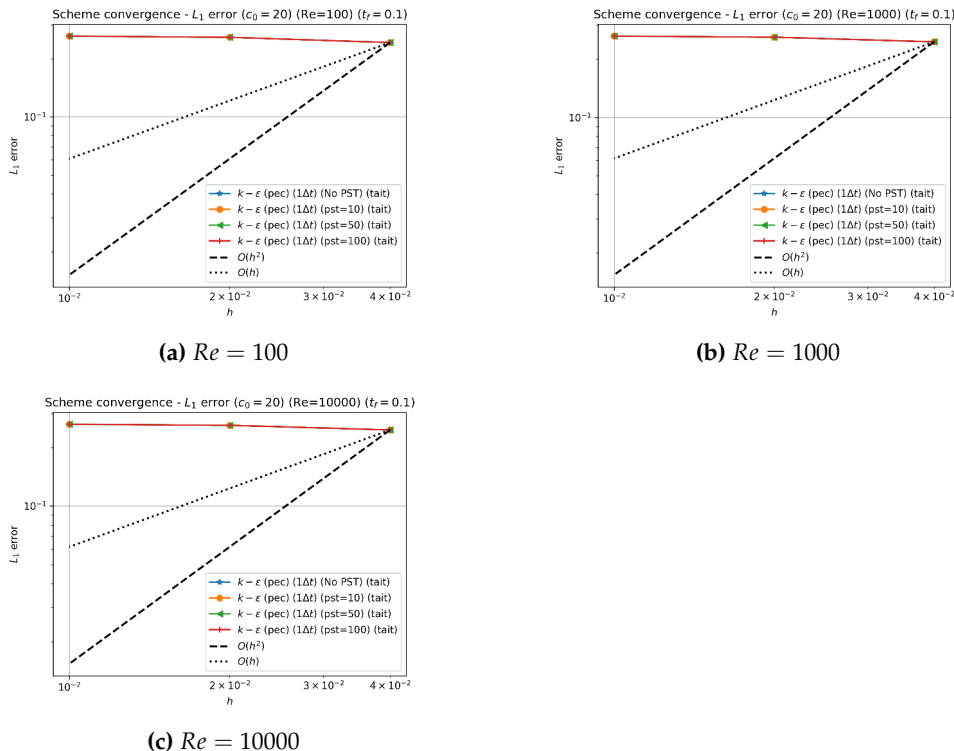


Figure 4.36: Convergence of the $k - \epsilon$ SPH scheme for various f_{pst} values.

4.2.6 SPH- ϵ Scheme

Amongst all of the LANS-based turbulence models, the SPH- ϵ scheme of J. J. Monaghan 2017 was chosen over the other schemes because of its straightforward implementation regarding the momentum equation. Unlike the governing equations in the LANS- α scheme of Mohseni et al. 2003, which involve solving for the inverse

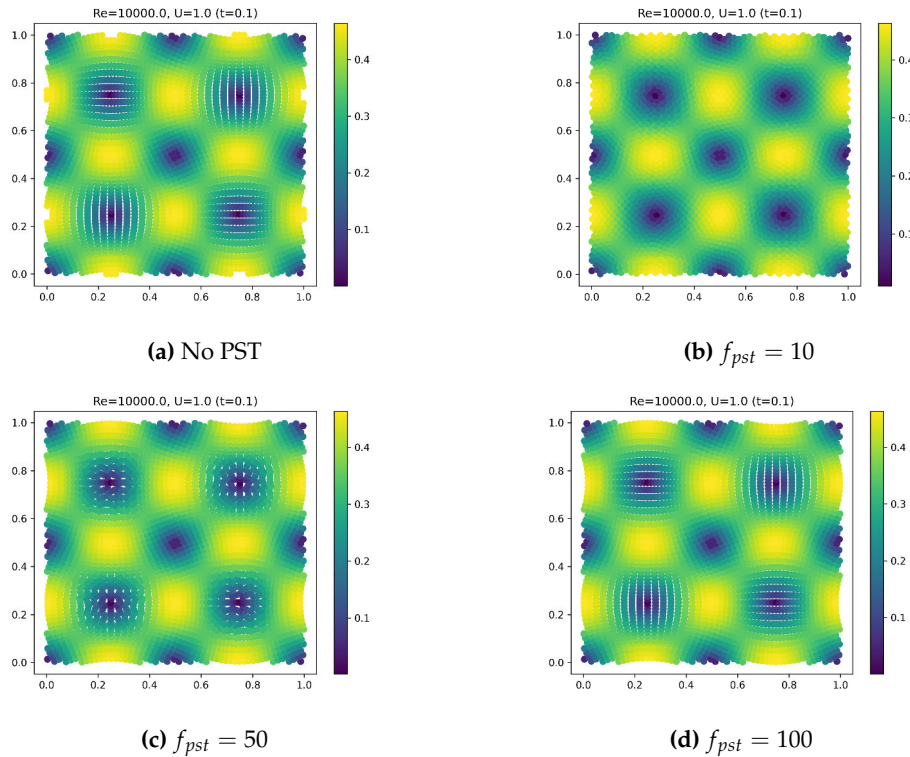


Figure 4.37: Velocity magnitude field for the $k - \epsilon$ SPH scheme for various f_{pst} values ($N = 50^2, t_f = 0.1, Re = 10000, c_s = 20$).

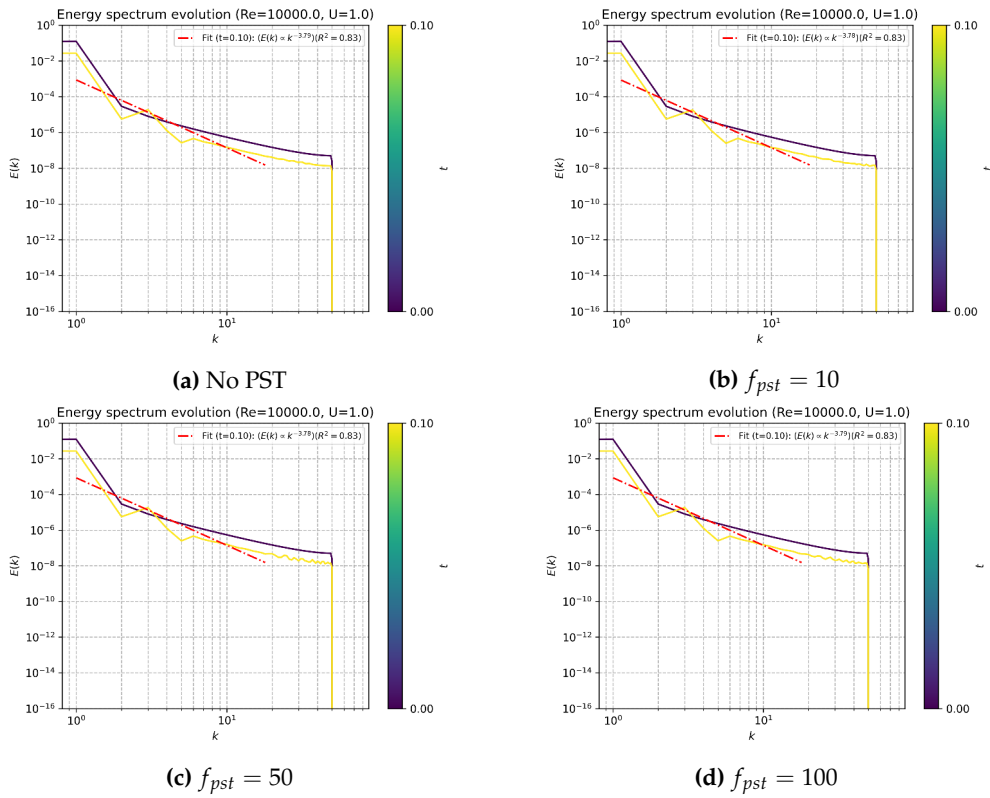


Figure 4.38: Evolution of the energy spectrum for the $k - \epsilon$ SPH scheme for various f_{pst} values ($N = 100^2, t_f = 0.1, Re = 10000, c_s = 20$).

of the Helmholtz operator (which appears in Eq. 2.113), Monaghan was able to derive a form from the Lagrangian for a compressive, non-dissipative fluid. The result was a scheme consisting of explicit terms for the transport equations, which could be easily implemented in SPH.

The scheme was not implemented with the gradient correction term in the original work, and hence, to study its potential effects, a convergence study was performed on the scheme with and without the Bonet and Lok gradient correction term. The results are shown in Fig. 4.39, where it can be observed that the gradient correction term does not appear to have a significant effect on the convergence of the scheme. The same conclusion can be drawn from the velocity magnitude field, as shown in Fig. 4.40, where the velocity field does not appear to be significantly different for the two cases. Similarly, the energy spectrum, as shown in Fig. 4.41, also does not appear to be significantly different for the two cases. Therefore, a variant without the gradient correction term is chosen as the default for the SPH- ϵ scheme.

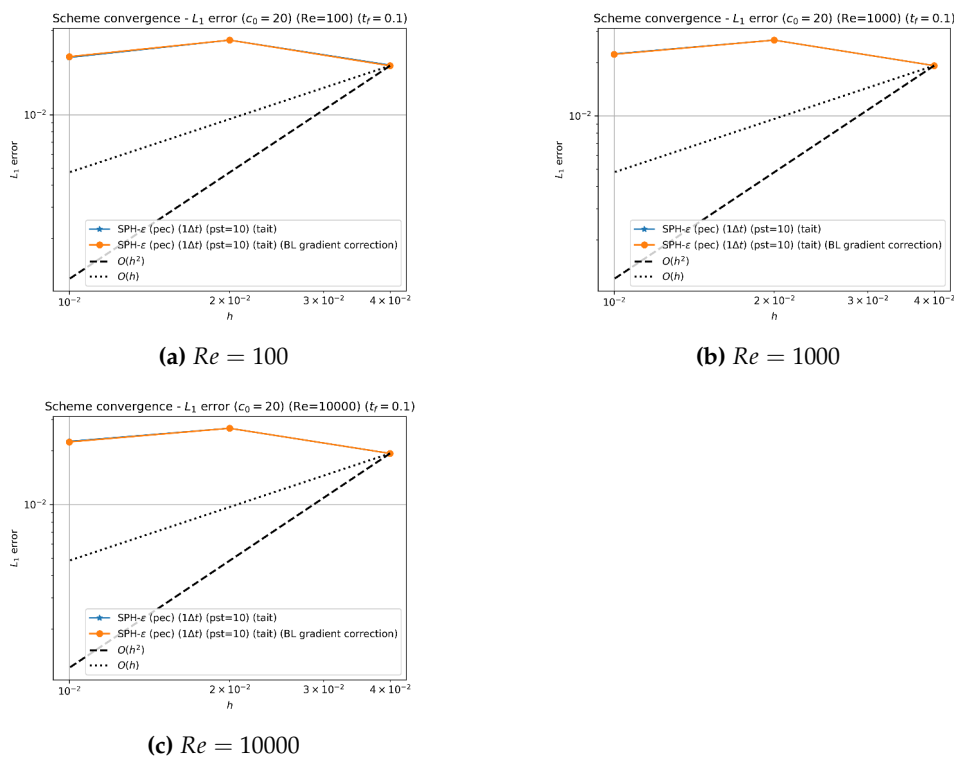


Figure 4.39: Convergence of the SPH- ϵ scheme without and with gradient correction.

Since the scheme has the smoothing parameter ϵ as a free parameter, a convergence study was performed on the scheme for various values of ϵ . The results are shown in Fig. 4.42. Firstly, it can be observed that the scheme appears to offer zeroth-order convergence for all values of ϵ , which is not surprising, as the scheme is not designed to be a high-order scheme. Secondly, the value of ϵ does not appear to have a significant effect on the convergence of the scheme, except for minor differences in the magnitude of the L_1 error, particularly for low values of Re . The velocity magnitude field, as shown in Fig. 4.43, indicates that as the ϵ value increases, the velocity field appears to be more diffused, which is expected, as the scheme is designed to be more dissipative for higher values of ϵ , but this comes at the cost of a velocity profile that is not as accurate as the lower values of ϵ . From the energy spectrum plot, as shown

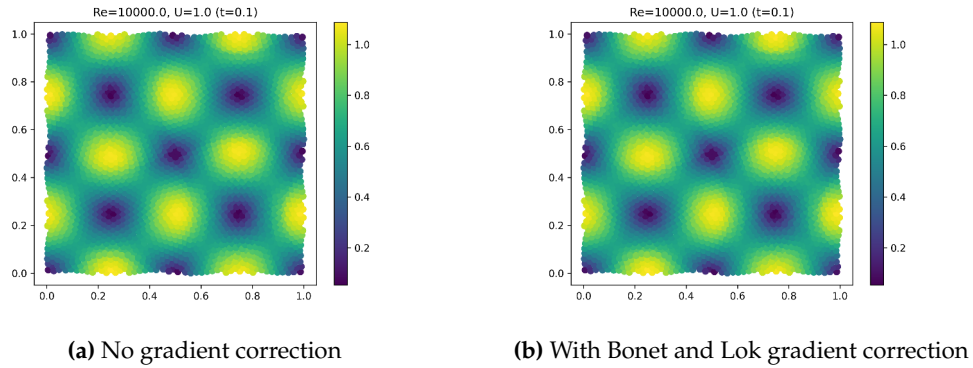


Figure 4.40: Velocity magnitude field for the SPH- ϵ scheme without and with gradient correction ($N = 50^2, t_f = 0.1, Re = 10000, c_s = 20, f_{pst} = 100$).

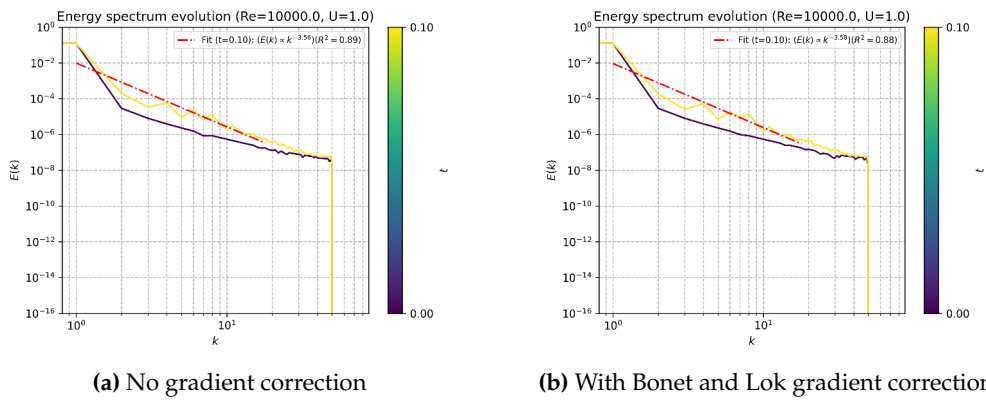


Figure 4.41: Evolution of the energy spectrum for the SPH- ϵ scheme without and with gradient correction ($N = 100^2, t_f = 0.1, Re = 10000, c_s = 20, f_{pst} = 100$).

in Fig. 4.44, it can be observed that the higher values of ϵ reduce the overall energy in the system relatively, in addition to reducing the slope of the energy spectrum, further indicating the dissipative nature of the scheme for higher values of ϵ .

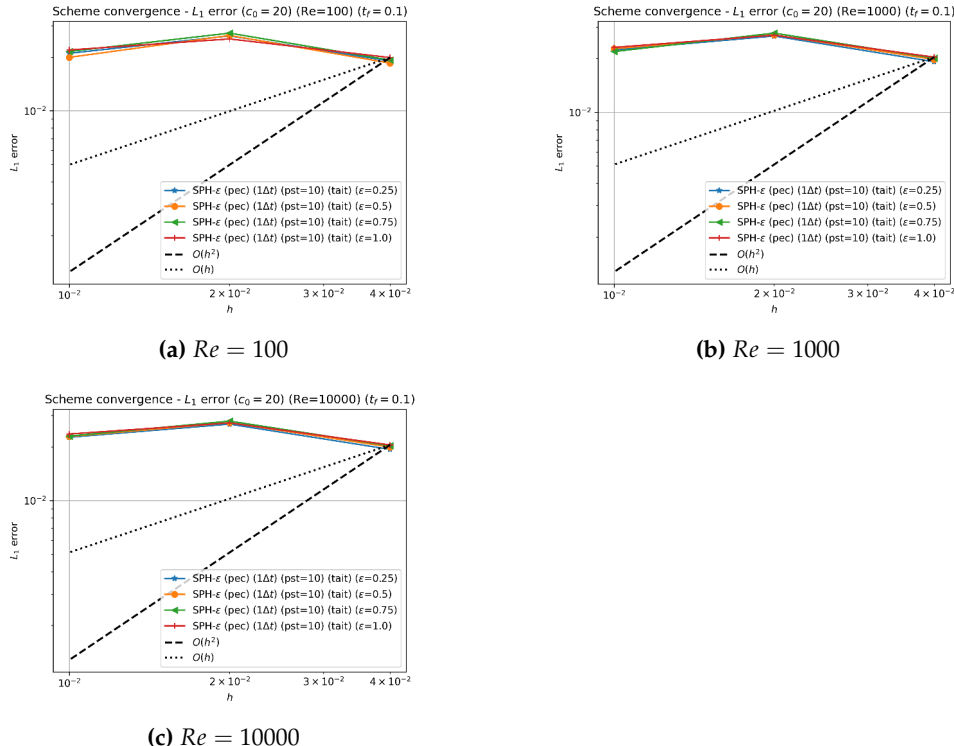


Figure 4.42: Convergence of the SPH- ϵ scheme for various values of ϵ ($N = 50^2$, $t_f = 0.1$, $Re = 10000$, $c_s = 20$, $f_{pst} = 100$).

Similarly, a convergence study was performed to study the effects of the equation of state on the SPH- ϵ scheme. The results are shown in Fig. 4.45, where it can be observed that, once again, the nature of the equation of state does not affect the convergence of the scheme. This is made evident by both the velocity magnitude field, as shown in Fig. 4.46, and the energy spectrum, as shown in Fig. 4.47, which do not appear to be significantly different for the two cases. Hence, following through with the original scheme, TaitEOS is chosen as the default equation of state for the SPH- ϵ scheme.

Finally, a convergence study was performed on the effects of f_{pst} on the SPH- ϵ scheme. From observing the results shown in Fig. 4.48, it can be concluded that though large values of f_{pst} reduce the magnitude of the L_1 error, the OOC is still zeroth-order. On the other hand, the velocity magnitude field, as shown in Fig. 4.49, indicates that higher values of f_{pst} lead to the clustering of particles. The energy spectrum, as shown in Fig. 4.50, indicates that higher values of f_{pst} , or lack of one, do not lead to much change in the energy distribution in the system. Whereas smaller values of f_{pst} appear to dump energy into the smaller scales, the larger ones remain relatively unaffected. This observation is interesting since adding energy to the system without a dissipative mechanism will potentially lead to instability at high Re . Suppose one tries to counter this with the natural dissipative mechanism of the smoothing parameter ϵ . In that case, there is a trade-off between the accuracy of the velocity field and the energy spectrum. Hence, a default value of $f_{pst} = 10$, and $\epsilon = 0.5$ is chosen for the SPH- ϵ scheme.

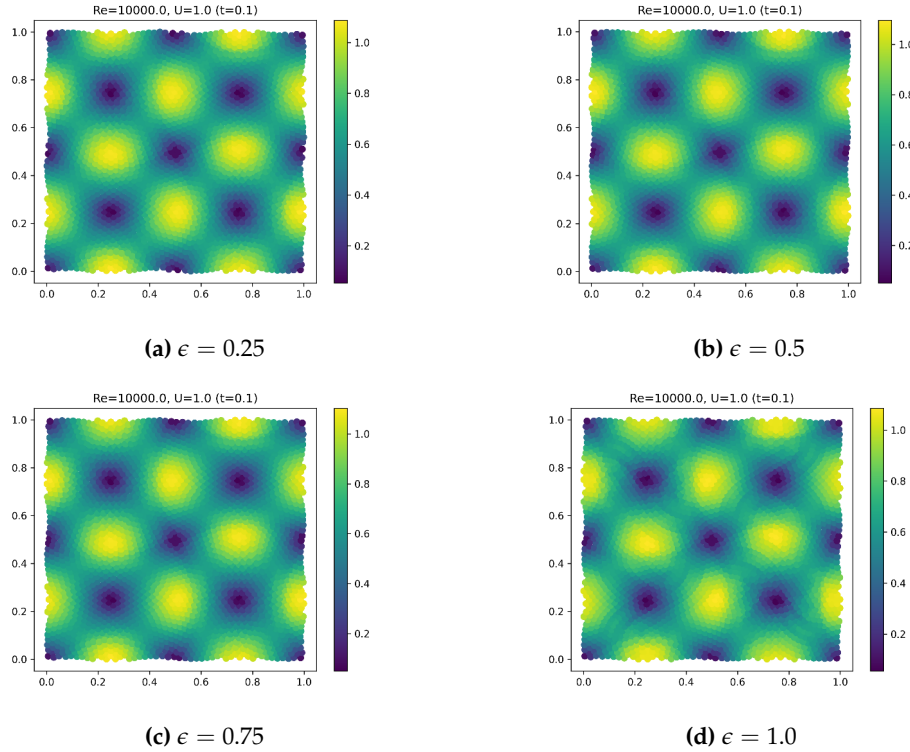


Figure 4.43: Velocity magnitude field for the SPH- ϵ scheme for various values of ϵ ($N = 50^2$, $t_f = 0.1$, $Re = 10000$, $c_s = 20$, $f_{pst} = 100$).

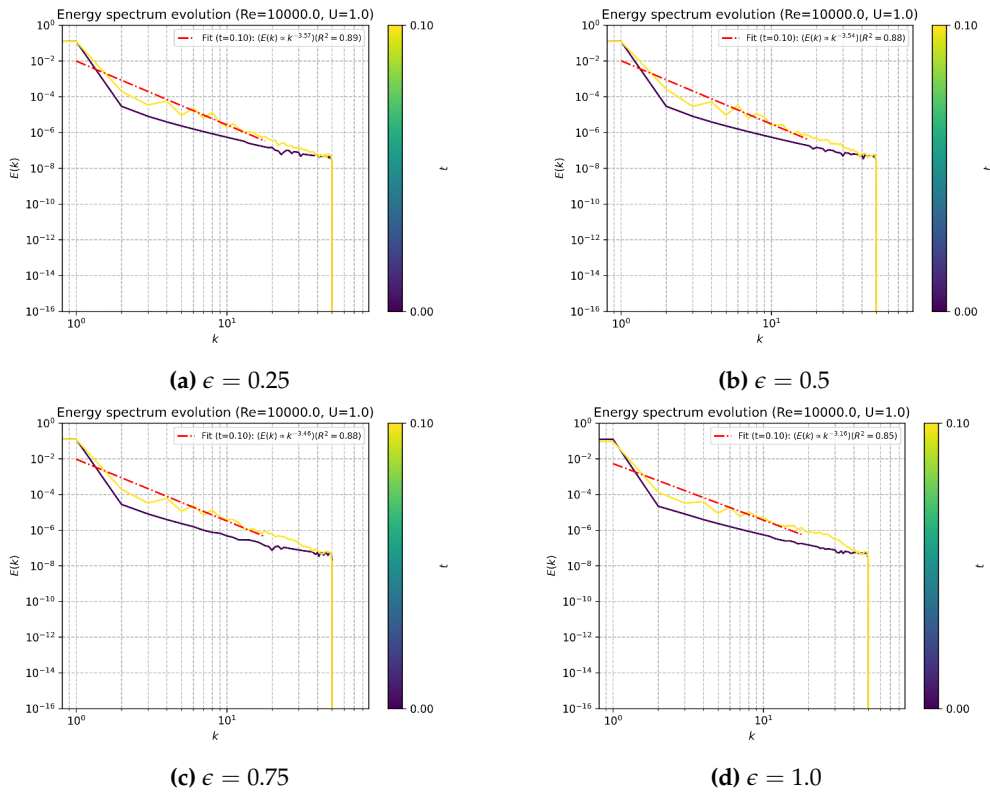


Figure 4.44: Evolution of the energy spectrum for the SPH- ϵ scheme for various values of ϵ ($N = 100^2$, $t_f = 0.1$, $Re = 10000$, $c_s = 20$, $f_{pst} = 100$).

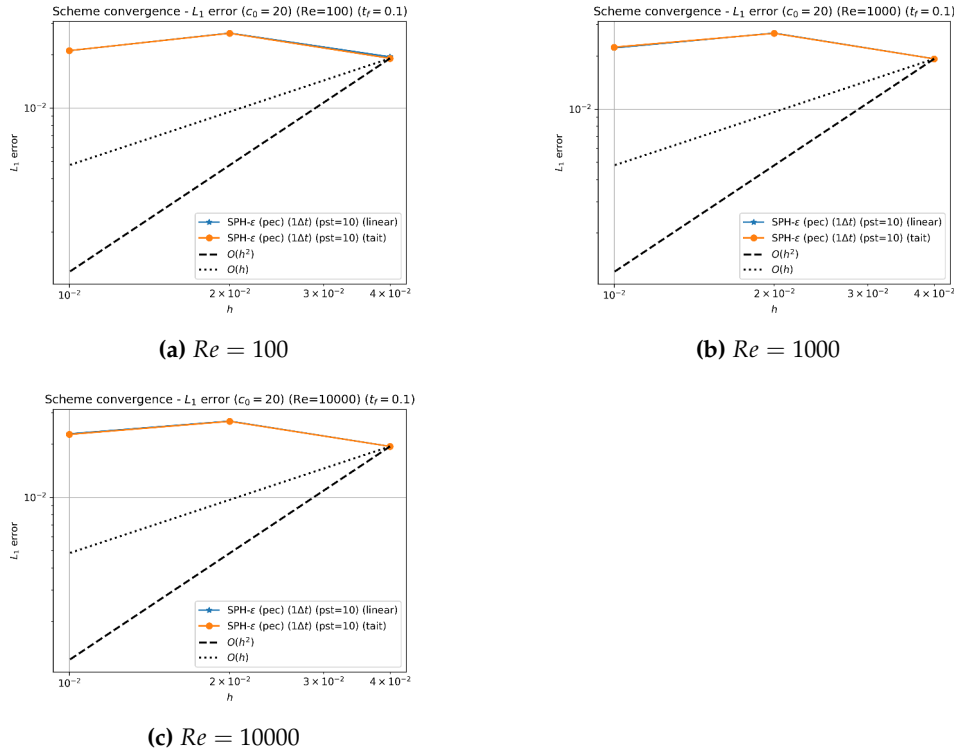


Figure 4.45: Convergence of the SPH- ϵ scheme for various equations of state.

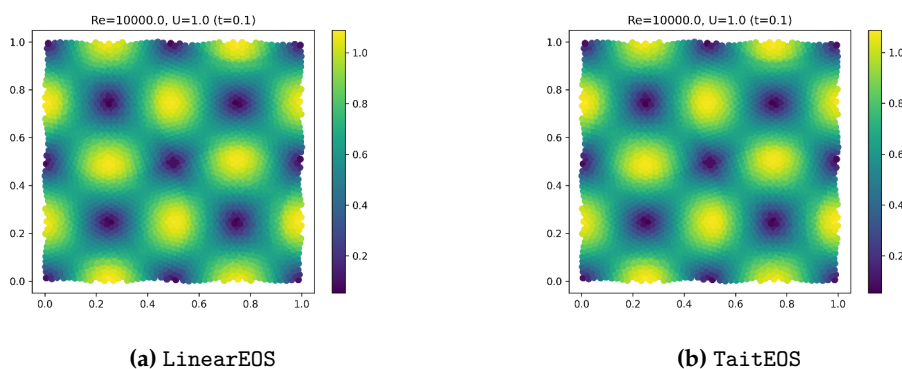


Figure 4.46: Velocity magnitude field for the SPH- ϵ scheme for various equations of state ($N = 50^2$, $t_f = 0.1$, $Re = 10000$, $c_s = 20$, $f_{pst} = 100$).

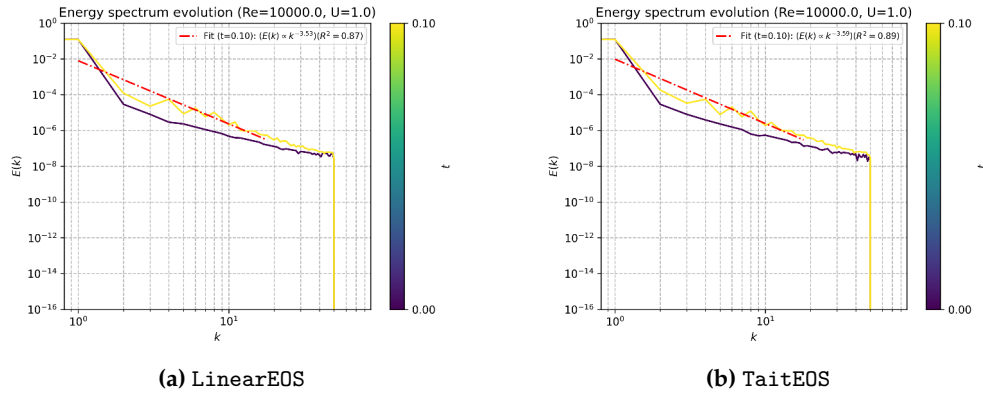


Figure 4.47: Evolution of the energy spectrum for the SPH- ϵ scheme for various equations of state ($N = 100^2$, $t_f = 0.1$, $Re = 10000$, $c_s = 20$, $f_{pst} = 100$).

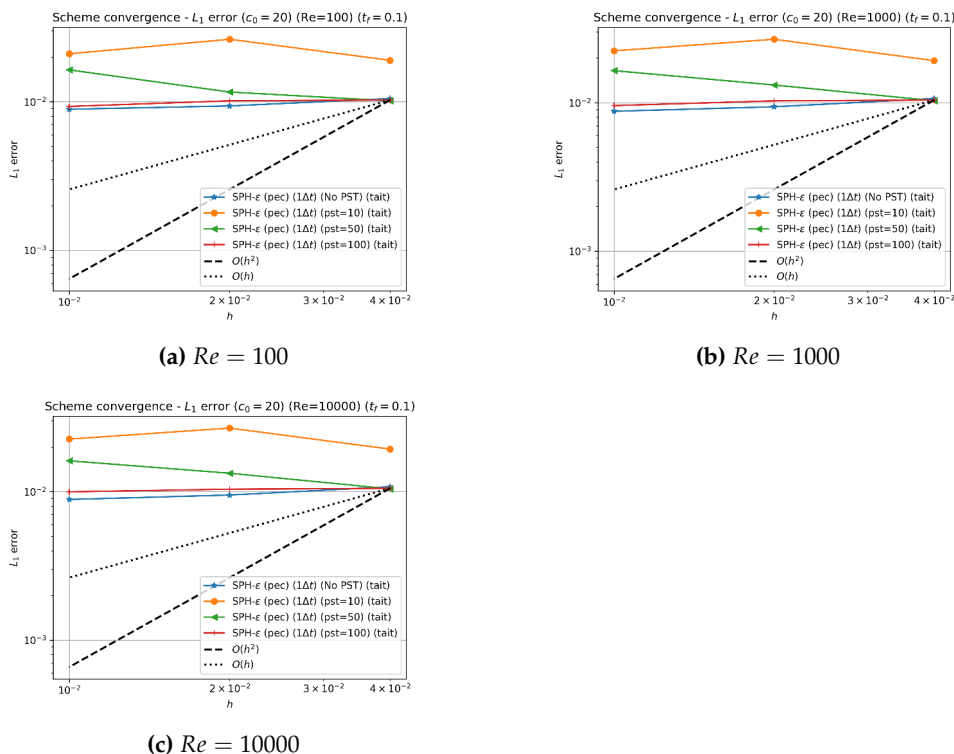


Figure 4.48: Convergence of the SPH- ϵ scheme for various f_{pst} values.

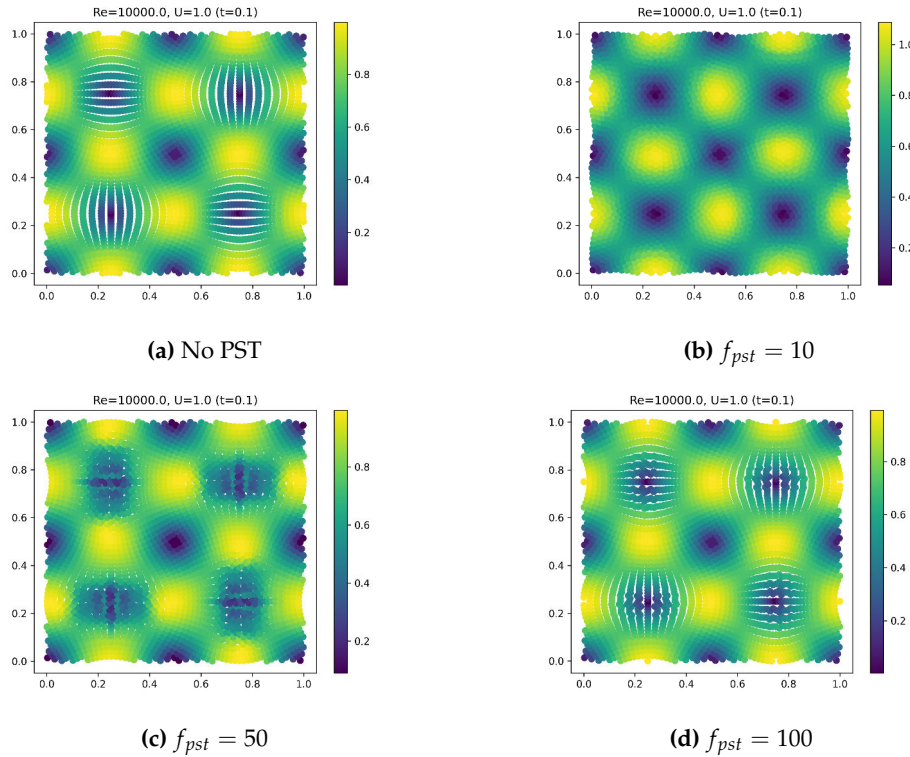


Figure 4.49: Velocity magnitude field for the SPH- ϵ scheme for various f_{pst} values ($N = 50^2$, $t_f = 0.1$, $Re = 10000$, $c_s = 20$).

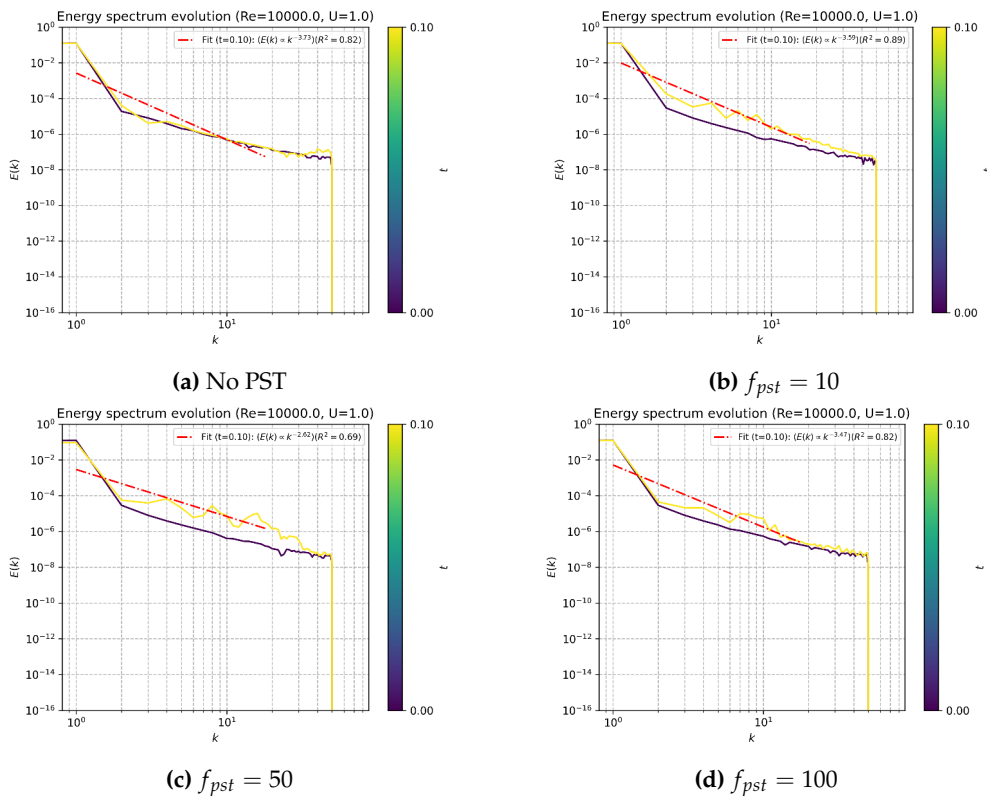


Figure 4.50: Evolution of the energy spectrum for the SPH- ϵ scheme for various f_{pst} values ($N = 100^2$, $t_f = 0.1$, $Re = 10000$, $c_s = 20$).

4.3 Long-time Simulations - Taylor-Green Vortex Problem

As mentioned in the previous section, a long-time simulation of the TGV problem was essential to understand each turbulence model regarding if and when instability would appear in the flow field. Therefore, the TGV problem was simulated for a more extended period of $t_f = 2.0$, for Reynolds number of $Re = [10^4, 10^5]$. Each simulation run was repeated for the resolutions of $N = [100^2, 200^2]$, with $c_s = 20$. The WendlandQuinticC4 kernel was used for all simulations, with a radius multiplier of 2.0. Further scheme-specific parameters are listed in [Table 4.2](#). The run time for the simulations is also listed in the table for the case of ($N = 200^2, Re = 10^5$), which was the most expensive simulation run. When arranged in order of increasing run time, the schemes are SPH- ϵ , L-IPST-C, $k - \epsilon$ SPH, and δ -LES-SPH. On the other hand, the SPH-LES scheme could never simulate the TGV problem for the given period; hence, the run time is not listed in the table.

The results will be presented in the subsequent sections. It should be noted that each scheme is assigned a unique colour for the plots. The opacity, i.e. the transparency of the colour, is used to indicate the resolution of the simulation, with the higher opacity indicating the higher resolution. For example, the blue line with the highest opacity indicates the results for the L-IPST-C scheme with $N = 200^2$.

Turbulence Model	Scheme Name	PST Frequency	Equation of State	Integrator	CFL	Scheme-specific Parameters	Run Time (in s) ($N = 200^2, Re = 10^5$)
Viscosity-based Model	Lagrangian with iterative PST and coupled- ϵ viscosity formulation (L-IPST-C)	10	TaitEDS	PEC	1	-	5000
Large Eddy Simulation-based Model	SPH-LES	10	TaitEDS	PEC	1	Viscous models=[SMAG, SMAG-MOD, SIGMA]	n.a.
Lagrangian LES-based Model	δ -LES-SPH(μ_0)	10	TaitEDS	RK2	1.5	No gradient correction;	8200
RANS-based $k - \epsilon$ Model	$k - \epsilon$ SPH	10	TaitEDS	PEC	1	Simplified $k - \epsilon$ transport equations;	6400
LANS-based Model	SPH- ϵ	10	TaitEDS	PEC	1	No gradient correction; $\epsilon = 0.5$;	3000

Table 4.2: Optimised SPH schemes for each category of turbulence model.

Since the problem does not have any external force or torque acting on the system, the angular and linear momentum of the system should be conserved. Therefore, on plotting the evolution of the angular and linear momentum of the system, as shown in [Fig. 4.51](#), it can be observed that the $k - \epsilon$ SPH scheme appears to be the only scheme that conserves both the angular and linear momentum to high precision (this will be discussed in more detail in the subsequent sections). The L-IPST-C scheme, and the δ -LES-SPH scheme, oscillate about the zero line but tend to stay bounded. The bounds become tighter with increasing resolution, indicating that the schemes converge to a solution. The SPH- ϵ scheme, on the other hand, appears to be the only scheme that does not follow any specific trend with increasing resolution. This is evident from the fact that the bounds on the angular and linear momentum of the system do not appear to converge to a specific value. Moreover, instances, when there are sudden jumps in the momentum of the system appear to be arbitrary, implying that the scheme is not conservative.

The various schemes' kinetic energy and velocity decay evolution is shown in [Fig. 4.52](#). Here, it is observed that for the L-IPST-C and δ -LES-SPH schemes, the kinetic energy and the decay follow the exact solution accurately, with this accuracy increasing with increasing resolution. It is also interesting to note that the L-IPST-C scheme generally over-predicts the energy in the system, and by increasing the resolution, this can be reduced. For the δ -LES-SPH scheme, it is the other way around, where the energy in the system is under-predicted, and increasing the resolution increases the energy in the system. Interestingly, the $k - \epsilon$ SPH scheme, the only scheme that conserved the system's angular and linear momentum, dissipates the system's energy drastically, even for the high Re case. Therefore, this 'almost' zero-energy solution,

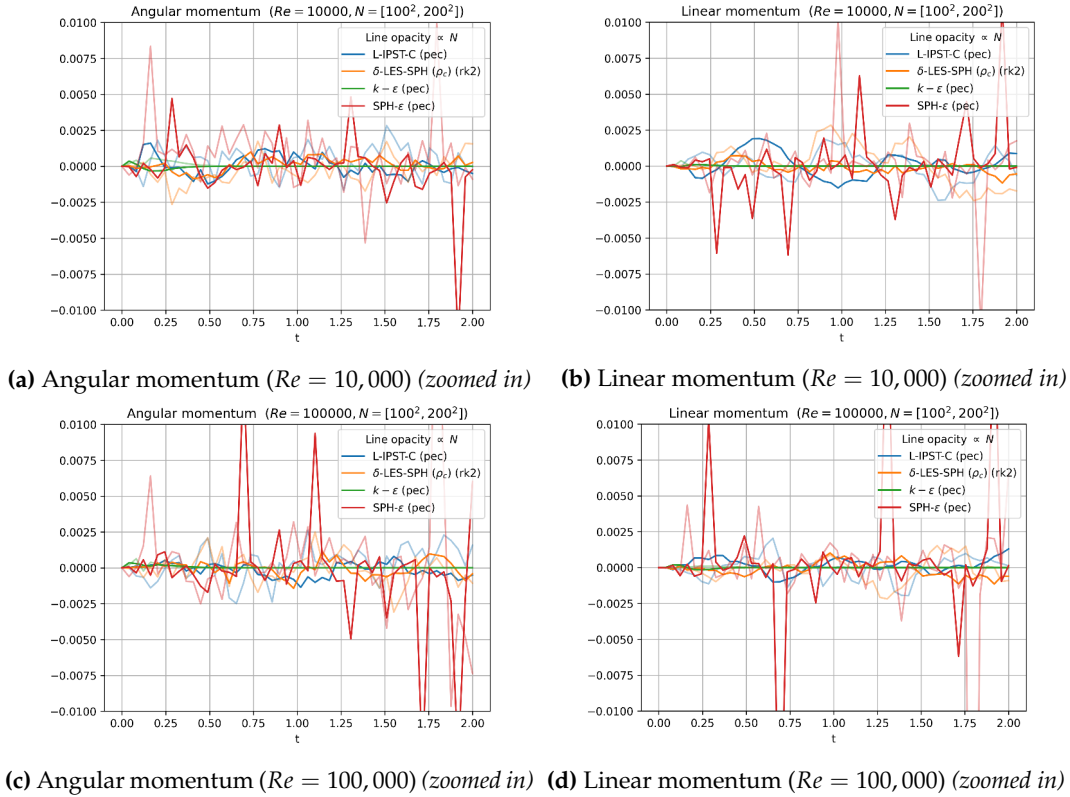


Figure 4.51: Evolution of the angular and linear momentum for various schemes ($N = [100^2, 200^2]$, $Re = [10^4, 10^5]$, $c_s = 20$).

which is not a physical solution, provided for such high precision in the conservation of the angular and linear momentum of the system, and not because of the accuracy of the scheme. The SPH- ϵ scheme, on the other hand, seems to constantly dump energy into the system, which, after a certain point, leads to instability in the system.

The evolution of the L_1 error for the various schemes is shown in Fig. 4.53. For the case of the L_1 error, which is a function of the velocity profile, the L-IPST-C scheme performs the best, followed by the δ -LES-SPH scheme. This is also supported by the actual velocity magnitude plots as shown in Fig. 4.54, where both schemes still accurately capture the velocity profile, even for the high Re case. With the SPH- ϵ scheme, the L_1 error is relatively high and diverges. However, the velocity magnitude plot still indicates the presence of the typical TGV vortex cells, but the magnitude of the velocity is significantly higher than the other schemes. This leads to the conclusion that the SPH- ϵ scheme can be a competitive alternative with a suitable dissipate mechanism. The same cannot be said for the $k - \epsilon$ SPH scheme, which, as mentioned, completely drains all the energy from the system, with even the velocity magnitude plot indicating random fluctuations in the velocity field. Supporting observations can also be made from the vorticity magnitude plots, shown in Fig. 4.55.

The evolution of the L_1 error for the pressure field for the various schemes is shown in Fig. 4.56. Here, we see that the L-IPST-C scheme produces the least error, which reduces with increasing resolution. The δ -LES-SPH scheme, interestingly, is significantly affected by the resolution of the simulation. Although the error rates for the resolution of $N = 200^2$ are under 20%, the error rates for the resolution of $N = 100^2$

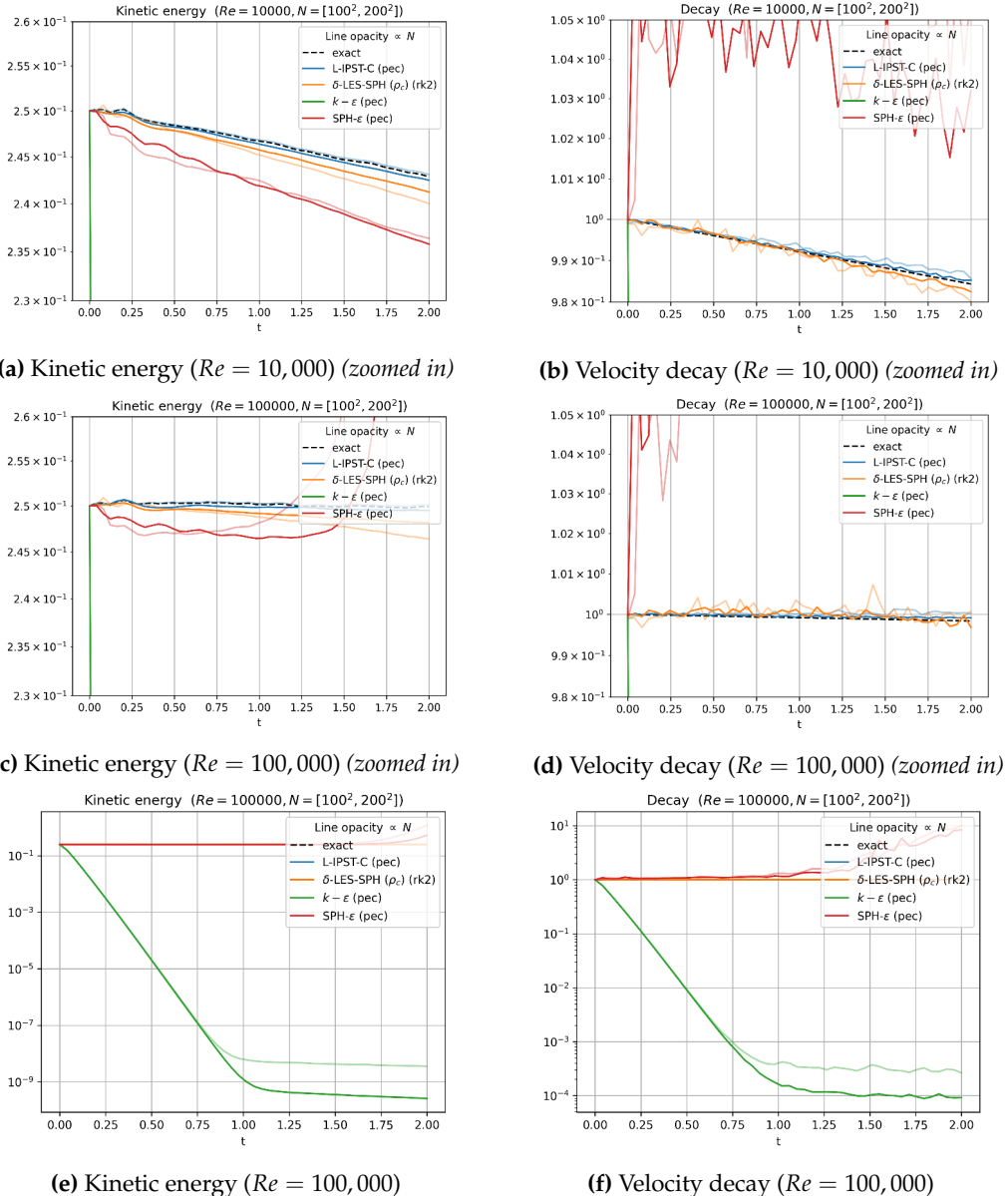


Figure 4.52: Evolution of the kinetic energy and velocity decay for various schemes ($N = [100^2, 200^2]$, $Re = [10^4, 10^5]$, $c_s = 20$).

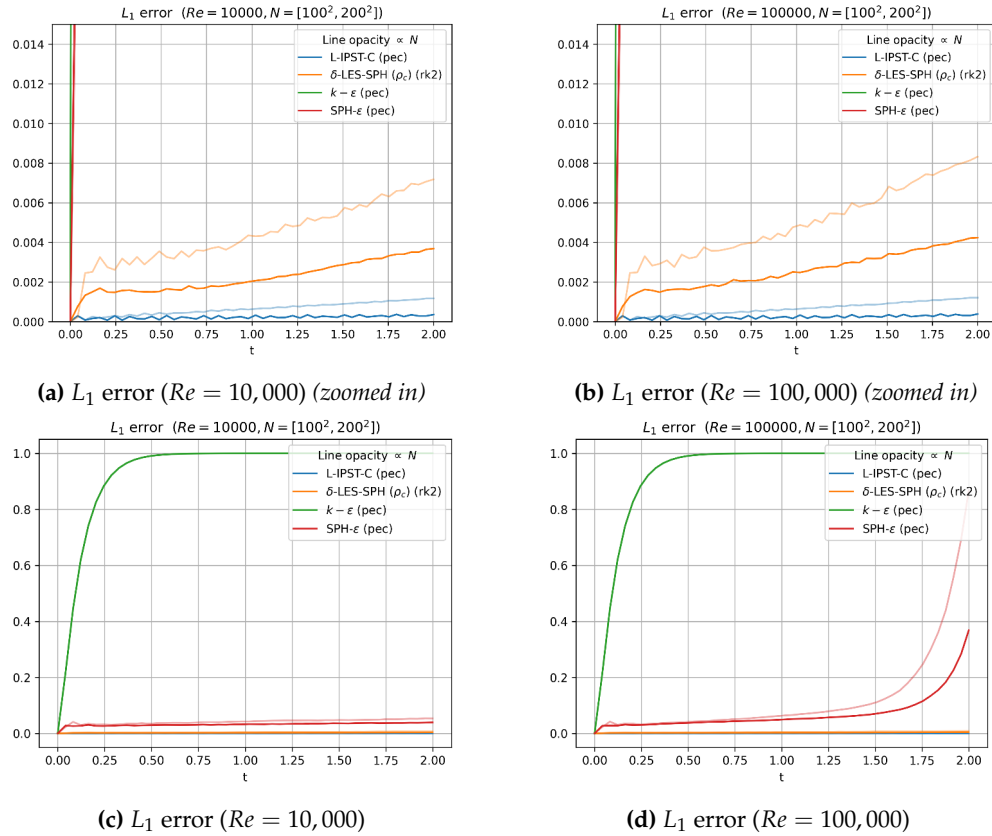


Figure 4.53: Evolution of the L_1 error for various schemes ($N = [100^2, 200^2]$, $Re = [10^4, 10^5]$, $c_s = 20$).

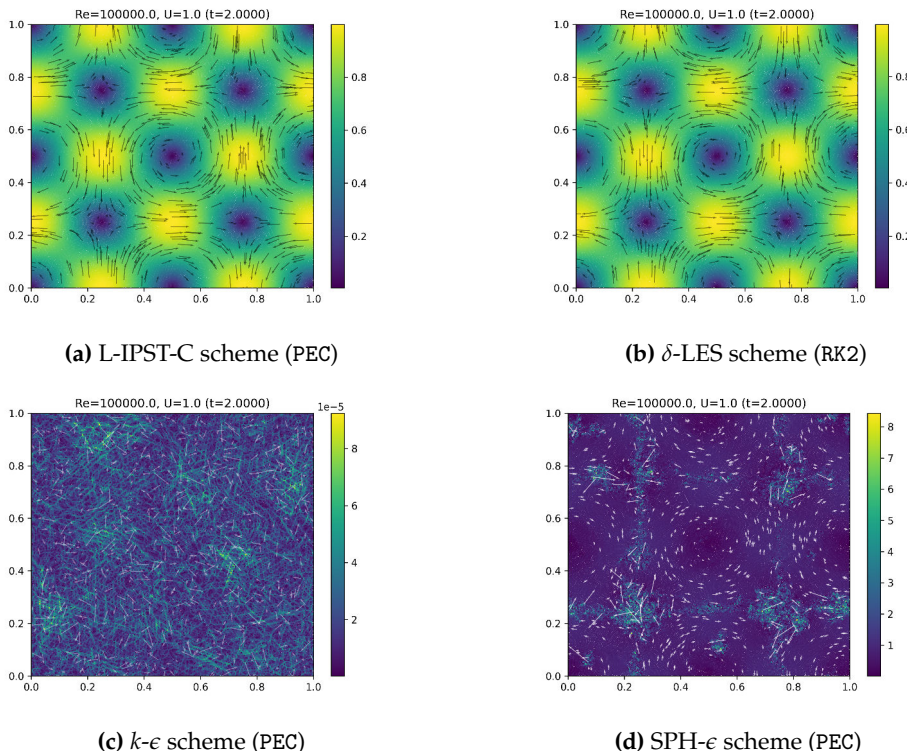


Figure 4.54: Velocity magnitude field (arrows represent the velocity vector) for various schemes ($N = 200^2$, $t_f = 2$, $Re = 10^5$, $c_s = 20$).

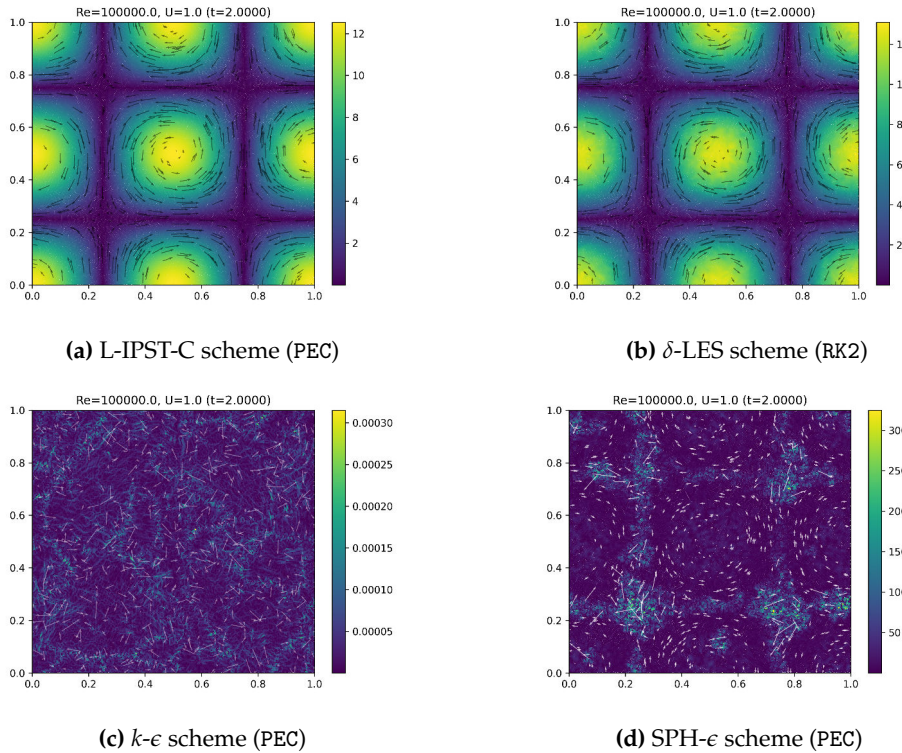


Figure 4.55: Vorticity magnitude field (*arrows represent the velocity vector*) for various schemes ($N = 200^2$, $t_f = 2$, $Re = 10^5$, $c_s = 20$).

are the most for all the schemes. This indicates that the δ -LES-SPH scheme will require much higher resolutions to produce accurate results than the L-IPST-C scheme. On observing the actual pressure field plots, as shown in Fig. 4.57, we see that both the L-IPST-C and δ -LES-SPH schemes can accurately capture the pressure field, even for the high Re case when $N = 200^2$. However, when the case for $N = 100^2$ is considered, we see that even though the δ -LES-SPH scheme can capture the pressure field, the magnitude of the pressure is significantly lower than that of the L-IPST-C scheme. Since all the formulations are weakly compressible, pressure has an explicit and closed-form expression with density. Correspondingly, by observing the density plots, as shown in Fig. 4.58, we note that the δ -LES-SPH scheme again captures the trends of the density field. However, the density's upper and lower limits are lower than the L-IPST-C scheme. This also is the case for the $N = 200^2$, but the difference is less significant. However, it may delay the inevitable since the error rates for the $N = 200^2$ case also increase with time. Hence, identifying the cause of this behaviour, and rectifying it, will be essential for the δ -LES-SPH scheme to be a viable alternative to the L-IPST-C scheme in terms of accuracy when it comes to the pressure and density field. With the $k - \epsilon$ SPH scheme, there is little to comment on besides that the density and the pressure field are noisy. On the other hand, with the SPH- ϵ scheme, L_1 error in pressure is comparable to that of the δ -LES-SPH case, with perhaps exaggerated trends. This is also evident with the pressure fields, where the SPH- ϵ scheme still appears to have maintained the pressure field trends, with the discrepancy coming from the more significant lower limits for the pressure field. Therefore, it is reasonable to conclude that these trends might result from a fundamental flaw affecting both schemes. A much more rigorous analysis would have to be performed to identify the cause of this behaviour.

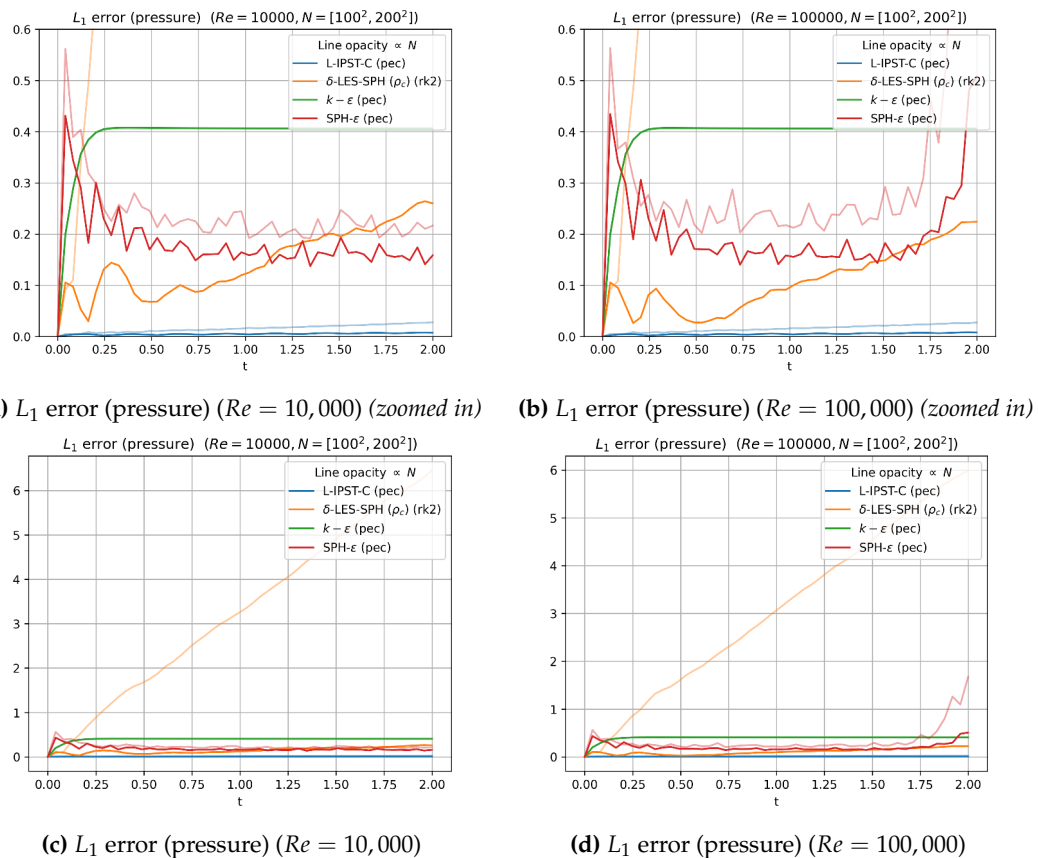


Figure 4.56: Evolution of the L_1 error (pressure) for various schemes
($N = [100^2, 200^2]$, $Re = [10^4, 10^5]$, $c_s = 20$).

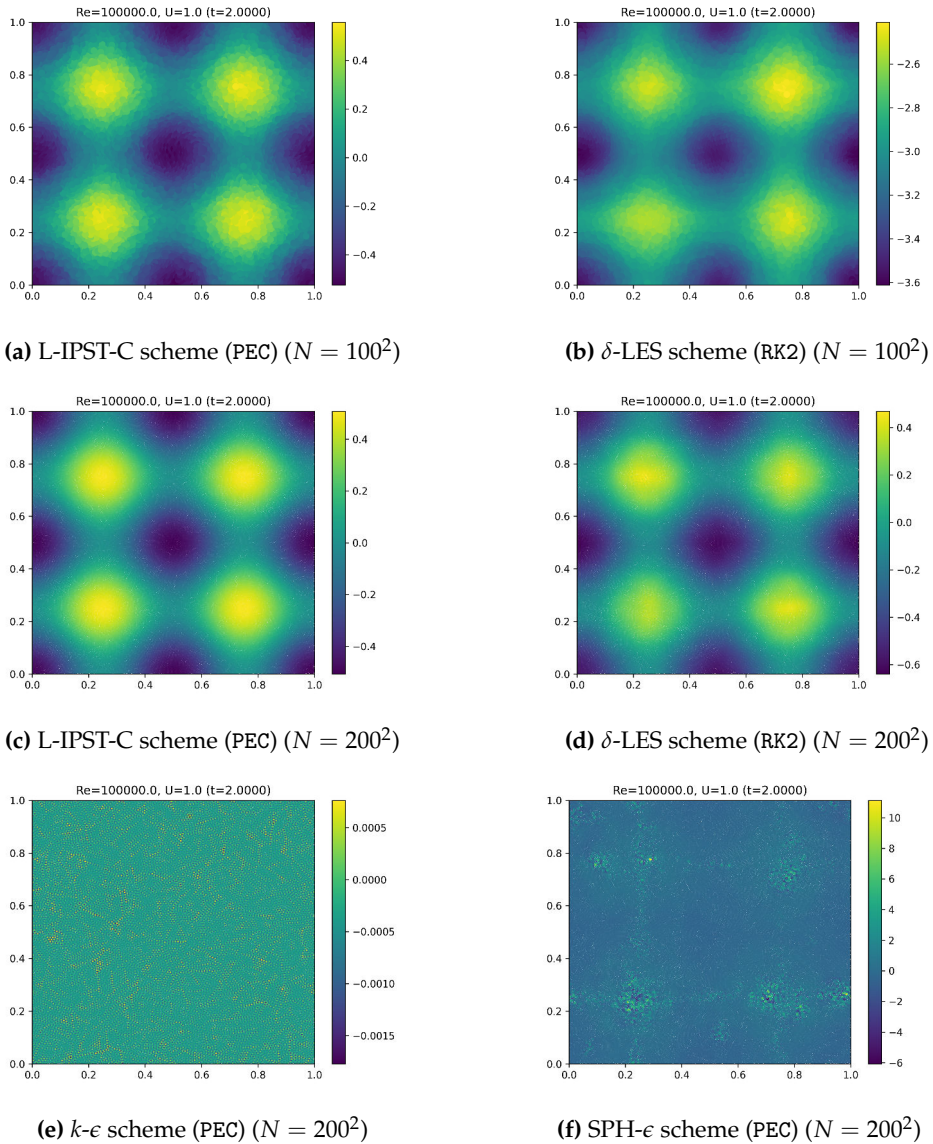


Figure 4.57: Pressure field for various schemes ($t_f = 2, Re = 10^5, c_s = 20$).

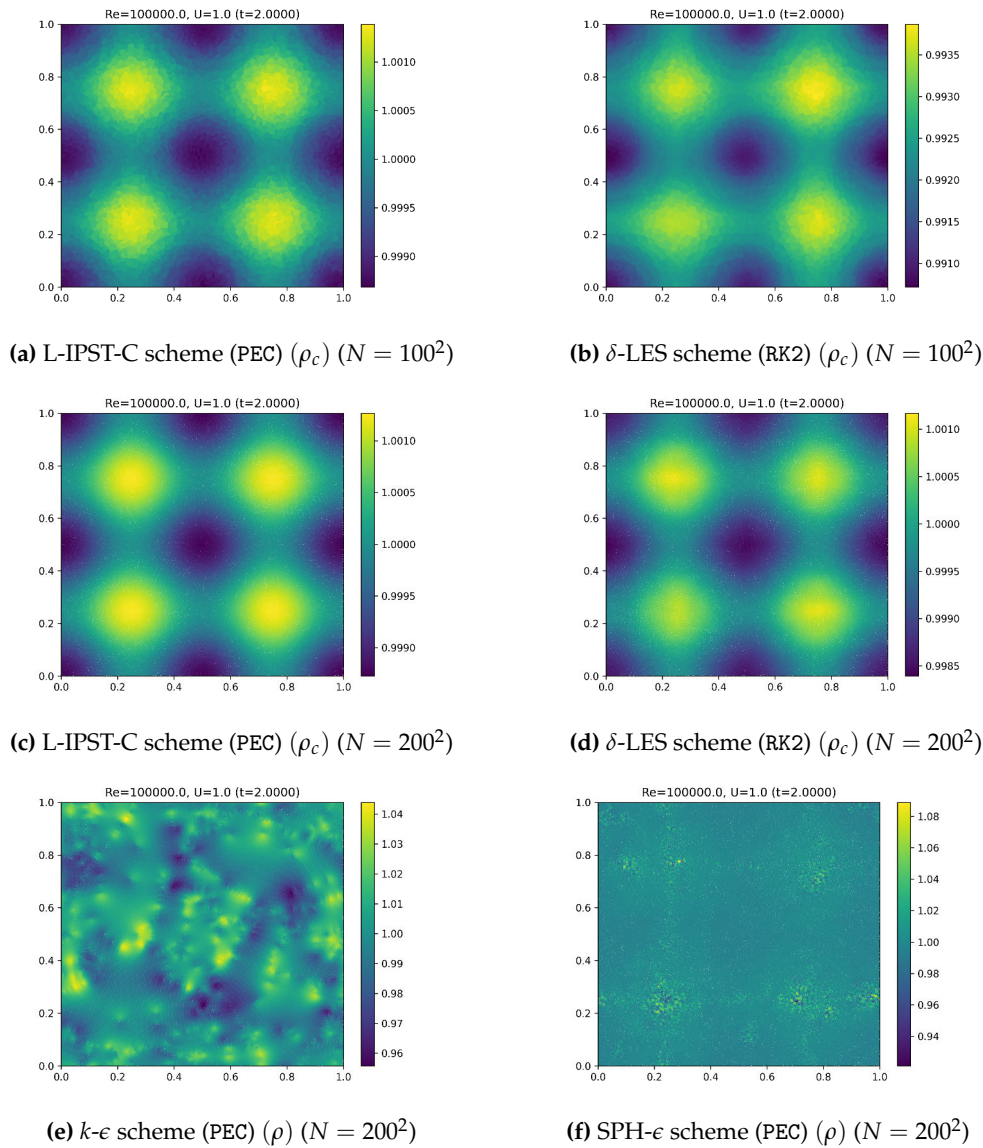


Figure 4.58: Density field for various schemes ($t_f = 2, Re = 10^5, c_s = 20$).

The evolution of the energy spectrum for the various schemes is shown in Fig. 4.59. Here, both the L-IPST-C and δ -LES-SPH schemes have a similar influence on the energy dissipation in the system over time. However, the δ -LES-SPH scheme does seem to perform better than the L-IPST-C scheme in terms of redistributing the energy to lower scales, which is evident from the lower slope, and increased energy in the lower scales at the expense of the higher scales with the δ -LES-SPH scheme. This is indeed what is expected from a reasonable turbulence model. This energy redistribution is something that the L-IPST-C scheme currently lacks and will need to be improved to serve as a suitable turbulence model. The observations with the $k - \epsilon$ SPH and SPH- ϵ schemes are much simpler to identify. The $k - \epsilon$ scheme reduces the energy for all scales drastically. In contrast, the SPH- ϵ scheme increases the energy in the smaller scales, with negligible effect on the large scales.

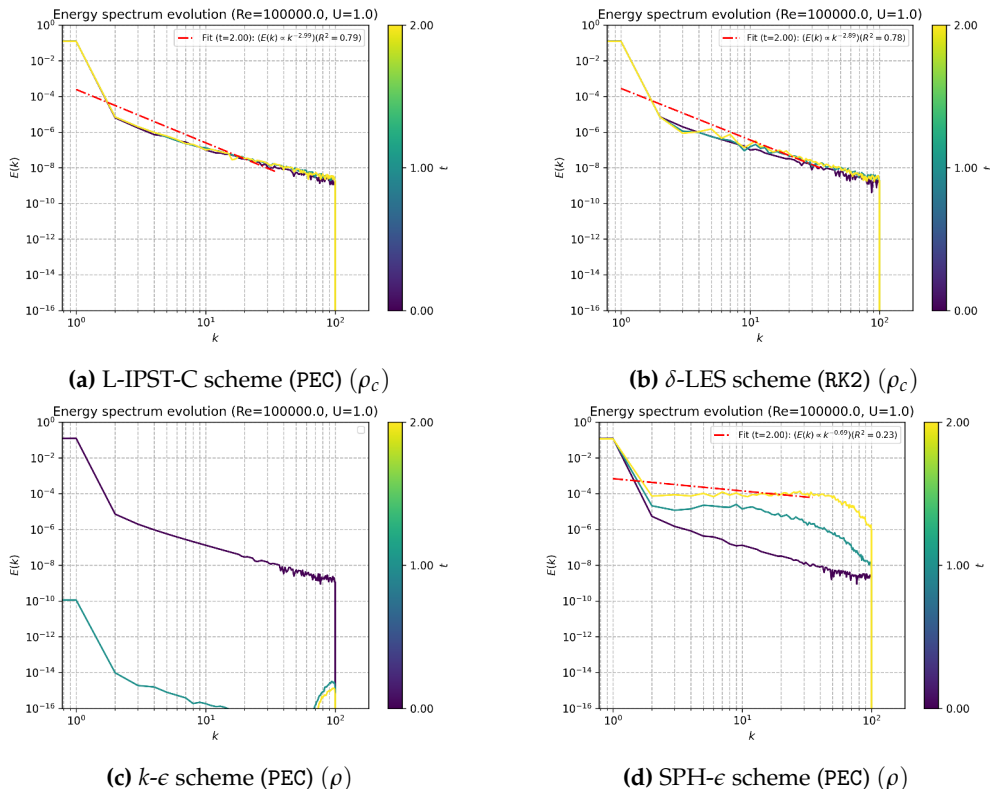


Figure 4.59: Evolution of the energy spectrum for various schemes ($N = 200^2, t_f = 2, Re = 10^5, c_s = 20$).

4.4 Externally Forced Variant - Taylor-Green Vortex Problem

From the previous section, it is evident that $k - \epsilon$ SPH and SPH- ϵ need to be improved before they can be considered potential turbulence modelling schemes in SPH. Therefore, to better gauge the differences between the L-IPST-C and δ -LES-SPH schemes, the externally forced TGV problem is considered. Detailed in the work of Antuono et al. 2021, this 2D problem is driven by a forcing function, given by:

$$\mathbf{F}_{2D} = r(t^*)A \left(\sin(8\pi x^*) \cos(8\pi y^*), -\cos(8\pi x^*) \sin(8\pi y^*) \right), \quad (4.31)$$

where $t^* = tU/L$, $\mathbf{x}^* = \mathbf{x}/L$, and $A = 1.3U^2/L$. U and L are the system's characteristic velocity and length scales, respectively. The ramp function $r(t^*)$ is given by:

$$r(t^*) = \begin{cases} 10t^* & \text{for } t^* \in [0, 0.1), \\ 1 & \text{for } t^* \in [0.1, 0.9), \\ 10(1 - t^*) & \text{for } t^* \in [0.9, 1), \\ 0 & \text{for } t^* \geq 1. \end{cases} \quad (4.32)$$

The author simulated this problem for a Reynolds number range of $Re = [10^4, 10^5, 10^6]$, with a resolution of $N = 1200^2$, using an RK4 time integrator, and a WendlandQuinticC2 kernel. For the sake of uniformity and computational feasibility, the same problem is run by the L-IPST-C and δ -LES-SPH schemes, with a resolution of $N = [100^2, 200^2]$, and other scheme-specific parameters as mentioned in [Table 4.2](#).

The kinetic energy evolution for various Re is shown in [Fig. 4.60](#). As had been discussed in the previous section, regarding the over-predicting and under-predicting nature of the L-IPST-C and δ -LES-SPH schemes, respectively, when it comes to the energy of the system, we see similar trends here as well. This causes the L-IPST-C scheme to blow up for all Re when $N = 100^2$ even after the forcing term has been switched off. However, when the resolution is increased to $N = 200^2$, the L-IPST-C scheme can track the trend as the authors observe, albeit with a slight over-prediction. This manifests in the energy appearing to diverge towards the end of the 3s mark. Therefore, it is safe to conclude that the simulation cannot run longer without a significantly large resolution. The authors, however, were able to simulate the problem for $t_f = 20s$ in their work. They have made the data available in the form of a video titled: SPH LES TurboMixer N1200 Re=1M, Q, Curl, Pr, Lyap.

On the other hand, the δ -LES-SPH scheme continues to underpredict the system's energy, even for the $N = 200^2$ case. There might be credible reasons for this, considering that the author used the same scheme but with a resolution that is $6x$ finer. This would imply that if we consider the fact that the δ -LES-SPH scheme will continue to reduce the error in under-predicting the energy of the system, with increasing resolution, it is possible that the exact results obtained by the authors, can be reproduced with simply a much higher resolution.

The evolution of the energy spectrum for $Re = 10^6$ is shown in [Fig. 4.61](#). It must be highlighted that the multiple coloured lines in the computed energy spectrum plots refer to the energy spectrum at different time instances. The dark blue line represents the energy spectrum at the earliest time, and the yellow line represents the energy spectrum at the final time, with the other colours representing the energy spectrum at intermediate time instances. It is immediately noted that this is not a fair comparison with the data obtained from the authors since they used a much finer resolution, allowing for much larger wavenumbers to be captured in the energy spectrum. Therefore, only the trends are compared here qualitatively. The slope of the line is calculated using the first quartile of the energy spectrum. The slope obtained from the L-IPST-C scheme is -1.77 at the final time instance, which is appropriately $-5/3$ and, therefore, close to the expected slope for the inertial subrange. However, the energy in the lower scales is also significant, and the expected slope of -3 for the viscous subrange is not observed. This would imply the lack of

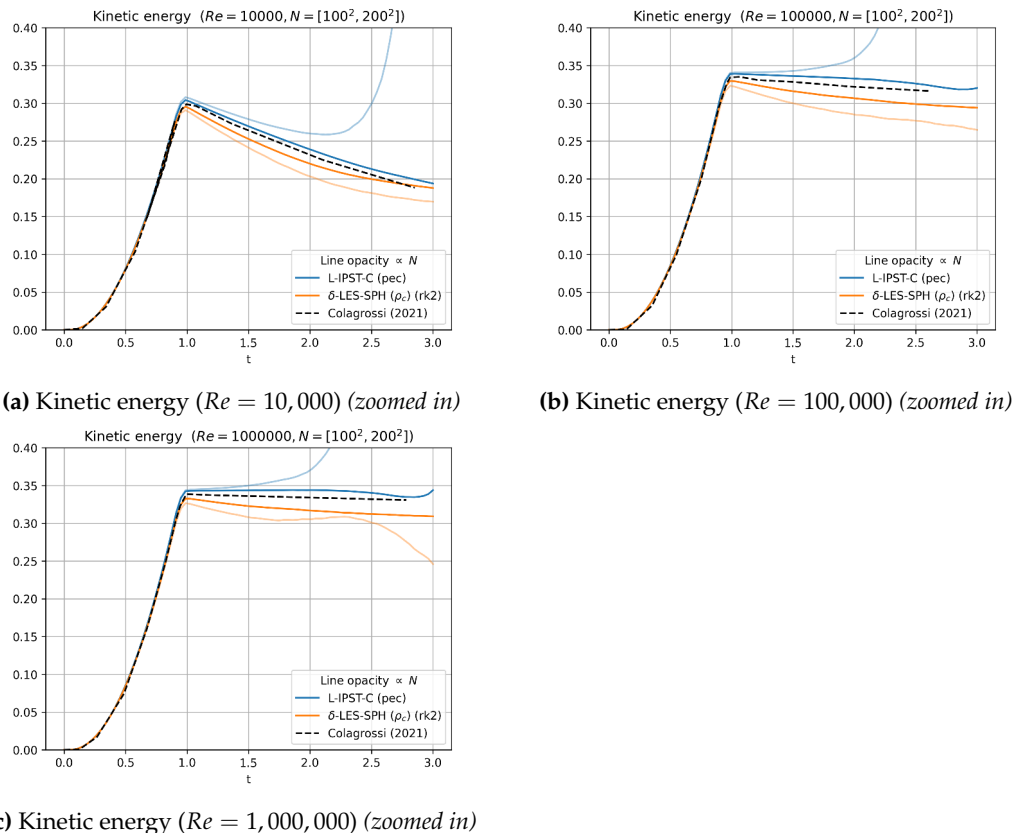


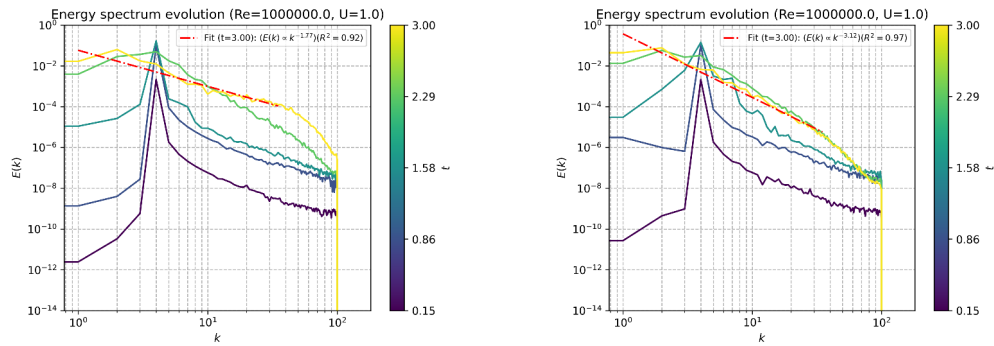
Figure 4.60: Evolution of the kinetic energy for the externally-forced TGV problem ($N = [100^2, 200^2]$, $Re = [10^4, 10^5, 10^6]$, $c_s = 20$). Compared with data obtained from Antuono et al. 2021.

a robust viscous dissipation mechanism. This is also evident in the velocity magnitude plots, shown in Fig. 4.62, where we can see a noisy velocity field, implying the presence of particles with relatively high energy throughout the domain. Similarly, in the vorticity plots, shown in Fig. 4.63, we see that the vorticity field is extremely noisy and does not appear to have coherent vorticity structures. Therefore, it is reasonable to conclude that the reason for the L-IPST-C scheme to predict a slope of $-5/3$ might have more to do with the fact that the particles are no longer associated with eddies, and are instead being advected arbitrarily, without a viscous term to curtail their motion and organise them into Lagrangian coherent structures.

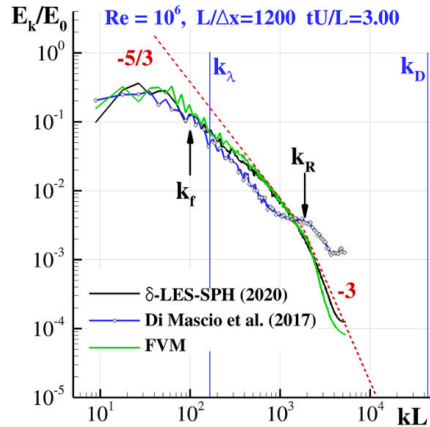
On the other hand, the slope obtained from the δ -LES-SPH scheme is -3.12 , which is close to the slope expected in the viscous subrange, but appears in the inertial subrange instead. This shows that the δ -LES-SPH scheme has a robust viscous dissipation mechanism, causing a steep energy redistribution from a much larger scale than expected. This implies that the velocity magnitude field would be much smoother, and the flow would be characterised by significantly larger eddies that contain the bulk of the energy and a cascade of energy to lower scales through smaller and smaller structures. This is what is seen in Fig. 4.62. A similar conclusion can be made from observing the vorticity field, as shown in Fig. 4.63. The vorticity field obtained from the δ -LES-SPH scheme is much smoother and appears to have coherent vorticity structures. This indicates that merely increasing the resolution of the L-IPST-C scheme will not be sufficient to turn it into a suitable turbulence model. Instead, a mechanism to dissipate energy at smaller scales will have to be introduced, allowing the energy to cascade to smaller scales and dissipate at the viscous subrange. This also gives a reasonable explanation behind the over-predicting and under-predicting predicament of these two schemes.

The pressure field for the $Re = 10^6$ case is shown in Fig. 4.64. Here we see that the L-IPST-C scheme has been able to maintain the pressure field trends, but that is not the case with the δ -LES-SPH scheme, where like the earlier case, the limits of the pressure field are much lower than that of the L-IPST-C scheme. This needs to be studied further since the pressure field is a significant quantity when it comes to the applications of turbulence modelling.

Finally, the various schemes' angular and linear momentum evolution is shown in Fig. 4.65. These quantities would have to be conserved here since the net force on the system is zero. The expected trend of improved bounds around the zero line with increased resolution is observed. However, the L-IPST-C scheme is not as conservative as the δ -LES-SPH scheme regarding being bounded or having similar zones of peaks and troughs.

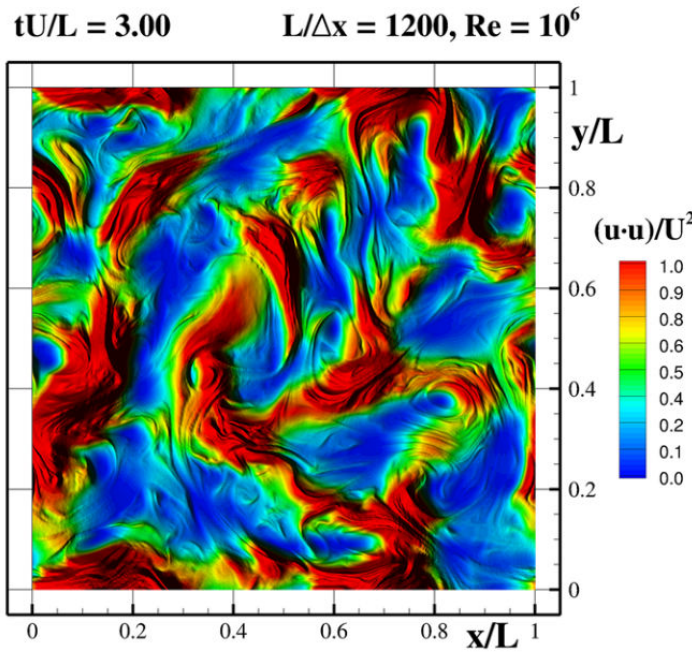


(a) Energy spectrum computed using L-IPST scheme ($Re = 1,000,000$) (b) Energy spectrum computed using δ -LES-SPH scheme ($Re = 1,000,000$)

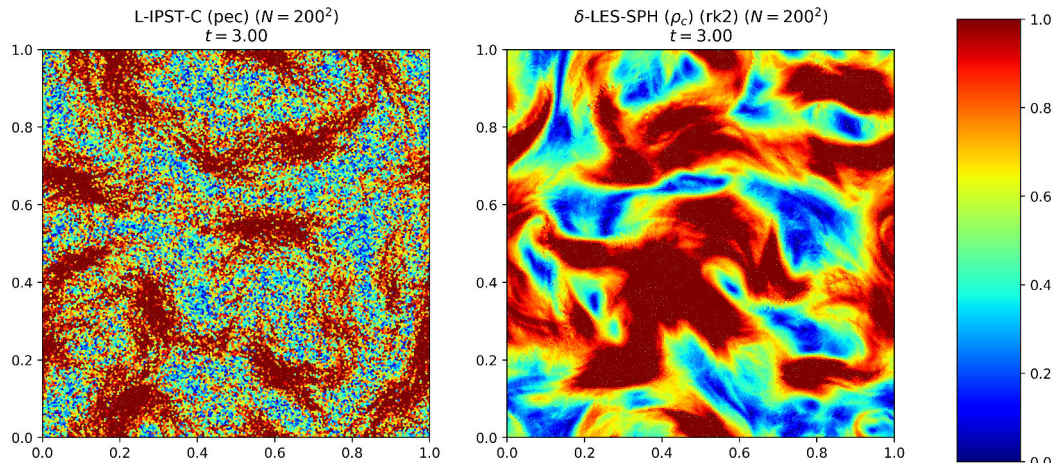


(c) Energy spectrum ($Re = 1,000,000$), reproduced from Antuono et al. 2021

Figure 4.61: Evolution of the energy spectrum for the externally-forced TGV problem ($N = 200^2$, $t_f = 3$, $Re = 10^6$, $c_s = 20$). Compared with data obtained from Antuono et al. 2021.



(a) Velocity magnitude field ($Re = 10^6$), reproduced from Antuono et al.
2021



(b) Velocity magnitude field ($Re = 10^6$), computed from the L-IPST-C and δ -LES-SPH schemes

Figure 4.62: Comparison between expected velocity magnitude field (Antuono et al. 2021), and the computed velocity magnitude field for the externally-forced TGV problem ($N = 200^2, t_f = 1.92, Re = 10^6, c_s = 20$).

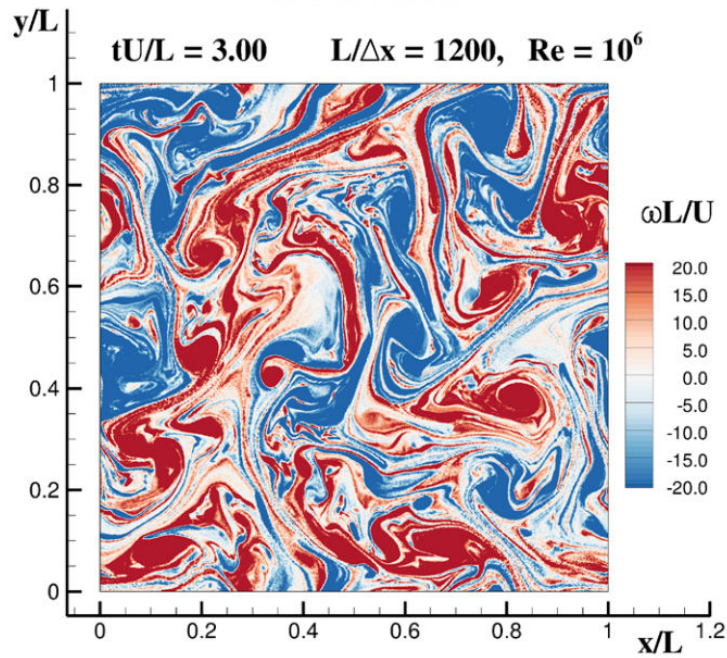
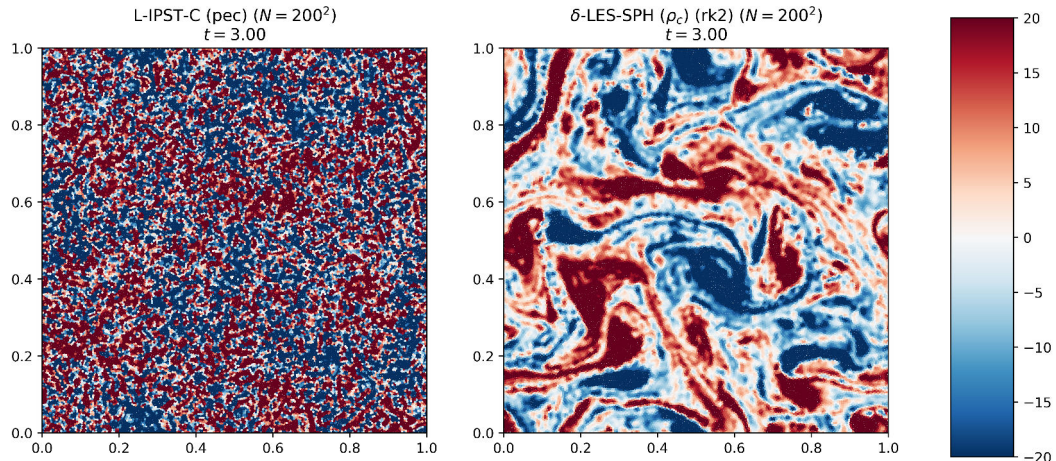
(a) ω_z field ($Re = 10^6$), reproduced from Antuono et al. 2021(b) ω_z field ($Re = 10^6$), computed from the L-IPST-C and δ -LES-SPH schemes

Figure 4.63: Comparison between expected ω_z field (Antuono et al. 2021), and the computed ω_z field for the externally-forced TGV problem ($N = 200^2, t_f = 1.92, Re = 10^6, c_s = 20$).

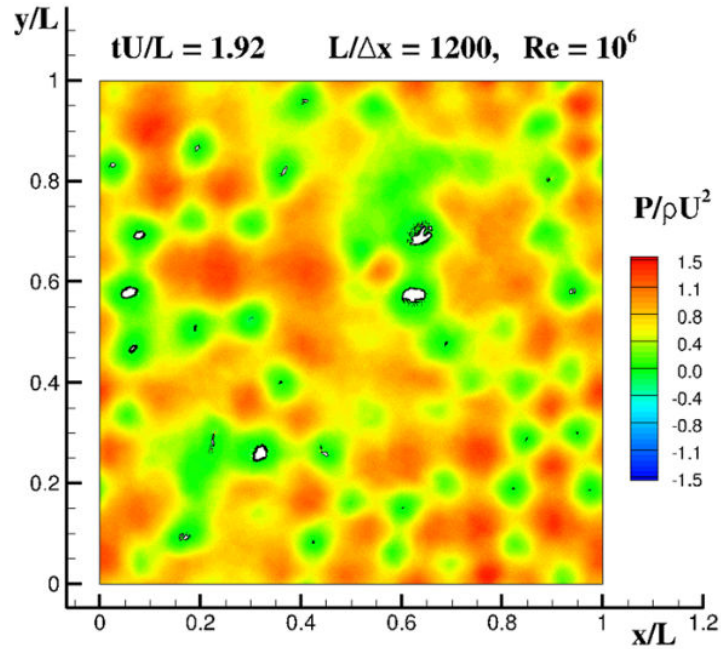
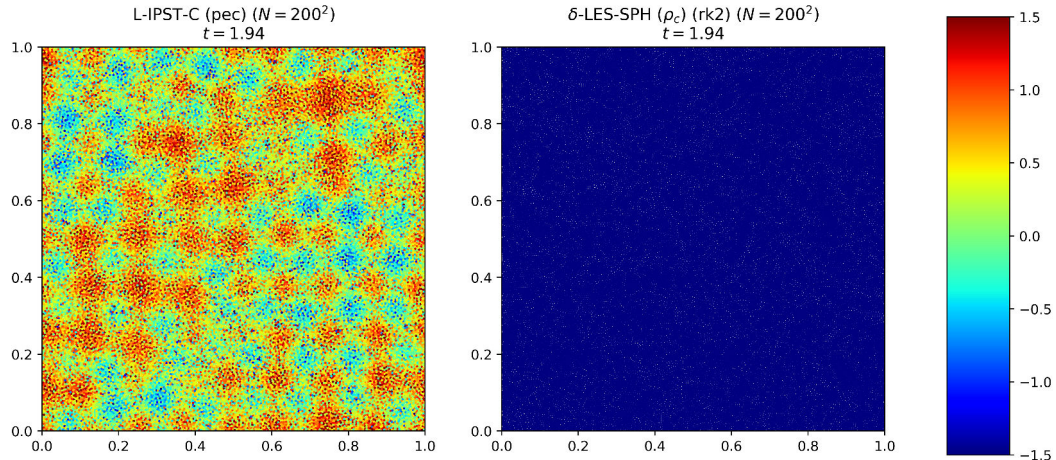
(a) Pressure field ($Re = 10^6$), reproduced from Antuono et al. 2021(b) Pressure field ($Re = 10^6$), computed from the L-IPST-C and δ -LES-SPH schemes

Figure 4.64: Comparison between expected pressure field (Antuono et al. 2021), and the computed pressure field for the externally-forced TGV problem ($N = 200^2, t_f = 1.92, Re = 10^6, c_s = 20$).

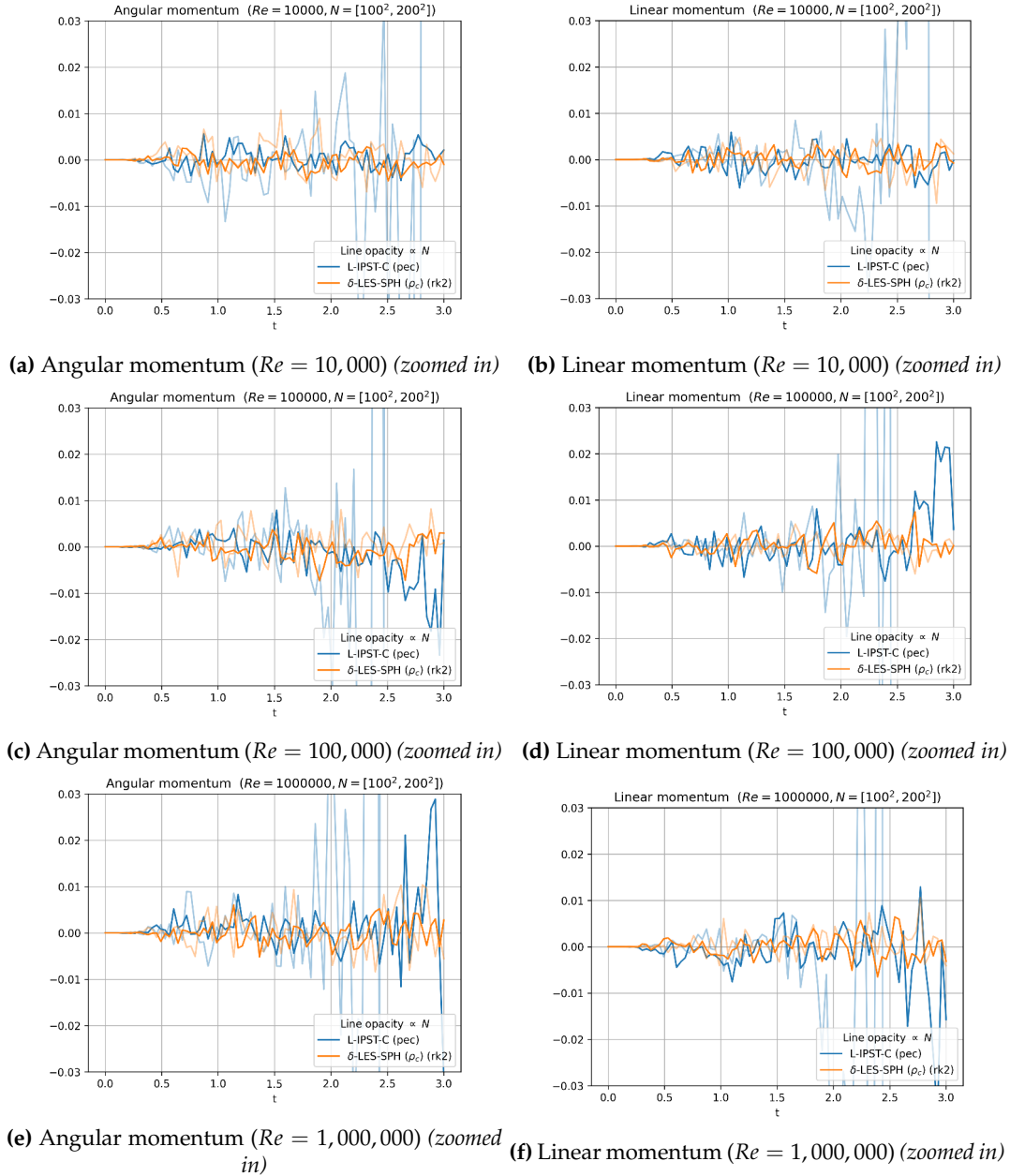


Figure 4.65: Evolution of the angular and linear momentum for the externally-forced TGV problem ($N = [100^2, 200^2]$, $Re = [10^4, 10^5, 10^6]$, $c_s = 20$).

5 Conclusion & Future Work

Werner Heisenberg, an eminent theoretical physicist of the 20th century and one of the pioneers of quantum mechanics, said -

"When I meet God, I am going to ask him two questions: why relativity?
And why turbulence? I really believe he will have an answer for the
first."

His tongue-in-cheek quip regarding turbulence seems relevant even today, given that the comprehensive turbulence theory still eludes us. This is a testament to the complexity of dealing with turbulence from a theoretical and numerical perspective.

Marking the culmination of this project, all of the work done so far and the conclusions drawn from the results are summarised in this chapter. It also discusses the future work that can be done to further this project's scope. A vital component of this project involved compiling a comprehensive database of past SPH turbulence models. Each model has been listed, with their governing equations, SPH discretisations and derivation, if available. The limitations of each model have also been discussed, as well as potential areas for refinement and any advantages they provide when dealing with a specific class of problems.

Efforts to extend the EDAC scheme (Prabhu Ramachandran and Puri 2019) with the Lagrangian LES model is rendered challenging as detailed in Sec. 2.3.1. The scheme also cannot make use of RANS-based models since the averaging technique assumes incompressibility, which simplifies to $(\nabla \cdot \mathbf{v} = 0)$, which would affect the transport equation for pressure Eq. 2.93 which contains a term dependent of the divergence of velocity. Therefore, a potential avenue of future work would be to consider the compressible form of EDAC (Chola and Shintake 2021) and develop a suitable turbulence for the scheme. This would be a fruitful endeavour since the scheme typically produces a smoother and more accurate pressure distribution for flows, confined or free, without requiring artificial viscosity. This would significantly improve the current state-of-the-art SPH schemes, which are typically plagued by spurious pressure oscillations.

The project further led to a better understanding of post-processing techniques available for SPH problems to study the effect of turbulence and the evolution of the flow fields. Characterisation of the energy spectrum of the flow, a standard technique employed in the FEM/FVM community, had been challenging for the particle-based Lagrangian method of SPH. This project, through a comparative study of various interpolation techniques, kernel type, kernel radius scale, particle resolution and the amount of disorder in their spacing, allowed for appropriate recommendations to be made. This resulted in the development of a TurbulentFlowApp class for the PySPH framework, which can be used to study the energy spectrum of the flow. Similar work was attempted to characterise the FTLE fields between two-time instances of the flow. However, the results revealed that this, at best, provides a qualitative measure of the attracting/repelling pathlines, which could only be used for visualisation

purposes and possibly not for quantitative analysis. The method of using tracer particles is suggested as a potential alternative to explore in the future. They have the advantage of being able to be advected by the flow and can store the exact forces acting on them, which can be used to analyse the flow quantitatively. Other methods that track the Lagrangian coherent structures (LCS) in the flow, such as in the work of Shadden, Lekien, and Jerrold E Marsden 2005, should be explored in future.

With the post-processing aspect of the project complete, the next stage involved identifying representative schemes from each class of the five major turbulence models and implementing them in PySPH. This allowed a detailed study of the performance of each of the models. Potential refinements in terms of scheme-specific parameters were also identified, along with improvements that could be made to the SPH discretisation. These results have been compiled in [Table 4.2](#). The comparative study involved studying the schemes at three levels of Reynolds number regimes $Re : [10^2, 10^3, 10^4]$ at multiple resolution scales. This made a study on the convergence order of these schemes possible. Furthermore, through the means of the energy spectrum, and flow field visualisation, a detailed analysis of the schemes' performance has been compiled. It was also instrumental in identifying the issues with the schemes' implementation as described solely from the literature. This shows that reproducing a scheme's results from literature is not trivial and requires a detailed understanding of the scheme and the ability to identify the key parameters that affect the scheme's performance. This task is not made any more accessible because the codes are generally not made available, and the schemes need to be implemented in a standardised manner. This also concerns SPH, which, unlike its typical CFD counterparts, needs more standardisation and is currently challenging to reproduce the results from the research literature. This could be a hurdle in the widespread adoption of SPH as a viable alternative to FEM/FVM, especially in turbulence modelling.

Once the schemes were optimised, the project involved a long-time simulation analysis in evaluating the performance of these schemes based on identifying potential instabilities that could creep into the flow from the building of numerical errors or issues with the physical modelling. This study simulated the TGV problem at two levels of Reynolds number regimes $Re : [10^4, 10^5]$ across two finer resolution levels $N : [100^2, 200^2]$. The comparative study, through the use of L_1 and L_∞ errors, also made use of the energy spectrums, and visualisation of flow field properties such as $|\mathbf{v}|, P, \rho$, and $\mathbf{!}$, to comprehensively evaluate the performance and behaviour of the schemes. It proved crucial in demonstrating how the SPH- ϵ and $k - \epsilon$ schemes are unsuitable and must be improved before they are viable for practical use. On the contrary, the L-IPST-C and δ -LES-SPH schemes were the most promising and could produce results that agreed with the reference solution. The work also identified how the four schemes could be refined further to improve their convergence order and reduce the numerical errors that creep into the flow.

The inadequacies of using TGV as a benchmark problem were realised at this stage of the project, despite it serving as an excellent problem to perform OOC analysis. However, to study the long-term behaviour of these schemes, more complex flow fields will have to be taken up as benchmark problems. It is also important to note that problems with solid boundaries will be required to evaluate these schemes in a more realistic setting. The TGV problem, being a periodic domain, did not allow for the study of boundary conditions, which are a crucial aspect of turbulence modelling.

However, the L-IPST-C and δ -LES-SPH schemes were studied with the externally forced variant of the TGV problem at three levels of Reynolds number regimes $Re : [10^4, 10^5, 10^6]$, across two levels of resolution $N : [100^2, 200^2]$. This allowed for a deeper understanding of these schemes and their ability to model the turbulent flow. Their effect on the energy spectrum, flow field, and vortical structures could be better studied in detail. The studies also were crucial in identifying the nature and cause of the L-IPST-C scheme in over-predicting the system's energy due to the lack of a reasonable viscous dissipation mechanism. This was also the cause of the scheme's inability to redistribute the energy to the lower scales of the flow with typical cascade behaviour expected for the inertial and viscous sub-ranges. Consequently, the scheme was demonstrated to lead to a lack of total vortical structures in the flow because the particles that build up energy cannot dissipate it and move freely across the domain, leading to noisy velocity fields. On the other hand, the δ -LES-SPH scheme suffered from the opposite issue. It under-predicts the energy of the system. The viscous dissipation mechanism is overly-powerful, leading to a much steeper energy spectrum in the inertial sub-range. Therefore, the scheme should be refined to reduce this behaviour and allow for a more realistic cascade trend to form.

Such a study showed the importance of still having a periodic problem with complex yet predictable flow fields, which can be used to study how the schemes perform in the presence of Re -onset instabilities and how they affect the flow field. Such periodic problems would still have much insight to offer in terms of turbulence modelling while also being computationally easier to implement and solve. This project also highlighted the current bottleneck in terms of computational speed when it comes to solving periodic problems using the PySPH framework. This issue does not allow the simulation to scale efficiently using more processors. The cause of this is attributed to the serial copying of data required by the particles near the boundary to enforce true periodic boundary conditions. This process is not parallelised; therefore, as the number of particles increases, the computational cost increases linearly. It was observed that typically 40 – 65% of the run time was taken by this serial process for resolutions of $N = 100^2 – 200^2$. Amdahl's law states that the speedup of a program using multiple processors is limited by the time taken by the serial portion of the program. Therefore, this known issue will have to be addressed in order to scale the simulation to higher resolutions and still be able to run using a reasonable amount of time and computational resources. Through this project, a preliminary study was performed to try and rectify this issue. It involved interpolating the properties of the particles near the boundary from the particles on the opposite side of the domain. However, early results indicated that such a technique would be bespoke to each scheme and, therefore, would not be a generalised solution. There would also present a trade-off between the computational cost of the serial process and the loss in accuracy from this interpolation method, not to mention a much higher memory requirement. This is because many more layers of ghost particles are required near the boundaries, which must be closely packed for even the most basic SPH operators to maintain still SOC. Therefore, this issue and a suitable solution to it will have to be addressed to scale the simulation to higher resolutions which will be necessary when dealing with massive complex flow fields that exhibit isotropic turbulence.

Future work incorporating adaptive particle refinement to reduce the computational cost can also be considered, as shown in the work of Muta and Prabhu Ramachandran 2022. However, this can be undertaken only when the scheme is robust and accurate in a standard particle setting. There could also be issues with the energy

distribution across scales with adaptive refinement, which must be studied carefully. Such a development would allow for simulations involving moving or deformable geometries, in which case the issue of the computational cost could become unfeasible. The work of Haftu, Muta, and Prabhu Ramachandran 2022 on parallel adaptive WCSPH and Negi, Prabhu Ramachandran, and Haftu 2020 on inlet-outlet boundary conditions would serve as a helpful junction to proceed in future.

Finally, the issue of incorporating boundary conditions and wall functions should also be addressed. This would allow for studying more complex flow fields and the effect of boundary layers which are essential when dealing with real-world problems. The work of Arno Mayrhofer 2014 on incorporating boundary conditions and wall functions for turbulence modelling would serve as a good starting point to proceed in future.

A Lagrangian LES Filtering of EDAC

EDAC Pressure evolution equation:

$$\frac{D P}{D t} = -c_s^2 \rho \nabla \cdot \mathbf{v} + \nu \nabla^2 P \quad (\text{A.1})$$

Lagrangian LES filter (Di Mascio et al. 2017):

$$\phi = \phi(\tilde{\mathbf{r}}_p(t) - \mathbf{y}, t - \tau) \quad (\text{A.2})$$

Substituting Eq. A.2 in Eq. A.1

$$\tilde{P}(\tilde{\mathbf{r}}_p, t) = \int_{\mathbb{R}^3} \int_{-\infty}^{\infty} \phi(\tilde{\mathbf{r}}_p(t) - \mathbf{y}, t - \tau) P(\mathbf{y}, \tau) d\tau dV_y \quad (\text{A.3})$$

Applying the Lagrangian derivative operator on both sides

$$\frac{D \tilde{P}(\tilde{\mathbf{r}}_p, t)}{D t} = \frac{D}{D t} \left(\int_{\mathbb{R}^3} \int_{-\infty}^{\infty} \phi(\tilde{\mathbf{r}}_p(t) - \mathbf{y}, t - \tau) P(\mathbf{y}, \tau) d\tau dV_y \right) \quad (\text{A.4})$$

Commuting the Lagrangian derivative operator and the integral operator

$$\frac{D \tilde{P}(\tilde{\mathbf{r}}_p, t)}{D t} = \int_{\mathbb{R}^3} \int_{-\infty}^{\infty} \frac{D \left(\phi(\tilde{\mathbf{r}}_p(t) - \mathbf{y}, t - \tau) P(\mathbf{y}, \tau) \right)}{D t} d\tau dV_y \quad (\text{A.5})$$

Applying chain rule and introducing $(\mathcal{I}_1, \mathcal{I}_2)$

$$\begin{aligned} \frac{D \tilde{P}(\tilde{\mathbf{r}}_p, t)}{D t} &= \int_{\mathbb{R}^3} \int_{-\infty}^{\infty} \left(\frac{\partial \phi(\tilde{\mathbf{r}}_p(t) - \mathbf{y}, t - \tau)}{\partial t} + \frac{D \tilde{\mathbf{r}}_p}{D t} \cdot \nabla \phi(\tilde{\mathbf{r}}_p(t) - \mathbf{y}, t - \tau) \right) P(\mathbf{y}, \tau) d\tau dV_y \\ &= \int_{\mathbb{R}^3} \int_{-\infty}^{\infty} \left(\underbrace{\frac{\partial \phi(\tilde{\mathbf{r}}_p(t) - \mathbf{y}, t - \tau)}{\partial t}}_{\mathcal{I}_1} + \underbrace{\tilde{\mathbf{v}}(\tilde{\mathbf{r}}_p, t) \cdot \nabla \phi(\tilde{\mathbf{r}}_p(t) - \mathbf{y}, t - \tau)}_{\mathcal{I}_2} \right) P(\mathbf{y}, \tau) d\tau dV_y \\ &= \int_{\mathbb{R}^3} \int_{-\infty}^{\infty} (\mathcal{I}_1 + \mathcal{I}_2) P(\mathbf{y}, \tau) d\tau dV_y \end{aligned} \quad (\text{A.6})$$

Rewriting (\mathcal{I}_1) as a function of $[\phi(\tilde{\mathbf{r}}_p(t) - \mathbf{y}, t - \tau)]$ using integration by parts

$$\int_{\mathbb{R}^3} \int_{-\infty}^{\infty} \mathcal{I}_1 P(\mathbf{y}, \tau) d\tau dV_y = \int_{\mathbb{R}^3} \int_{-\infty}^{\infty} \frac{\partial \phi(\tilde{\mathbf{r}}_p(t) - \mathbf{y}, t - \tau)}{\partial t} P(\mathbf{y}, \tau) d\tau dV_y = \\ \int_{\mathbb{R}^3} \int_{-\infty}^{\infty} \phi(\tilde{\mathbf{r}}_p(t) - \mathbf{y}, t - \tau) \frac{\partial P(\mathbf{y}, \tau)}{\partial \tau} d\tau dV_y \quad (\text{A.7})$$

Rewriting (\mathcal{I}_2) as a function of $[\phi(\tilde{\mathbf{r}}_p(t) - \mathbf{y}, t - \tau)]$ using integration by parts

$$\int_{\mathbb{R}^3} \int_{-\infty}^{\infty} \mathcal{I}_2 P(\mathbf{y}, \tau) d\tau dV_y = \int_{\mathbb{R}^3} \int_{-\infty}^{\infty} \left(\tilde{\mathbf{v}}(\tilde{\mathbf{r}}_p, t) \cdot \nabla \phi(\tilde{\mathbf{r}}_p(t) - \mathbf{y}, t - \tau) \right) P(\mathbf{y}, \tau) d\tau dV_y = \\ \int_{\mathbb{R}^3} \int_{-\infty}^{\infty} \phi(\tilde{\mathbf{r}}_p(t) - \mathbf{y}, t - \tau) \tilde{\mathbf{v}}(\tilde{\mathbf{r}}_p, t) \cdot \nabla_y P(\mathbf{y}, \tau) d\tau dV_y \quad (\text{A.8})$$

Substituting Eq. A.7 and Eq. A.8 in Eq. A.6 and introducing (\mathcal{I})

$$\frac{D \tilde{P}(\tilde{\mathbf{r}}_p, t)}{Dt} = \int_{\mathbb{R}^3} \int_{-\infty}^{\infty} \phi(\tilde{\mathbf{r}}_p(t) - \mathbf{y}, t - \tau) \underbrace{\left(\frac{\partial P(\mathbf{y}, \tau)}{\partial \tau} + \tilde{\mathbf{v}}(\tilde{\mathbf{r}}_p, t) \cdot \nabla_y P(\mathbf{y}, \tau) \right)}_{\mathcal{I}} d\tau dV_y \\ = \int_{\mathbb{R}^3} \int_{-\infty}^{\infty} \phi(\tilde{\mathbf{r}}_p(t) - \mathbf{y}, t - \tau) (\mathcal{I}) d\tau dV_y \quad (\text{A.9})$$

Rewriting (\mathcal{I}) by incorporating Eq. A.1

$$\frac{\partial P(\mathbf{y}, \tau)}{\partial \tau} + \tilde{\mathbf{v}}(\tilde{\mathbf{r}}_p, t) \cdot \nabla_y P(\mathbf{y}, \tau) = \frac{\partial P(\mathbf{y}, \tau)}{\partial \tau} + \left(\tilde{\mathbf{v}}(\tilde{\mathbf{r}}_p, t) - \mathbf{v}(\mathbf{y}, \tau) + \mathbf{v}(\mathbf{y}, \tau) \right) \cdot \nabla_y P(\mathbf{y}, \tau) \\ = \left(\frac{\partial P(\mathbf{y}, \tau)}{\partial \tau} + \mathbf{v}(\mathbf{y}, \tau) \cdot \nabla P(\mathbf{y}, \tau) \right) + \left(\tilde{\mathbf{v}}(\tilde{\mathbf{r}}_p, t) - \mathbf{v}(\mathbf{y}, \tau) \right) \cdot \nabla_y P(\mathbf{y}, \tau) \\ = \frac{D P(\mathbf{y}, \tau)}{D \tau} + \left(\tilde{\mathbf{v}}(\tilde{\mathbf{r}}_p, t) - \mathbf{v}(\mathbf{y}, \tau) \right) \cdot \nabla_y P(\mathbf{y}, \tau) \\ = \left(-c_s^2 \rho \nabla_y \mathbf{v}(\mathbf{y}, \tau) + \nu \nabla_y^2 P(\mathbf{y}, \tau) \right) + \left(\tilde{\mathbf{v}}(\tilde{\mathbf{r}}_p, t) - \mathbf{v}(\mathbf{y}, \tau) \right) \cdot \nabla_y P(\mathbf{y}, \tau) \quad (\text{A.10})$$

Substituting Eq. A.10 in Eq. A.9, and making use of the fact that the differential and spatial filtering operator commute far from the boundaries $[\nabla \tilde{a} = \widetilde{\nabla a}]$ (Di Mascio et al. 2017)

$$\frac{D \tilde{P}(\tilde{\mathbf{r}}_p, t)}{Dt} = \int_{\mathbb{R}^3} \int_{-\infty}^{\infty} \phi(\tilde{\mathbf{r}}_p(t) - \mathbf{y}, t - \tau) (\mathcal{I}) d\tau dV_y \\ = -c_s^2 \rho \widetilde{\nabla \cdot \mathbf{v}} + \nu \widetilde{\nabla^2 P} + \widetilde{\mathbf{v} \cdot \nabla \tilde{P}} - \widetilde{\mathbf{v} \cdot \nabla P} \quad (\text{A.11}) \\ = -c_s^2 \rho \nabla \cdot \widetilde{\mathbf{v}} + \nu \nabla^2 \widetilde{P} + \widetilde{\mathbf{v} \cdot \nabla \tilde{P}} - \widetilde{\mathbf{v} \cdot \nabla P}$$

$$\therefore \frac{D \tilde{P}}{Dt} = -c_s^2 \rho \nabla \cdot \widetilde{\mathbf{v}} + \nu \nabla^2 \widetilde{P} + \widetilde{\mathbf{v} \cdot \nabla \tilde{P}} - \widetilde{\mathbf{v} \cdot \nabla P} \quad (\text{A.12})$$

Bibliography

- Adami, S., X. Y. Hu, and N. A. Adams (2012). *Simulating three-dimensional turbulence with SPH*. Lehrstuhl für Aerodynamik.
- Antuono, M. et al. (2021). "Smoothed particle hydrodynamics method from a large eddy simulation perspective. Generalization to a quasi-Lagrangian model". In: *Physics of fluids* (Woodbury, N.Y.: 1994) 33.1, p. 015102. ISSN: 1070-6631. DOI: 10.1063/5.0034568. URL: <http://dx.doi.org/10.1063/5.0034568>.
- Bhosale, Aditya and Prabhu Ramachandran (2020). "Compyle: a Python package for parallel computing". In: *Proceedings of the 19th Python in Science Conference*. Ed. by Meghann Agarwal et al., pp. 32–39. DOI: 10.25080/Majora-342d178e-005.
- Bonet, Javier and T-SL Lok (1999). "Variational and momentum preservation aspects of smooth particle hydrodynamic formulations". In: *Computer Methods in applied mechanics and engineering* 180.1-2, pp. 97–115.
- Canelas, Ricardo B et al. (2016). "Hunting for Lagrangian Coherent Structures : SPH-LES turbulence simulations with Wall-adapting Local Eddy Viscosity (WALE) model". In: *11th SPHERIC* (March 2017). URL: https://www.researchgate.net/publication/315665064_Hunting_for_Lagrangian_Coherent_Structures_SPH-LES_turbulence_simulations_with_Wall-adapting_Local_Eddy_Viscosity_WALE_model.
- Chola, Kalale and Tsumoru Shintake (2021). "Generalized entropically damped artificial compressibility for weakly compressible SPH". In: *Computers and Fluids* 229.July, p. 105093. ISSN: 00457930. DOI: 10.1016/j.compfluid.2021.105093. URL: <https://doi.org/10.1016/j.compfluid.2021.105093>.
- Chorin, Alexandre Joel (1968). "Numerical solution of the Navier-Stokes equations". In: *Mathematics of computation* 22.104, pp. 745–762.
- Clausen, Jonathan R. (2013). "Entropically damped form of artificial compressibility for explicit simulation of incompressible flow". In: *Physical Review E - Statistical, Nonlinear, and Soft Matter Physics* 87.1, pp. 1–12. ISSN: 15393755. DOI: 10.1103/PhysRevE.87.013309.
- Cleary, Paul W and Joseph J Monaghan (1999). "Conduction modelling using smoothed particle hydrodynamics". In: *Journal of Computational Physics* 148.1, pp. 227–264.
- Cummins, Sharen J and Murray Rudman (1999). "An SPH projection method". In: *Journal of computational physics* 152.2, pp. 584–607.
- Dalrymple, R A and B D Rogers (2006). "Numerical modeling of water waves with the SPH method". In: 53. Favre-Averaging, Sub-Particle Scaling, Shepard Filtering, pp. 141–147. DOI: 10.1016/j.coastaleng.2005.10.004.
- Dauch, TF et al. (2018). "Highly efficient computation of Finite-Time Lyapunov Exponents (FTLE) on GPUs based on three-dimensional SPH datasets". In: *Computers & Fluids* 175, pp. 129–141.
- Di Mascio, A. et al. (2017). "Smoothed particle hydrodynamics method from a large eddy simulation perspective". In: *Physics of Fluids* 29.3. ISSN: 10897666. DOI: 10.1063/1.4978274.

- Drikakis, Dimitris and Piotr K Smolarkiewicz (2001). "On spurious vortical structures". In: *Journal of Computational physics* 172.1, pp. 309–325.
- Frigo, Matteo and Steven G Johnson (2005). "The design and implementation of FFTW3". In: *Proceedings of the IEEE* 93.2, pp. 216–231.
- Gossler, Albert A (2001). *Moving Least-Squares: a numerical differentiation method for irregularly spaced calculation points*. Tech. rep. Sandia National Lab.(SNL-NM), Albuquerque, NM (United States); Sandia ...
- Gotoh, Hitoshi, Songdong Shao, and Tetsu Memita (2004). "SPH-LES model for numerical investigation of wave interaction with partially immersed breakwater". In: *Coastal Engineering Journal* 46 (1), pp. 39–63. ISSN: 17936292. DOI: 10.1142/S0578563404000872.
- Haftu, Asmelash, Abhinav Muta, and Prabhu Ramachandran (2022). "Parallel adaptive weakly-compressible SPH for complex moving geometries". In: *Computer Physics Communications* 277, p. 108377. ISSN: 00104655. DOI: 10.1016/j.cpc.2022.108377. arXiv: 2201.00514. URL: <https://doi.org/10.1016/j.cpc.2022.108377>.
- Haller, George (2005). "An objective definition of a vortex". In: *Journal of fluid mechanics* 525, pp. 1–26.
- Hardy, Robert J (1982). "Formulas for determining local properties in molecular-dynamics simulations: Shock waves". In: *The Journal of Chemical Physics* 76.1, pp. 622–628.
- Harris, Charles R. et al. (Sept. 2020). "Array programming with NumPy". In: *Nature* 585.7825, pp. 357–362. DOI: 10.1038/s41586-020-2649-2. URL: <https://doi.org/10.1038/s41586-020-2649-2>.
- Holm, Darryl D, Jerrold E Marsden, and Tudor S Ratiu (1998). "Euler-Poincaré models of ideal fluids with nonlinear dispersion". In: *Physical Review Letters* 80.19, p. 4173.
- Hu, X. Y. and N. A. Adams (2015). "A SPH Model for Incompressible Turbulence". In: *Procedia IUTAM* 18, pp. 66–75. ISSN: 22109838. DOI: 10.1016/j.piutam.2015.11.007. arXiv: 1204.5097.
- Hu, Xiang Yu and Nikolaus A Adams (2006). "A multi-phase SPH method for macroscopic and mesoscopic flows". In: *Journal of Computational Physics* 213.2, pp. 844–861.
- Hu, XY and Nikolaus A Adams (2007). "An incompressible multi-phase SPH method". In: *Journal of computational physics* 227.1, pp. 264–278.
- Huang, C. et al. (2019). "A kernel gradient-free SPH method with iterative particle shifting technology for modeling low-Reynolds flows around airfoils". en. In: *Engineering analysis with boundary elements* 106, pp. 571–587. ISSN: 0955-7997. DOI: 10.1016/j.enganabound.2019.06.010. URL: <http://dx.doi.org/10.1016/j.enganabound.2019.06.010>.
- Khayyer, A, H Gotoh, and SD Shao (2008). "Corrected incompressible SPH method for accurate water-surface tracking in breaking waves". In: *Coastal Engineering* 55.3, pp. 236–250.
- Kubo, Hidehito and Tsuguo Sunamura (2001). "Large-scale turbulence to facilitate sediment motion under spilling breakers". In: *Coastal Dynamics' 01*, pp. 212–221.
- Lam, Siu Kwan, Antoine Pitrou, and Stanley Seibert (2015). "Numba: A LLVM-based Python JIT compiler". In: *Proceedings of the Second Workshop on the LLVM Compiler Infrastructure in HPC*. New York, NY, USA: ACM. ISBN: 9781450340052.
- Lancaster, Peter and Kes Salkauskas (1981). "Surfaces generated by moving least squares methods". In: *Mathematics of computation* 37.155, pp. 141–158.

- Li, Tingqiu, Peter Troch, and Julien De Rouck (2004). "Wave overtopping over a sea dike". In: *Journal of Computational Physics* 198.2, pp. 686–726.
- Li, Yi et al. (2008). "A public turbulence database cluster and applications to study Lagrangian evolution of velocity increments in turbulence". In: *Journal of Turbulence* 9, N31.
- Liu, M. B. and G. R. Liu (2006). "Restoring particle consistency in smoothed particle hydrodynamics". In: *Applied Numerical Mathematics* 56.1, pp. 19–36. ISSN: 01689274. DOI: 10.1016/j.apnum.2005.02.012.
- Liu, Sinuo et al. (Mar. 2019). "Viscosity-based Vorticity Correction for Turbulent SPH Fluids". In: IEEE, pp. 1048–1049. ISBN: 978-1-7281-1377-7. DOI: 10.1109/VR.2019.8798224. URL: <https://ieeexplore.ieee.org/document/8798224/>.
- Marsden, J. E. and S. Shkoller (2001). "Global well-posedness for the Lagrangian averaged Navier-Stokes (LANS- α) equations on bounded domains". In: *Philosophical Transactions of the Royal Society A: Mathematical, Physical and Engineering Sciences* 359.1784, pp. 1449–1468. ISSN: 1364503X. DOI: 10.1098/rsta.2001.0852.
- Mayrhofer, A et al. (2015). "DNS and LES of 3-D wall-bounded turbulence using smoothed particle hydrodynamics". In: *Computers & Fluids* 115, pp. 86–97.
- Mayrhofer, Arno (2014). "An investigation into wall boundary conditions and three-dimensional turbulent flows using smoothed particle hydrodynamics". The University of Manchester (United Kingdom), p. 181.
- Meurer, Aaron et al. (Jan. 2017). "SymPy: symbolic computing in Python". In: *PeerJ Computer Science* 3, e103. ISSN: 2376-5992. DOI: 10.7717/peerj-cs.103. URL: <https://doi.org/10.7717/peerj-cs.103>.
- Minion, Michael L and David L Brown (1997). "Performance of under-resolved two-dimensional incompressible flow simulations, II". In: *Journal of Computational Physics* 138.2, pp. 734–765.
- Mohseni, Kamran et al. (2003). "Numerical simulations of the Lagrangian averaged Navier-Stokes equations for homogeneous isotropic turbulence". In: *Physics of Fluids* 15.2, pp. 524–544. ISSN: 10706631. DOI: 10.1063/1.1533069.
- Monaghan, J. J. (Sept. 1992). "Smoothed particle hydrodynamics". In: *Annual Review of Astronomy and Astrophysics* 30.1, pp. 543–574. ISSN: 00664146. DOI: 10.1146/annurev.aa.30.090192.002551.
- (Apr. 2002). "SPH compressible turbulence". In: 852, pp. 843–852. DOI: 10.1046/j.1365-8711.2002.05678.x. URL: <http://arxiv.org/abs/astro-ph/0204118>.
20http://dx.doi.org/10.1046/j.1365-8711.2002.05678.x.
 - (2011). "A turbulence model for smoothed particle hydrodynamics". In: *European Journal of Mechanics, B/Fluids* 30 (4), pp. 360–370. ISSN: 09977546. DOI: 10.1016/j.euromechflu.2011.04.002. URL: <http://dx.doi.org/10.1016/j.euromechflu.2011.04.002>.
 - (2017). "SPH- ϵ simulation of 2D turbulence driven by a moving cylinder". In: *European Journal of Mechanics, B/Fluids* 65, pp. 486–493. ISSN: 09977546. DOI: 10.1016/j.euromechflu.2017.03.011. URL: <http://dx.doi.org/10.1016/j.euromechflu.2017.03.011>.
 - (1989). "On the problem of penetration in particle methods". In: *Journal of Computational physics* 82.1, pp. 1–15.
- Morris, Joseph P, Patrick J Fox, and Yi Zhu (1997). "Modeling low Reynolds number incompressible flows using SPH". In: *Journal of computational physics* 136.1, pp. 214–226.
- Muta, Abhinav and Prabhu Ramachandran (2022). *Efficient and accurate adaptive resolution for weakly-compressible SPH*. Vol. 395. Elsevier B.V., p. 115019. DOI: 10.1016/

- j . cma . 2022 . 115019. arXiv: 2107 . 01276. URL: <https://doi.org/10.1016/j.cma.2022.115019>.
- Negi, Pawan and Prabhu Ramachandran (2021). "How to train your solver: A method of manufactured solutions for weakly compressible smoothed particle hydrodynamics". In: *Physics of fluids* (Woodbury, N.Y.: 1994) 33.12, p. 127108. ISSN: 1070-6631. DOI: 10 . 1063 / 5 . 0072383. URL: <http://dx.doi.org/10.1063/5.0072383>.
- (2022). "Techniques for second-order convergent weakly compressible smoothed particle hydrodynamics schemes without boundaries". In: *Physics of Fluids* 34.8, p. 087125. ISSN: 1070-6631. DOI: 10 . 1063 / 5 . 0098352. arXiv: 2107 . 11859.
- Negi, Pawan, Prabhu Ramachandran, and Asmelash Haftu (2020). "An improved non-reflecting outlet boundary condition for weakly-compressible SPH". In: *Computer Methods in Applied Mechanics and Engineering* 367, p. 113119.
- Nicoud, Franck et al. (2011). "Using singular values to build a subgrid-scale model for large eddy simulations". In: *Physics of fluids* 23.8, p. 085106.
- Obeidat, Anas and Stéphane P.A. Bordas (2018). "Three-dimensional remeshed smoothed particle hydrodynamics for the simulation of isotropic turbulence". In: *International Journal for Numerical Methods in Fluids* 86 (1), pp. 1–19. ISSN: 10970363. DOI: 10 . 1002 / fld . 4405.
- Okrashevski, Max et al. (2022). "Smoothed Particle Hydrodynamics Physically Reconsidered – The Relation to Explicit Large Eddy Simulation and the Issue of Particle Duality". In: URL: <http://arxiv.org/abs/2206.10127>.
- Panizzo, Andrea (2004). "Physical and numerical modelling of subaerial landslide generated waves". PhD thesis. PhD Thesis, Universita Degli Studi di L'Aquila, Italy.
- Pereira, Filipe S et al. (2021). "Modeling and simulation of transitional Taylor-Green vortex flow with partially averaged Navier-Stokes equations". In: *Physical Review Fluids* 6.5, p. 054611.
- Pope, SB (1994). "Lagrangian PDF Methods For Turbulent Flows". In: *Annu. Rev. Fluid Mech* 23, p. 63.
- Pope, Stephen B and Stephen B Pope (2000). *Turbulent flows*. Cambridge university press.
- Ramachandran, P. (Sept. 2018). "automan: A Python-Based Automation Framework for Numerical Computing". In: *Computing in Science & Engineering* 20.05, pp. 81–97. ISSN: 1558-366X. DOI: 10 . 1109 / MCSE . 2018 . 05329818.
- Ramachandran, Prabhu, Aditya Bhosale, et al. (Dec. 2021). "PySPH: A Python-based Framework for Smoothed Particle Hydrodynamics". In: *ACM Transactions on Mathematical Software* 47.4, pp. 1–38. ISSN: 0098-3500, 1557-7295. DOI: 10 . 1145 / 3460773.
- Ramachandran, Prabhu and Kunal Puri (Dec. 2019). "Entropically damped artificial compressibility for SPH". In: *Computers and Fluids* 179, pp. 579–594. ISSN: 00457930. DOI: 10 . 1016 / j . compfluid . 2018 . 11 . 023. arXiv: 1612 . 05901. URL: <http://arxiv.org/abs/1612.05901%20http://dx.doi.org/10.1016/j.compfluid.2018.11.023>.
- Rennehan, Douglas (2021). "Mixing matters". In: *Monthly Notices of the Royal Astronomical Society* 506.2, pp. 2836–2852.
- Rogers, Benedict D. and Robert A. Dalrymple (Apr. 2005). "SPH Modeling Of Breaking Waves". In: *Coastal Engineering 2004*. World Scientific Publishing Company, pp. 415–427. ISBN: 978-981-256-298-2. DOI: 10 . 1142 / 9789812701916 _ 0032. URL: http://www.worldscientific.com/doi/abs/10.1142/9789812701916%7B%5C_7D0032.

- Sagaut, Pierre (2002). "Statistical and Spectral Analysis of Turbulence". In: *Large Eddy Simulation for Incompressible Flows*. Springer, pp. 379–390.
- Schmitt, Francois G (2017). "Turbulence from 1870 to 1920: The birth of a noun and of a concept". In: *Comptes Rendus Mécanique* 345.9, pp. 620–626.
- Shadden, Shawn C, Francois Lekien, and Jerrold E Marsden (2005). "Definition and properties of Lagrangian coherent structures from finite-time Lyapunov exponents in two-dimensional aperiodic flows". In: *Physica D: Nonlinear Phenomena* 212.3-4, pp. 271–304.
- Shao, Songdong (2006). "Incompressible SPH simulation of wave breaking and over-topping with turbulence modelling". In: (May 2005), pp. 597–621.
- Shao, Songdong and Hitoshi Gotoh (May 2005). "Turbulence particle models for tracking free surfaces". In: *Journal of Hydraulic Research* 43.3, pp. 276–289. ISSN: 0022-1686. DOI: 10.1080/00221680509500122. URL: <https://www.tandfonline.com/doi/full/10.1080/00221680509500122>.
- Shepard, Donald (1968). "A two-dimensional interpolation function for irregularly-spaced data". In: *Proceedings of the 1968 23rd ACM national conference*, pp. 517–524.
- Shi, Yilei et al. (2013). "Analysis of interpolation schemes for the accurate estimation of energy spectrum in Lagrangian methods". In: *Computers and Fluids* 82, pp. 122–131. ISSN: 00457930. DOI: 10.1016/j.compfluid.2013.05.003. URL: <http://dx.doi.org/10.1016/j.compfluid.2013.05.003>.
- Smagorinsky, Joseph (1963). "General circulation experiments with the primitive equations: I. The basic experiment". In: *Monthly weather review* 91.3, pp. 99–164.
- Sun, PN, A Colagrossi, et al. (2016). "Detection of Lagrangian coherent structures in the SPH framework". In: *Computer Methods in Applied Mechanics and Engineering* 305, pp. 849–868.
- Sun, PN, Andrea Colagrossi, et al. (2018). "Multi-resolution Delta-plus-SPH with tensile instability control: Towards high Reynolds number flows". In: *Computer Physics Communications* 224, pp. 63–80.
- Synolakis, Constantine Emmanuel (1986). "The runup of long waves". PhD thesis. California Institute of Technology.
- Taneda, Sadatoshi (1977). "Visual study of unsteady separated flows around bodies". In: *Progress in Aerospace Sciences* 17.4, pp. 287–348.
- Violeau, D., S. Piccon, and J.-P. Chabard (July 2002). "Two Attempts Of Turbulence Modelling In Smoothed Particle Hydrodynamics". In: vol. 1. WORLD SCIENTIFIC, pp. 339–346. ISBN: 978-981-02-4931-1. DOI: 10.1142/9789812777591_0041.
- Wang, Dong and Philip L.F. Liu (2020). "An ISPH with $k - \epsilon$ closure for simulating turbulence under solitary waves". In: *Coastal Engineering* 157 (July 2019), p. 103657. ISSN: 03783839. DOI: 10.1016/j.coastaleng.2020.103657. URL: <https://doi.org/10.1016/j.coastaleng.2020.103657>.
- Yoshizawa, Akira (1986). "Statistical theory for compressible turbulent shear flows, with the application to subgrid modeling". In: *The Physics of fluids* 29.7, pp. 2152–2164.